UNIVERSIDADE DE LISBOA
FACULDADE DE CIÊNCIAS
DEPARTAMENTO DE FÍSICA

Laser-Induced Crystallization of Amorphous Silicon for Poly-Si/SiO_x Passivating Contacts

João Pedro Jones Olho Azul

Mestrado em Engenharia Física

Dissertação orientada por:
Orientador: Prof. Doutor Killian Lobato
Co-orientador: Prof. Doutor Giso Hahn

2025

Acknowledgements

I would like to express my gratitude to Prof. Killian Lobato and Prof. Giso Hahn for their support throughout this journey and for providing me with this research opportunity in the Photovoltaics Division of the University of Konstanz. I am also grateful to Dr. Barbara Terheiden for welcoming me into the team, for the valuable insights during the weekly group meetings, and for the great discussions throughout the long writing process of this thesis.

A special thanks to Tobias Okker for always being there for me, for all the meetings and discussions on lab experiments and results, and especially for brainstorming during the tougher times when things did not go as expected. His support and guidance, from the very beginning to the end, have been truly great and I really appreciate it.

A very special thank you to my family – your help, support, encouragement and lots of patience have been essential during the very long challenging moments.

To all the friends I had before college, those I met along the way during these tough but incredible five years of my degree, and the friends from my amazing Erasmus in Konstanz – thank you for being part of my life. I am truly grateful to have met you all and for the time we have spent and shared together.

To my flatmates, thank you for making life at home more enjoyable and for all the small, almost daily hangouts. Those times were a much-needed escape from the everyday routine, and I really cherished those simple, good moments.

Resumo

O crescente consumo energético da população mundial e a necessidade de transição de combustíveis fósseis para energias renováveis impulsiona a necessidade de desenvolver células fotovoltaicas mais eficientes e economicamente mais viáveis. Entre as diversas estruturas inovadoras, destacam-se os contactos passivadores, que combinam a função de passivação, reduzindo a recombinação indesejada de pares eletrão-buraco, com a seletividade do transporte de cargas, os chamados contactos seletivos de eletrões ou buracos. Em particular, os contactos passivadores de poly-Si/SiO_x, que são a arquitetura aqui em estudo, combinam uma camada fina de silício policristalino (poly-Si) com uma camada ultra fina de óxido de silício (SiO_x). A camada de poly-Si pode ser depositada nesta fase cristalina ou pode ainda ser depositada como silício amorfo (a-Si), sendo posteriormente exposta a um tratamento térmico de modo a passar para silício no estado policristalino. Neste contexto, a cristalização induzida por laser (LIC) surge como um possível processo a ser incorporado no fabrico de contactos passivadores, sendo esta uma técnica de processamento rápida, com um controlo localizado na escala do micrómetro e de baixo custo.

Este trabalho investiga a transformação de camadas de silício amorfo altamente dopado com fósforo, (n) a-Si:P, para (n) poly-Si:P, através de um processo de cristalização induzida por laser. Foram analisados duas fontes de laser pulsado de estado sólido com comprimentos de onda de 355 nm e 532 nm, denominados como laser ultravioleta (UV) e verde, respetivamente. As amostras são compostas por um substrato com uma espessura de 155 μm de silício cristalino dopado com fósforo (c-Si:P) e, em ambos os lados do substrato, uma camada fina de 1.9 nm de SiO_x, juntamente com uma camada de (n) a-Si:P com 100 nm de espessura no topo.

A análise foca-se na relação entre os parâmetros do laser – potência P, desfocalização D ("defocus" é o desvio da posição do plano focal em relação à superfície da amostra) e espaçamento entre pulsos consecutivos L – com a cristalização induzida por laser, para efeitos de qualidade de passivação e características de microestrutura da camada, tal como a condutividade e o tamanho dos cristais de Si.

Foi realizado um estudo comparativo entre as fontes laser, que demonstrou a influência dos coeficientes de absorção do a-Si para comprimentos de onda distintos. Amostras processadas com o laser verde demonstraram consistentemente ablação da superfície. Para além disso, medições de espetrometria de emissão ótica por descarga luminescente (GDOES) indicaram a inexistência de óxido de túnel, evidenciada pela ausência de um pico de concentração no sinal de oxigénio. Foi possível deduzir que, devido ao menor coeficiente de absorção do a-Si para o comprimento de onda de emissão de 532 nm, a radiação laser atravessa a camada de a-Si e é maioritariamente absorvida pelo substrato de c-Si, que apresenta um coeficiente de absorção mais elevado para este comprimento de onda. Esse efeito resulta num aumento significativo da temperatura do c-Si, que danifica a camada fina de óxido. Já as amostras com o laser UV não apresentam marcas de ablação na superfície e as medições de GDOES encontravam-se de acordo com as medições de referência. Como o laser UV permite maior controlo e não apresenta sinais de dano evidentes nas camadas das amostras processadas, este foi escolhido como fonte laser para

o processamento das amostras.

O processamento a laser em bolachas com uma área de $156.5 \times 156.5\,\mathrm{mm}^2$ foi testado fazendo o varrimento de duas formas: (i) utilizando apenas o galvanómetro para o rastreamento completo da bolacha, ou (ii) movendo a bolacha com a mesa de varrimento XY para posicionar cada área de processamento no centro, deixando o galvanómetro varrer apenas essa região menor. No caso (i) observou-se um contraste visual dentro das áreas processadas e o microscópio permitiu observar variações significativas na morfologia. Enquanto algumas regiões exibiam marcas claras de pulsos, indicando ablação, outras, processadas com os mesmos parâmetros laser, permaneciam inalteradas, correspondendo ao resultado desejado, uma vez que evitar danos às camadas devido à energia excessiva é essencial. No caso (ii), bolachas processadas com os mesmos parâmetros apresentaram morfologias uniformes e a ausência de quaisquer evidências de ablação. Estes resultados sugerem que, dada a dimensão da bolacha, o rastreamento feito apenas com o galvanómetro pode levar a variações na incidência do feixe na superfície, possivelmente resultantes de ângulos acentuados introduzidos pela direção do feixe em relação à posição na bolacha. Assim, o método que combina a mesa de varrimento com o galvanómetro mostrou ser o mais eficaz para um processamento homogéneo.

Foram testados diversos conjuntos de parâmetros laser resultantes em valores de fluência entre 0 e $0.6\,\mathrm{J/cm}^2$. Os valores de tensão de circuito aberto implícita ($\mathrm{i}V_{\mathrm{oc}}$), obtidos por decaimento de fotocondutância (PCD), demonstram uma elevada dispersão de valores mesmo para fluências semelhantes. O facto da camada de a-Si apresentar um certo grau de não homogeneidade dificulta a análise destes resultados, uma vez que as variações observadas podem dever-se não só aos parâmetros testados, mas também à própria falta de homogeneidade da camada. Adicionalmente, foram testadas diferentes posições ou orientações dos tratamentos a laser para investigar possíveis padrões associados à falta de homogeneidade. Observou-se que, na zona esquerda (considerando como ponto de referência um número de identificação marcado na bolacha), as regiões central e inferior apresentavam, de forma consistente, a melhor qualidade de passivação. Os testes finais foram realizados em bolachas tratadas a laser com um único conjunto de parâmetros, com o objetivo de diminuir a influência da distribuição não homogénea da camada de a-Si numa amostra. Para avaliar o potencial de LIC após o processo de hidrogenação, nitrato de silício ($\mathrm{SiN_x}$:H) com 75 nm de espessura foi depositado por Deposição de Vapor Químico Enriquecida com Plasma (PECVD) no topo da amostra processada a laser. Foram testadas temperaturas de recozimento entre 700 °C a 900 °C. Observou-se que a qualidade da passivação diminuía com o aumento da temperatura, atingindo os piores resultados para a temperatura de 900 °C. Além disso, verificou-se que 750 °C seria a temperatura que proporcionava os melhores resultados, tendo sido esta adotada para a continuidade do projeto. Reunidas as condições do laser UV, o varrimento com a mesa de rastreamento XY em conjunto com o galvanómetro e hidrogenação com a temperatura de recozimento a 750 °C, foram realizados rastreamentos a laser em padrões de 3×3 em bolachas, utilizando os mesmos parâmetros de laser para a bolacha completa. A fluência aplicada variou entre 0 e aproximadamente $0.4\,\mathrm{J/cm}^2$. Os resultados indicaram que o processamento a laser resultou numa passivação semelhante à da bolacha de referência, ainda que ligeiramente inferior. A bolacha de referência foi submetida apenas ao processo de hidrogenação, sem tratamento a laser. Através de medições de PCD, obteve-se um valor médio de $\langle \mathrm{i}V_{\mathrm{oc}} \rangle = (0.677 \pm 0.015)\,\mathrm{V}$ para a amostra de referência, seguido de $\langle \mathrm{i}V_{\mathrm{oc}} \rangle = (0.672 \pm 0.012)\,\mathrm{V}$ para uma amostra preparada com $P = 1.5\,\mathrm{W}$, $D = 7.0\,\mathrm{mm}$ e $L = 35\,\mu\mathrm{m}$. No entanto, medições individuais, consistentemente localizadas na mesma região das bolachas, revelaram valores superiores de $\mathrm{i}V_{\mathrm{oc}}$ em relação ao valor médio, em diversas amostras, atingindo um máximo de 0.695 V observado para a amostra processada com $P = 1.0\,\mathrm{W}$, $D = 6.0\,\mathrm{mm}$ e $L = 35\,\mu\mathrm{m}$.

Relativamente à microestrutura, foram realizadas medições de Difração de Raios-X em amostras

tratadas a laser, mas sem qualquer processo de hidrogenação ou recozimento, significando que o único tratamento térmico foi o rastreamento a laser. Os resultados indicam que o grau de cristalinidade aumenta com a fluência aplicada, não sendo possível quantificar com precisão o grau. No entanto, neste caso, as amostras passaram também pelo processo de hidrogenação, que, em conjunto com o recozimento rápido, resultou numa melhoria mais significativa, comparativamente a apenas com o tratamento a laser. Observou-se também indícios de que a resistência de folha (R_{sh}) diminui com o aumento da fluência, apresentando todas as amostras analisadas consistentemente com um valor inferior ao da amostra de referência.

Em suma, esta investigação corrobora que LIC melhora a cristalinidade e a condutividade da camada processada de poly-Si em comparação com amostras não tratadas via laser, cuja camada de superfície se mantém tal como foi depositada (a-Si). A incorporação de um processo de hidrogenação – depositando uma camada rica em hidrogénio e realizando um passo de recozimento rápido, uma prática comum em células fotovoltaicas – pode melhorar ainda mais a condutividade e a cristalinidade. Além disso, LIC permite atingir valores de iV_{oc} comparáveis aos de bolachas de referência não tratadas a laser. Isto foi conseguido sem ablação da superfície, como observado com um microscópio ótico, e sem indícios de comprometer a estrutura da camada de poly-Si ou a interface de SiO_x, confirmada por medições de GDOES.

Palavras chave: Cristalização induzida por laser, silício amorfo, passivação, fluência, recozimento rápido.

Abstract

Laser-induced crystallization (LIC) was investigated to develop a suitable method to transform 100 nm-thick amorphous silicon (a-Si) into polycrystalline silicon (poly-Si) for poly-Si/SiO_x passivating contacts in silicon solar cells.

The project explores the influence of laser wavelength, scanning techniques and key laser parameters – such as power P, defocus D, and pulse spots distance L – on passivation quality, conductivity, and crystallinity. A comparison between 532 nm (green) and 355 nm (UV) nanosecond pulsed lasers highlights the impact of the absorption coefficients of a-Si for different wavelengths on crystallization, passivation quality and sample elemental composition due to the laser treatments. Results showed that the 355 nm source was more suited to the project as the 532 nm source treatments frequently resulted in layer ablation and a consequent absence of the oxide layer.

The investigation also assesses the role of hydrogenation by silicon nitride (SiN_x) deposition followed by a high-temperature, short-duration thermal step (fast firing), testing peak temperatures ranging from 700 to 900 °C. The results showed that firing temperature had a significant impact on passivation, identifying 750 °C as the optimal temperature.

Further samples were processed with the 355 nm laser source, followed by a hydrogenation process by firing at 750 °C. The highest achieved implied open-circuit voltage iV_{oc} results were: (0.677 ± 0.015) V, for a non-lasered sample, followed by (0.672 ± 0.012) V for a laser-treated wafer with $P = 1.5$ W, $D = 7.0$ mm and $L = 35\,\mu$m. However, individual measurements in several samples revealed higher iV_{oc} values, with a maximum of 0.695 V observed for $P = 1.0$ W, $D = 6.0$ mm, and $L = 35\,\mu$m. Additionally, crystallinity and conductivity of the a-Si layer improved due to laser treatments, in comparison to reference non-lasered wafers.

Keywords: Laser-induced crystallization, amorphous silicon, passivation quality, fluence, fast firing.

Contents

List of Figures

List of Tables

Acronyms

a-Si - Amorphous Silicon
Al-BSF - Aluminum Back Surface Field
APCVD - Atmospheric Pressure Chemical Vapor Deposition
ARC - Anti-reflective Coating
c-Si - Crystalline Silicon
poly-Si - Polycrystalline Silicon
CB - Conduction Band
Cz - Czochralski
EB-PVD - Electron-beam Physical Vapor Deposition
FPP - Four-Point-Probe
GDOES - Glow Discharge Optical Emission Spectroscopy
HF - Hydrofluoric
LIC - Laser-induced Crystallization
PCD - Photoconductance decay
PECVD - Plasma-enhanced Chemical Vapor Deposition
PERC - Passivated Emitter and Rear Cell
PL - Photoluminescence
PV - Photovoltaic
QSSPC - Quasi-steady-state Photoconductance
SRH - Shockley-Read-Hall
TOPCon - Tunnel Oxide Passivated Contact
UV - Ultraviolet
VB - Valence Band
XRD - X-ray Diffraction

List of Symbols

γ - Photon
ε_S - Permittivity of the material
θ - Angular position
θ_B - Bragg angle
λ - Wavelength
μ_n - Electron mobility
μ_p - Hole mobility
ρ - Resistivity
σ - Conductivity
τ_{eff} - Effective lifetime
ω - Beam radius
ω_0 - Focal beam radius
f - Frequency
iV_{oc} - Implied open-circuit voltage
$\langle \text{i}V_{\text{oc}} \rangle$ - Average implied open-circuit voltage
n - Concentration of electrons
p - Concentration of holes
q - Elemental charge
t - time
z_{R} - Rayleigh length
A - Area
C - Capacitance
D - Defocus
E_{c} - Conduction band energy
E_{F} - Fermi level
E_{g} - Bandgap energy
E_{v} - Valence band energy
I_{sc} - Short-circuit current
F - Fluence
G - Generation rate
L - Distance between laser pulses
P - Laser power
R - Recombination rate
R_{sh} - Sheet resistance
T - Temperature
T_{peak} - Firing peak temperature
V_{oc} - Open-circuit voltage
W - Layer thickness
Nd:YVO_4 - Neodymium-doped yttrium orthovanadate
SiN_x - Silicon nitride
SiO_x - Silicon oxide
Al_2O_3 - Aluminium oxide

Chapter 1

Introduction

The ongoing energy transition from a fossil fuel-based society to the implementation of diverse renewable energy sources is essential not only for environmental purposes but also from an economic sustainability perspective. A significant amount of CO_2 emissions needs to be reduced in all sectors. The climate change topic has received a lot of attention in recent years due to the worldwide commitment to the 2016 Paris Agreement. Since then, nations have been taking steps to align with the commitments declared regarding global warming.

Photovoltaics (PV) stands out as a key player in this transition among renewable energy sources, with general costs falling by 90 % in the last decade [1]. This cost reduction is related to several factors, including improvements in supply chain logistics, more effective manufacturing processes, lower material consumption during production and improved cell efficiencies, which allow greater energy generation per unit of installed area. The amount of solar energy installed in the EU increased by more than 40 % annually in both 2021 and 2022, and by more than 50 % in 2023. In 2024, a record 65.5 GW of solar capacity was installed, but compared with the previous year, the growth was only 4 %. To meet the 2030 climate targets, the EU must sustain an installation rate of at least 70.0 GW per year [2].

To address these challenges, improving solar cell designs is key to making them more efficient and cost-effective. One of these improvements is the use of passivating contacts, a technology that helps reduce energy losses by improving carrier selectivity and surface passivation. In October 2022, the PV module manufacturer JinkoSolar registered a new record for the maximum conversion efficiency of 26.1 % for a monocrystalline silicon TOPCon solar cell, surpassing their previous record of 25.7 % set in April [3]. This TOPCon architecture (Tunnel Oxide Passivated contact) is a well-defined implementation of poly-Si/SiO_x passivating contacts.

Looking at the market share of different solar cell technologies is important for understanding the industry. In 2021, the Passivated Emitter and Rear Cell (PERC) architecture dominated the industry, accounting for 75 % of the market, while other technologies, such as heterojunction solar cells, carry a smaller share of around 2.5 % [4]. In 2022, passivating contacts using tunnel oxide passivation at the rear side reached a 10 % share of the PV market [5].

Additionally, alternative fabrication approaches, such as laser-induced crystallization, present opportunities to enhance the performance and viability of these contacts. By improving these technologies, the PV industry can keep achieving efficiency gains while reducing production costs, helping drive the transition to a renewable energy-based economy and society.

Chapter 2

Theory

In this chapter, the fundamental principles of solar cells are presented, with an overview of semiconductor physics, in Section 2.1. Then, a focus on silicon-based solar cells will be presented in Section 2.2, specifically highlighting the amorphous form of silicon and the fundamental operations of solar cells. Next, the underlying theory on passivation is discussed in detail in Section 2.3, exploring recombination mechanisms and strategies to mitigate them. Finally, an introduction to passivating contacts and the ideal architecture of this concept to enhance efficiency will be done.

2.1 Semiconductor Physics

The key to understanding semiconductor behavior is the concept of the bandgap, which represents the minimum energy necessary to excite an electron stuck in its bound state into a free state, where it can participate in conduction. The lower energy level of a semiconductor corresponds to the valence band (VB), with energy E_{v}, and the energy level at which an electron can be considered free is called conduction band (CB), with E_{c}. The bandgap energy E_{g} is defined as the energy difference between E_{c} and E_{v}.

If an incident photon with an energy equal to or greater than the bandgap energy ($E_{\gamma} \geq E_{\mathrm{g}}$) is absorbed, an electron is excited from the VB to the CB, this is the case of a direct bandgap semiconductor - shown in Figure 2.1a. Once excited to the CB, the electron becomes a free electron able to move within the semiconductor and contribute to the conduction process. At the same time, the absence of an electron in the VB results in a hole there, leading to the generation of an electron-hole pair. If the photon energy is greater than the bandgap, the electron will transition to the CB with excess energy, which is then dissipated through thermalization.

In the case of a semiconductor with an indirect bandgap, like silicon, the excitation of an electron from the VB to the CB requires a multiple-particle interaction. Unlike in direct bandgap materials, where photon absorption alone is sufficient, here the CB and VB are not directly aligned – the lowest energy level of the CB is not vertically aligned with the highest energy level of the VB in momentum space – as shown in Figure 2.1b. Instead, for an electron to transition to the CB, it requires additional momentum, which is provided by phonons – vibrations of the crystal lattice. If the momentum provided by the phonons is high enough, along with the photon absorption, it successfully transits the electron to the CB.

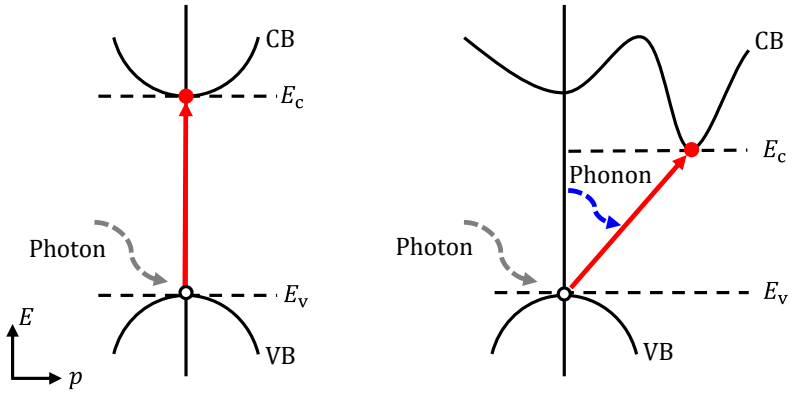

Figure 2.1: Photon absorption in a direct (a) and indirect (b) bandgap semiconductor. In both cases, $E_\gamma = E_g$. The X-axis is described as particle momentum p and the Y-axis is the energy level E.

At absolute zero (0 K), the thermal energy of the system is zero, and electrons cannot gain sufficient energy to transition from the VB to the CB. In this situation, all the energy levels below a specific energy are completely filled, while all levels above it remain empty. This energy is referred to as the Fermi energy, which is defined at absolute zero. At higher temperatures, electrons gain thermal energy, enabling some to occupy states with energies above the Fermi level.

For intrinsic semiconductors, the Fermi level is located in the middle of the bandgap. In other words, it corresponds to the energy where the probability of an electron occupying a state is 50 %, as described by the Fermi-Dirac distribution [6]. In doped semiconductors, the Fermi level shifts closer to the CB in n-type doping or closer to the VB in p-type doping. The Fermi level for n-type and p-type semiconductors is given by:

$$E_{F,n} = E_c - k_B T \ln\left(\frac{N_c}{n}\right), \tag{2.1}$$

$$E_{F,p} = E_v + k_B T \ln\left(\frac{N_v}{p}\right), \tag{2.2}$$

in which N_c and N_v are the effective density of states the CB and VB, respectively [6].

When two materials with distinct doping levels are joined, as their Fermi levels differ, they must reach equilibrium. This equilibrium results in a phenomenon known as band bending, where the conduction and valence bands bend continuously at the interface between the two differently doped regions to align their energy levels.

The energy necessary to remove an electron from the surface of a material into free space is called the work function. It is the energy difference between the vacuum level (0 eV, reference energy level) and the Fermi level. It ensures that the energy levels align properly in the material interfaces, allowing efficient carrier movement. This property also plays a role in the band bending process.

For temperatures above absolute zero, there are free charge carriers as there is thermal energy. Thermal energy is manifested in the form of phonons that interact with electrons in the VB and can cause the transition of electrons to the CB, generating electron-hole pairs. The formula that describes the probability that a certain energy state is occupied is called the Fermi-Dirac distribution. The intrinsic carrier concentration n_i is usually not enough for PV technologies to achieve the desired electrical goals. This concentration is given by:

$$n_i = \sqrt{n\,p}, \tag{2.3}$$

in which n and p are the equilibrium free electron and hole concentrations, respectively [6]. At equilibrium, the generation rate G of electron-hole pairs equals the recombination rate R, $G = R$, resulting in constant charge carrier concentrations.

For PV purposes, a doping process is performed on the semiconductor to increase the concentration of charge carriers. Impurities are purposely introduced to the semiconductor and the material becomes either: n-doped, if the dopant atoms have an extra electron compared to the material atoms and this extra electron becomes a free electron in the CB (donor atom); or p-doped, if the dopant atoms have one electron less, leaving an incomplete VB and creating an additional hole in the VB (acceptor atom). Doping will increase the concentration of one of the charge carriers, which will have the name of the majority carriers. As the law in the Equation (2.3) still applies, the concentration of the other carrier decreases, making it the minority carrier.

When an insulator is placed between two semiconductors with equal or similar bandgap, it creates a potential barrier due to the high bandgap of the insulating layer. When the insulator is thin enough, a quantum mechanical phenomenon known as tunneling can occur. Quantum tunneling happens when a charge carrier crosses a potential barrier without needing the classical energy to overcome it. The thinner the insulating layer, the higher the probability of tunneling [7].

2.2 Solar Cells

This section provides an overview of the main concepts of solar cells. Section 2.2.1 displays the key properties of silicon, followed by a focus on the amorphous form of silicon in Section 2.2.2, which plays a central role in this work. Further information on the essential mechanisms underlying cell operation is seen in Section 2.2.3.

2.2.1 Properties of Silicon

Silicon is the most common used material in solar cells. It is an indirect semiconductor material that belongs to the Group 14 of the Periodic Table. This element is among the most abundant on the crust of the Earth, although it never appears in its pure form in nature. Silicon has bandgap energy of 1.12 eV at 25 °C, a melting point 1414 °C and, at atmospheric pressure, it cristallizes in a diamond cubic structure [8]. Figure 2.2 shows the reference AM1.5G solar spectrum (with a standard irradiance of 1000 W/m^2) and marks the wavelength corresponding to the bandgap energy of silicon. This highlights the portion of the spectrum silicon solar cells can absorb, primarily the visible spectrum and near-infrared radiation. Silicon intrinsic carrier concentration is approximately $10^{10}\,cm^{-3}$ at 25 °C [9].

This material can exist in many forms, including amorphous silicon (a-Si), polycrystalline silicon (poly-Si), and crystalline silicon (c-Si). For many applications in PV technology, c-Si is commonly chosen as the bulk material, just like it was selected for this project. Over the years, various crystal growth techniques have been developed, such as the Float-Zone and Czochralski (Cz) methods. The latter is widely used for commercial and industrial fabrication, and it was the method employed to grow the c-Si bulk layer in this work. The process starts with inserting a small seed crystal, with a defined lattice orientation, into a silicon melt contained in a crucible. Then, the seed is pulled upwards and rotated at a controlled rate, obtaining a single crystal ingot in the end [8].

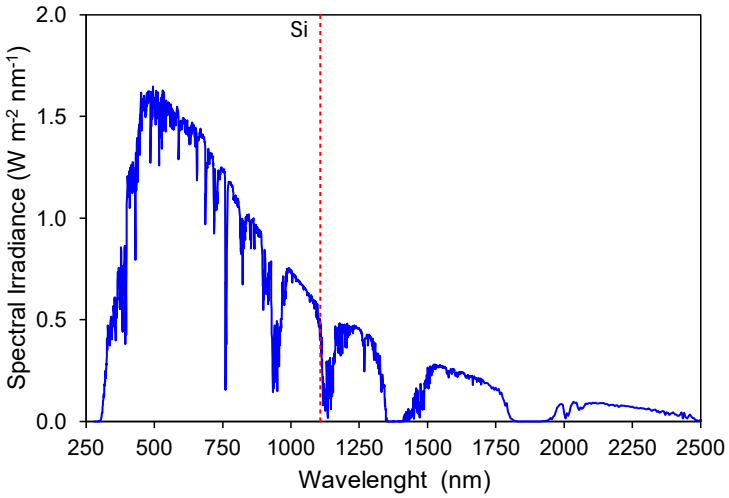

Figure 2.2: Reference AM1.5G solar spectrum displayed as spectral irradiance as a function of photon wavelength. The red dashed line marks the wavelength of 1107 nm, corresponding to photons with energy equal to or greater than the silicon bandgap energy (1.12 eV). Data sourced from the National Renewable Energy Laboratory [10].

Silicon has four valence electrons. Doping is typically performed with elements from Group 15, like phosphorus (P), for n-type doping, where the dopant adds a valence electron, contributing a free electron to the CB; Group 13, like boron (B) for p-type doping, where the dopant has one valence electron less than silicon, resulting in a hole in the VB. Recently, gallium doping, also from Group 13, is becoming more mainstream for commercial solar cells.

2.2.2 Amorphous Silicon

Poly-Si can be deposited directly, or it can deposited as a-Si layer and further crystallized into a polycrystalline state. Amorphous silicon has been used for decades, for instance, in the pioneering work of Si heterojunction formed between doped a-Si and c-Si back in 1974 by Fuhs *et al.* [11]. Opposite to c-Si, a-Si does not have a well-ordered crystal lattice, and only a short-range order is present in a-Si. Just like the name suggests, the atoms form bonds in a disordered structure, which results in a high density of dangling bonds. These defects impede the transport of carriers through the lattice, resulting in poor conductivity and high resistivity.

Non-hydrogenated a-Si has a high concentration of dangling bonds, leading to undesirable semiconductor properties. Passivating a-Si with hydrogen is a standard and well-studied procedure to reduce the density of defects by saturating them, while maintaining the material in the amorphous state [12]. Depending on the deposition method, hydrogenation can be incorporated into the deposition process directly, using specific precursor gases, or it can be done by depositing a hydrogen-rich layer, followed by a fast firing step that will allow the diffusion of the hydrogen content into the a-Si, making it a-Si:H. This fast firing step is a high temperature annealing process of short duration, typically lasting only a few seconds.

Due to the highly disordered nature of the a-Si lattice structure, the impurities introduced during the a-Si doping process often do not incorporate the crystalline structure, remaining interstitial impurities. If the layer undergoes an annealing step, the melting and re-crystallizing of the structure facilitate the incorporation of the impurity into the lattice, becoming a substitutional impurity [13]. This process, known as dopant activation, enhances the active dopant concentration of a layer.

Silicon exhibits a distinct absorption coefficient for each wavelength, depending on the photon energy

interacting with the material. In addition, c-Si and a-Si have a different absorption spectrum, as shown in Figure 2.3. This means that light of distinct wavelengths is absorbed differently, influencing the transmission and absorption rate. The wavelengths of 355 nm and 532 nm are highlighted in the plot as they correspond to the wavelength of the project's laser sources. It is clear that 355 nm has a higher absorption coefficient than 532 nm, meaning it is absorbed more strongly near the surface. In contrast, 532 nm, with its lower absorption coefficient, penetrates deeper into the a-Si layer.

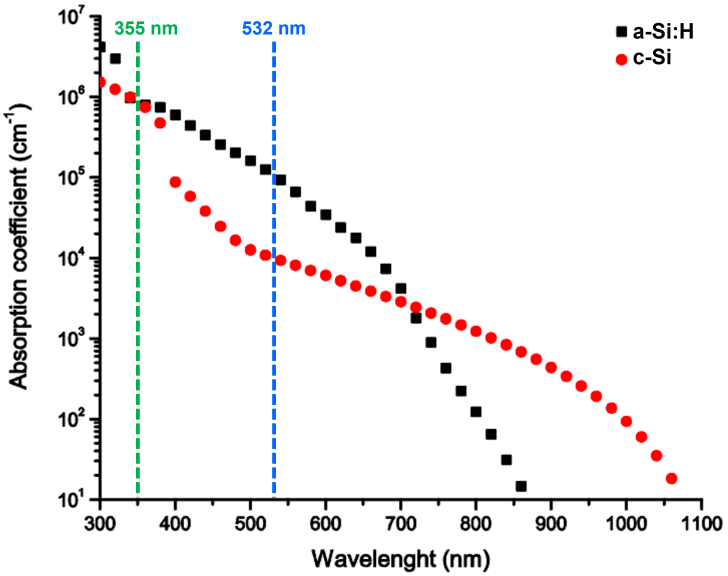

Figure 2.3: Absorption coefficients for a-Si:H and c-Si as a function of wavelength, highlighting 355 nm and 532 nm, which correspond to the laser source wavelengths used in this project. Adapted from Hernandez-Como *et al.* [14].

Besides photon absorption in the material, free carrier absorption also occurs in parallel. This process involves the absorption of photons by free electrons or holes, leading to energy transitions within the same or different bands, and not contributing for the generation of electron-hole pairs. However, for silicon, the free carrier absorption is generally negligible for wavelengths below 1000 nm and becomes more significant only at longer wavelengths, where free carrier effects are more pronounced [15].

2.2.3 Basic Solar Cell Operations

The working principle of solar cells relies on the conversion of photons to electricity. The physical phenomenon behind it is the photovoltaic effect, a process that generates voltage or electric current when it is exposed to light. When the material absorbs a photon with energy equal to or greater than the semiconductor bandgap, it excites an electron to the CB, creating an electron-hole pair, as previously shown in Figure 2.1. In the depletion region of a pn junction, the electric field separates the electron and hole, driving them in opposite directions, which generates a photogenerated current. Once the carriers are separated, they can be collected by a circuit connected to the cell through metallic contacts at the top and bottom of the cell.

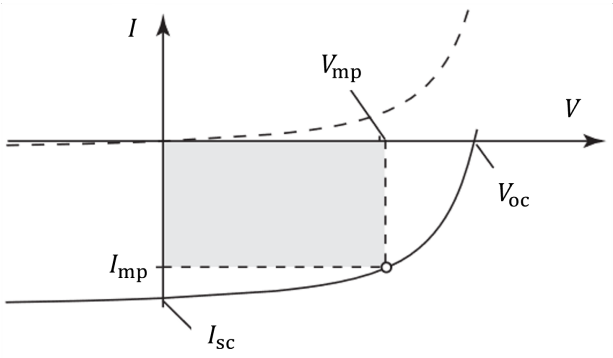

Figure 2.4: IV curve presented as the current of a pn junction in the dark, described by the dashed line, and under illumination, in the solid line, as a function of voltage. V_{mp} and I_{mp} are the voltage and current combination corresponding to the maximum power that the cell achieves.

An illustration of the IV curve, which represents the current and voltage characteristics of a solar cell, is displayed in Figure 2.4. This curve can be described by the diode model formula in Equation (2.4) [6]

$$I_L = I_{dark}\left[\exp\left(\frac{qV}{k_BT}\right) - 1\right] + I_{sc}, \tag{2.4}$$

where I_L is the light-generated current, I_{dark} is the dark saturation current of the diode, which, in this context, combines the carrier recombination mechanisms in the absence of light into one parameter. In addition, the open-circuit voltage ($I = 0$ A), can written by Equation (2.5)

$$V_{oc} = \frac{k_BT}{q}\ln\left(1 - \frac{I_{sc}}{I_{dark}}\right). \tag{2.5}$$

Another commonly investigated parameter is the implied open-circuit voltage (iV_{oc}). While V_{oc} represents the maximum voltage of a solar cell when no current flows, iV_{oc} corresponds to the potential in the absence of significant series resistance or contact losses. It is usually measured by photoconductance decay (PCD) or quasi-steady-state photoconductance (QSSPC) techniques and it gives insight into the passivation quality of the material before metallization in solar cell fabrication.

2.3 Passivation

This sector covers the topic of passivation. Section 2.3.1 begins by discussing the general recombination mechanisms in solar cells. Next, Section 2.3.2 focuses on surface passivation, describing both field-effect passivation and chemical passivation. Finally, an overview of the ideal behavior of a passivating contact is provided in Section 2.3.3.

2.3.1 Recombination Mechanisms

Radiative Recombination

Radiative recombination is the inverse process of generation of an electron-hole pair under illumination. When an electron in the CB recombines with a hole in the VB, it can emit a photon as it transitions to the VB. In indirect semiconductors, due to the offset in momentum, the recombination process also includes the emission, or absorption, of a phonon to conserve momentum from one band to the other, making this process less likely in materials like silicon. The recombination rate due to radiative processes

with a unit of volume per second is given by

$$R_{\text{rad}} = B_{\text{rad}} np, \tag{2.6}$$

in which B_{rad} is the coefficient for radiative recombination that remains to be determined [6].

There are mechanisms of recombination with no emission of photons, which are called non-radiative recombination. These are Auger recombination, recombination through defects, and surface recombination. Figure 2.5 shows an illustrative scheme of these mechanisms.

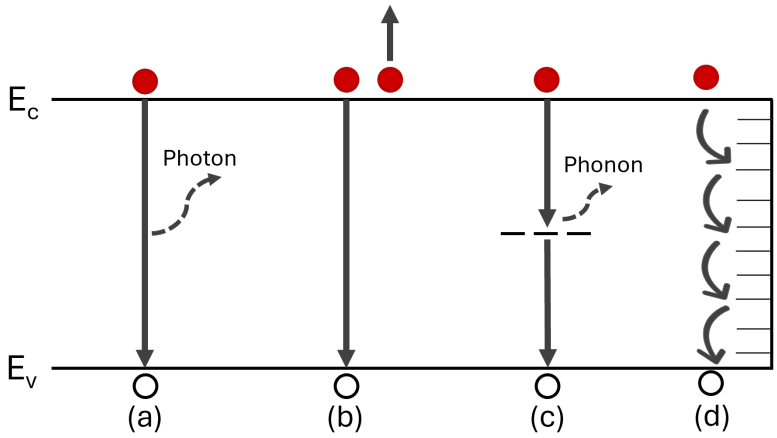

Figure 2.5: Schematic representation of recombination processes in a band diagram of a semiconductor. (a) Radiative recombination with an emission of a photon; (b) Auger recombination as a three-carrier phenomenon; (c) Shockley-Read-Hall recombination (recombination through defects); (d) Surface recombination.

Auger Recombination

Auger recombination is a three-carrier phenomenon. The energy released in the recombination of the electron-hole pair, instead of being emitted as a photon, is transferred to another electron from the CB, or hole from the valence band, exciting it to a higher energy level. The excited charge carrier eventually reaches equilibrium and dissipates the excess energy and momentum in the form of phonons. This type of recombination is more significant in materials with high carrier densities, such as heavily doped regions or under intense illumination and its rate also increases with temperature as higher thermal energy enhances carrier excitation. Auger recombination rate can be expressed by equation 2.7 [6]:

$$R_{\text{Auger}} = np\left(C_{\text{e}} n + C_{\text{h}} p\right). \tag{2.7}$$

Shockley-Read-Hall Recombination

Impurity defects introduce trap states within the bandgap, acting as recombination centers. In this process, a charge carrier first becomes trapped in a defect state within the forbidden region of the bandgap. If an opposite charge carrier transitions to the same defect energy state before the trapped carrier is re-emitted thermally, they will interact and recombine. In solar cells, this type of recombination is the most predominant, with impurities with energy levels near the middle of the bandgap being particularly important [6]. These impurities can trap both electrons and holes step by step, releasing small amounts of energy as heat during the process. Because the energy is released in small steps through vibrations in the crystal lattice – phonons – the transition of an electron from the CB to the VB happens more easily without emitting light with this mechanism. For this reason, radiative recombination

is less significant. This process is also known as Shockley-Read-Hall (SRH) recombination due to the investigation conducted by Shockley and Read [16], which was also studied and discussed by Hall [17].

Surface Recombination

Interfaces between two different material layers have a high concentration of defects due to the abrupt termination of the crystal lattice [8]. These interfaces are associated with a series of trap states in the forbidden region of the bandgap. The difference between surface recombination and SRH recombination is that, in surface recombination, there is a continuous distribution of trap states at the surface due to the high concentration of dangling bonds in interface regions. Electrons and holes can recombine through them, just like in the SRH recombination on the bulk.

2.3.2 Surface Passivation

Passivation is essential to improve cell efficiency, as recombination processes are always present in PV devices. This section will focus on the category of surface passivation as surface recombination is one of the recombination processes with more impact and more limiting in the technology of solar cells [18]. The main mechanisms are chemical passivation and field-effect passivation.

Field-effect Passivation

Field-effect passivation occurs when a dielectric layer or a highly doped layer generates an electric field at the interface with a semiconductor layer, producing a high-low junction. This electric field arises from the fixed charges in the dielectric layer or doping gradient. The presence of these layers causes band bending near the surface, i.e., the energy bands bend upward or downward, depending on the polarity of the field. This creates a region that favors the transport and free movement of majority carriers while repelling the minority carriers, keeping them away from the surface, reducing the recombination rate. This process is also used to form selective carrier contacts [18].

Chemical Passivation

Chemical passivation aims to reduce the density of surface states caused by dangling bonds as much as possible. This can be achieved by depositing a layer on the surface that forms stable chemical bonds with the surface atoms. For example, a hydrogenation process consists of the deposition of a hydrogen-rich layer that will diffuse onto the surface of the cell due to a firing step and will saturate those dangling bonds, neutralizing them and improving surface passivation (Section 4.2.3). This mechanism was applied through the deposition of silicon nitride (SiN_x) layer, which is rich in hydrogen content [19]. A post-deposition annealing step results in the saturation of dangling bonds and the diffusion of hydrogen into the wafer.

2.3.3 Ideal Passivating Contact

A standard solar cell structure is displayed in Figure 2.6. The central layer, known as the absorber, corresponds to the bulk layer, where the incident light is absorbed and the electron-hole pairs are generated. Since recombination of charge carriers is inevitable, a passivation layer is necessary on both sides of the cell. Ideally, these layers would be able to passivate all sources of recombination, which would significantly enhance the efficiency.

Selective contacts are necessary to separate the electron-hole pairs, allowing them to contribute to the photo-generated current. Figure 2.6 displays a hole-selective contact on the front of the cell, and an electron-selective contact on the back. In addition, the front side includes an anti-reflective coating (ARC), which reduces reflection losses and increases light absorption. Besides that, metallic contacts are required on both the front and back to connect the cell to an external electrical circuit. Note that, as the ARC is a dielectric layer, the metal contacts have to penetrate through this layer in order to contact with the selective contact.

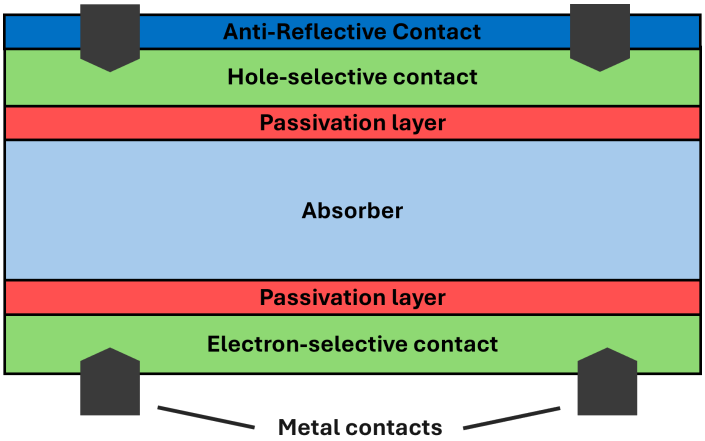

Figure 2.6: Schematic illustration of the essential layers of a generic solar cell.

The goal of a passivating contact is to combine a thin passivating layer with a charge-selective contact layer. It minimizes recombination losses by preventing direct contact between the metal contact and the absorber while allowing the majority carriers to move through freely, permitting efficient extraction of the charge carriers by an external circuit [20]. Typically, passivating contacts combine chemical passivation, which reduces surface defects, with field-effect passivation, by creating an electric field to repel minority carriers of the respective selective contact from the surface.

Chapter 3

State of the Art

The chapter begins with a discussion of PV technologies and the progression of efficiency in different designs. Next, a review of passivating contact technologies is done, leading on to poly-Si/SiO_x passivating contacts, in Section 3.1. Additionally, Section 3.2 explores the potential of laser-induced crystallization (LIC) as a possible cost-effective processing method for passivating contacts.

PV technology had a notable evolution over the years, spreading into various approaches that have a common goal - to increase the conversion efficiency of the solar cell and to reduce the fabrication costs. New architectures can provide a significant increase, but today most of the approaches need additional processing steps. In this context, laser processing offers an alternative way to process wafers that might be more cost-efficient and compatible with the PV industry. Figure 3.1 presents a plot incorporating the achieved efficiencies of solar cells over the years, starting in 1976 until the present. Here, the progress and the diversity of technologies are visible.

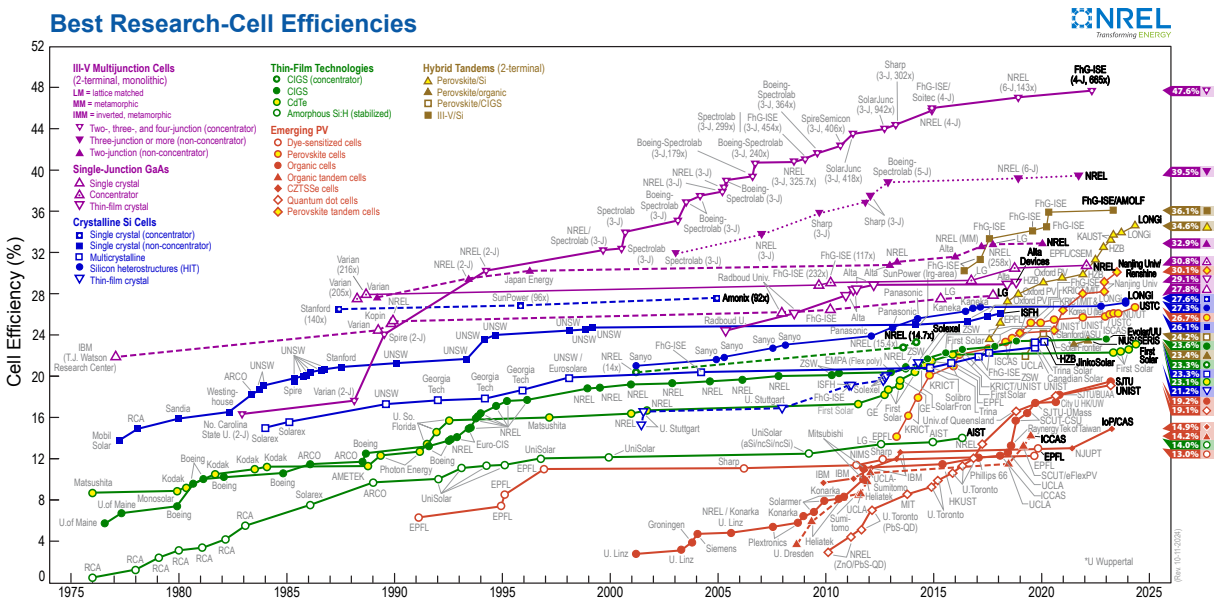

Figure 3.1: Profile of the highest confirmed conversion efficiencies for research cells for a range of photovoltaic technologies over the years, from 1976 to the present. Plot sourced from the *National Renewable Energy Laboratory* [21].

Figure 3.1 shows that higher conversion efficiencies are achieved with III-V multijunction cells, hybrid tandem structures, and emerging PV technologies, such as perovskites, compared to c-Si cells. The highest confirmed conversion efficiency is 47.6 % for a III-V multijunction cell featuring light concentration. In comparison, recent c-Si solar cells achieved efficiencies ranging from 21.2 % to 27.6 %. Despite

that, silicon remains one of the best choices for large-scale commercial PV applications, mainly due to its abundance and versatility, along with its proven stability and cost-effectiveness. Additionally, the material can be used in various applications, from thin films to Si substrates, passivating layers and selective contacts, depending on the crystallinity, layer thickness, dopant concentration and annealing methods.

It is important to note that there is a maximum theoretical limit to the energy conversion efficiency of a single pn junction solar cell. This limitation is called the Shockley–Queisser limit, in honor of William Shockley and Hans J. Queisser, who established it in 1961 [22]. The maximum efficiency was estimated to reach 30 % at a bandgap of 1.1 eV under standard conditions when radiative recombination is the only loss mechanism considered. In addition, the determined optimal bandgap aligns with the bandgap energy of silicon, which is one of the reasons why silicon is widely implemented in PV applications. More recently, researchers determined that, considering AM 1.5G solar spectrum, the maximum power conversion for a single junction cell is 33.16 % for a semiconductor bandgap energy of 1.34 eV [23].

The Aluminum Back Surface Field (Al-BSF) cell was once a widely adopted design, characterized by an aluminum alloy on the back surface. An aluminum layer is screen printed on the rear side and, through a firing step (typically between 750 °C to 900 °C), the aluminum melts and alloys with silicon, forming a highly doped p^+ region on the back side, named back surface field. A schematic of an Al-BSF cell for p-type Si is presented in Figure 3.2a. Traditional Al-BSF cells are designed for p-doped Si substrates, which are not so common for n-doped Si, whereas other rear-passivated designs exist that perform better with n-doped Si. For p-type Si solar cells, this structure was able to reach a power conversion efficiency near to 20 % [24].

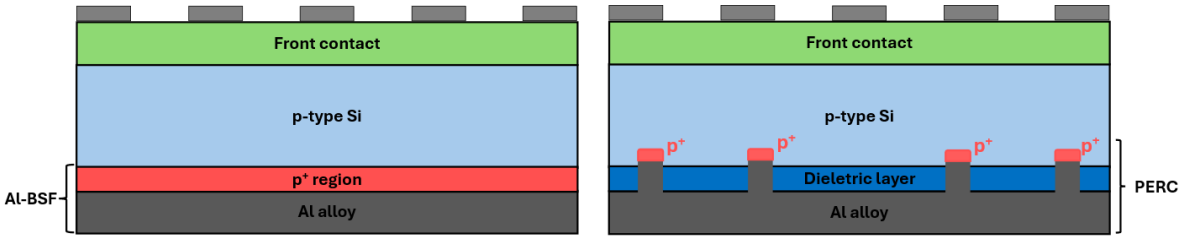

(a) Aluminum Back Surface Field (b) Passivated Emitter and Rear Cell

Figure 3.2: Schematic illustration of p-type silicon solar cell with (a) an Al-BSF design and (b) a PERC architecture (not to scale). The focus is on the rear side, where the key differences between the two designs are implemented. The front side is represented generically, with metal contacts on top.

Later on, another well-investigated design became popular, the Passivated Emitter and Rear Cell (PERC), achieving higher efficiencies in the range of 23-24 % [24]. The main difference between Al-BSF and PERC structures is the full-area back surface field that is replaced by localized back surface fields. Additionally, a dielectric layer is added to passivate the Si surface, reducing surface recombination on the back side. It is also used with the purpose of having a high refractive index contrast with Si, causing it to act as an optical mirror with reflective values over 90 % [25]. This redirects non-absorbed photons back into the Si absorber, increasing the probability of absorption and the end goal of generating an electron-hole pair. This layer is commonly Al_2O_3, SiN_x or SiO_x. An illustration of the structure for a p-type Si solar cell is presented in Figure 3.2b, showing the contrast between the localized p^+ regions in PERC and the full-area back surface field of the Al-BSF cell design.

Several conventional approaches, such as Al-BSF or PERC, aim to improve passivation while maintaining local contacts, by reducing the contact area between Si and metal, minimizing recombination at the interface. The metalized surface area typically constitutes less than 1 %, depending on the design, but it is still a significant source of recombination [26]. Shrinking the metal contacts surface to local point

contacts can mitigate the issue. However, it introduces additional recombination due to longer transport paths for carriers and current crowding at the contact points, leading to power loss [25]. Passivating contacts address these problems by preventing direct metal-silicon contact while still allowing majority carriers to pass through freely without generating a barrier for majority carriers. This technology combines chemical passivation, by reducing the density of surface defects, with field-effect passivation, by creating an electric field able to repel minority carriers from regions prone to recombination at the surface. The contacts are formed using a thin passivating layer (a-Si, SiO_x, SiN_x, Al_2O_3) between the metal and the silicon wafer, increasing charge carrier transport and reducing recombination.

3.1 Poly-Si/SiO_x Passivating Contacts

The principle of polycrystalline silicon-based passivating contacts was introduced into solar cells in the early 1980s by Yablonovitch *et al.* [27]. The goal was to come up with alternative approaches to Si heterojunction structure approaches. In 2013, Feldmann *et al.* introduced the concept of Tunnel Oxide Passivated Contact (TOPCon), which is a poly-Si/SiO_x passivating contact architecture, where the main method of carrier transport is quantum tunneling through an ultra-thin interfacial oxide layer. This architecture sparked again interest in polycrystalline silicon-based passivating contacts [25].

To achieve a poly-Si/SiO_x passivating contact architecture, the following general processing steps are required:

1. growth of an interfacial oxide on top of the bulk (plasma oxidation [28], thermal growth [29], etc);
2. poly-Si directly grown on the cell or crystallization of an a-Si layer deposited through plasma-enhanced chemical vapor deposition (PECVD) [30], electron-beam physical vapor deposition (EB-PVD) [31], atmospheric pressure chemical vapor deposition (APCVD) [32];
3. a high-temperature thermal process at temperatures in the range from 700 °C to 1050 °C [25];
4. a hydrogenation process [33].

For this project, a thin SiO_x layer was used as a dielectric layer due to its broad bandgap of 8.9 eV, low surface state density, and tetrahedral coordination, which aligns well with the silicon structure [34]. This layer acts as a mechanism of chemical passivation. Depending on the thickness of the oxide layer, the following transport mechanisms will be dominant: quantum tunneling through the oxide or transport through pinholes located on the oxide. For oxides thicker than 2 nm, the probability of occurring quantum tunneling is too low, so the dominant mechanism is pinhole transportation [7]. For thinner oxides (< 2 nm), which is the case of the wafers processed in this project, the dominant process is quantum tunneling, although it may still exist carrier transport through pinholes.

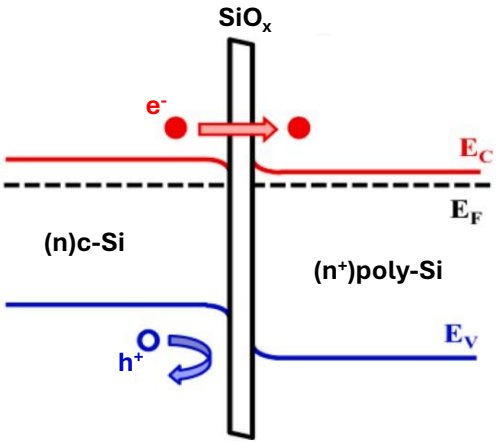

Figure 3.3: Band diagram illustration of a (n)-type poly-Si/SiO_x passivating contact, showing the highly doped poly-Si layer on the right, followed by the interfacial SiO_x layer and the absorber c-Si layer. In the illustration, e^- represents the majority carriers and h^+ represents the minority carriers.

The heavily doped poly-Si layer also plays a vital role in these passivating contacts. While the bandgap of poly-Si is similar to that of c-Si, heavy doping slightly modifies the energy bands of poly-Si. Together with the tunnel oxide layer connected to the c-Si, it induces a band offset. An example of how the tunneling would work in a poly-Si/SiO_x passivating contact is presented in Figure 3.3. While being an interfacial layer that helps passivate dangling bonds, in this case, the tunneling allows this structure to act as an electron-selective contact. In this case, electrons are the majority carriers, while holes are the minority carriers. Band bending in between (n^+) poly-Si and the (n) c-Si layer occurs due to different energy levels and this band offset will also act as an energy barrier that repels holes away from the surface of the contact. Since moving into the (n^+) poly-Si would require holes to gain energy and reach a higher valence band level, they are energetically unfavorable in this region. Even if some holes were able to tunnel through the oxide, their preferred energy state remains in the c-Si layer due to the valence band offset between c-Si and poly-Si. This effect helps keep minority carriers away from the electron-selective contact, ensuring efficient charge separation.

In this project, samples with an n-type poly-Si/SiO_x passivating contact were studied. An illustration of a solar cell with this technology on both sides is displayed in Figure 3.4. The absorber lies between an n-type passivating contact on the back side and p-type passivating contact on the front side, followed by an ARC layer on top, like Al_2O_3 or SiN_x, for instance.

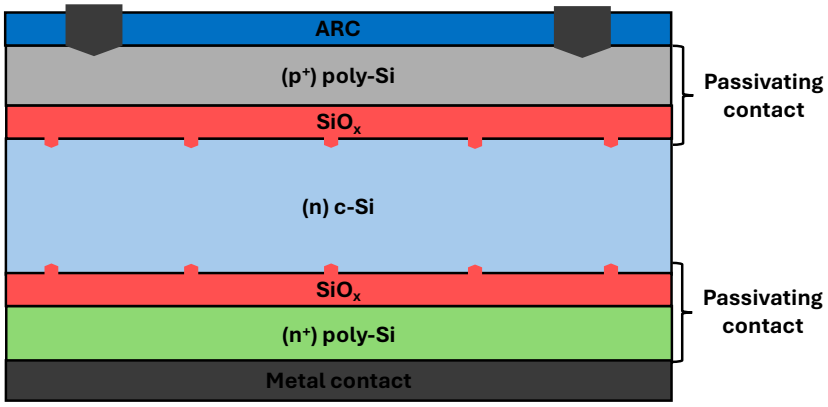

Figure 3.4: Schematic illustration of a solar cell with a poly-Si/SiO_x passivating contact on both sides, a n-type poly-Si/SiO_x passivating contact the back side and a p-type poly-Si/SiO_x on the front side, followed by an ARC on top (not to scale). Interruptions of the red SiO_x layer indicate possible pinhole transport regions.

3.2 Laser-Induced Crystallization for Passivating Contacts

Laser treatments are being investigated for various processes, including laser doping, laser contact openings and laser-induced crystallization, with the former being the main focus of this project. The use of lasers provides unique processing capabilities, including lower costs and fast processing times. For instance, in annealing applications, lasers need less energy compared with high-temperature furnaces, can be promptly switched on or off as necessary, and allow localized heating with a short duration due to the small laser spot areas. The actual temperature reached by a sample during the lasering will depend on the laser energy, the incident area, and irradiation time [35].

Recent investigations in 2020 on excimer laser annealing – a laser processing technique that uses ultraviolet (UV) excimer lasers to crystallize a-Si:H with thicknesses varying between 20 nm and 80 nm, showed that the crystallinity increases with the applied fluence [36]. Three lasers were used: xenon monochloride ($\lambda = 308$ nm), deep ultra-violet ($\lambda = 266$ nm), and krypton fluoride ($\lambda = 248$ nm). Among them, the sample processed with the deep UV laser at a fluence of $0.990\,\mathrm{J/cm^2}$ exhibited the highest degree of crystallinity among the three sources.[1] Further increments in applied fluence led to a decrease in crystallinity. In addition, surface morphology analysis revealed that fluences above $0.990\,\mathrm{J/cm^2}$ resulted in broken lattice structure, explaining the degradation in crystallinity at higher fluences. Furthermore, all three lasers showed better passivation with thinner 20 nm a-Si:H layers to the thicker layers. Regarding passivation quality, the laser process showed promise, achieving an iV_{oc} of 0.674 V with the 248 nm wavelength laser source.[2] However, traditional thermal annealing achieved better passivation, reaching a higher iV_{oc} of 0.697 V, indicating that the excimer laser annealing process still requires optimization in order to achieve higher passivation quality.

A recent study investigated the laser-induced crystallization of 12 nm (n^+) a-Si:H layer into poly-Si, using a laser with a 355 nm wavelength, a 25 ns pulse duration, and a Gaussian beam profile. The research focused on analyzing applied laser fluence and spacial pulse overlapping while keeping a constant spot diameter of 80 μm [13]. In this study, the overlapping of pulses was primarily controlled by varying the scanning speed and line spacing values. As the laser is rastered across the surface, depending on these parameters, a portion of the consecutive laser pulses may overlap with the previous one, resulting in pulse overlap. Results presented without hydrogenation processes showed that the optimally applied fluence was $0.34\,\mathrm{J/cm^2}$ and a pulse overlap of 50 %, correspondent to an iV_{oc} of 0.703 V, which corresponds to a temperature range near 800 °C from the simulation of temperature profile of Figure 3.5. The iV_{oc} profile with fluence and overlapping increased until the optimal value; from there, it dropped. It was suggested that the drop could indicate ablation, damaging the underlying interfaces. It was also stated that the Gaussian beam profile makes it difficult to control the fluence precisely as it creates a non-constant intensity throughout the beam area.

[1] Fluence is defined as the energy density applied per pulse.

[2] The implied open-circuit voltage (iV_{oc}) is an indicator of the passivation quality of a sample before metallization in solar cell fabrication.

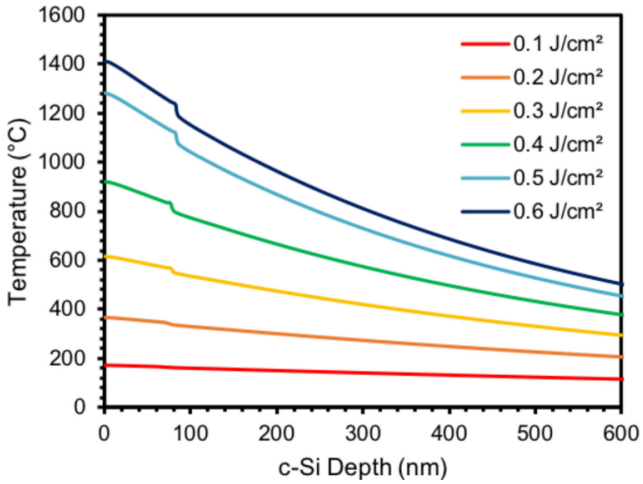

Figure 3.5: Spatial temperature profiles as a function of c-Si depth, simulated at $t = 25\,\text{ns}$ (end of laser pulse), showing peak temperatures reached for various laser fluences for each depth. The simulation was performed using a 355 nm wavelength laser model with 25 ns pulse duration. Sourced from Wilkes *et al.* [13].

Instead of using a pulsed laser source for LIC, one can conduct treatments with continuous wave laser sources, for instance. In 2022, Gawlik *et al.* investigated the laser power and the scanning speed of a diode laser with 808 nm of wavelength, a top-hat beam (the previous article used a Gaussian profile) with a rectangular line focus of $30 \times 0.1\,\text{mm}^2$, on 75 nm-thick (n) a-Si deposited by EB-PVD [31]. Two different scanning speeds of $15\,\text{mm/s}$ and $20\,\text{mm/s}$ were used, where the best results were achieved at $15\,\text{mm/s}$ within the range of $4.8\,\text{kW/cm}^2$ and $5.0\,\text{kW/cm}^2$, enabling an iV_{oc} value of 0.711 V in this range, after a hydrogenation procedure to enhance the passivation. Also, within this range, it was verified that minimal damage to the SiO_x layer below was done during crystallization.

This work focuses on developing a laser-induced crystallization process for highly phosphorus-doped a-Si layers by diode-pumped solid-state laser sources with a wavelength of 355 nm and 532 nm, to minimize recombination mechanisms by enhancing surface and interface passivation while increasing crystallinity and conductivity of the poly-Si/SiO_x passivating contact architecture for applications in silicon solar cells. Additionally, unless stated otherwise, poly-Si/SiO_x passivating contacts will be referred to simply as passivating contacts, as they are the only architecture under study.

Chapter 4

Experimental Methods

Silicon solar cell fabrication involves multiple processes, including etching, cleaning, layer deposition or growth, and contacting. Once the wafer is processed, the evaluation part begins, using several methods to characterize distinct properties of the cell. This chapter is divided into: Section 4.1, where a brief description of the steps the wafers went through prior to the processing of this project, Section 4.2 will describe the processing methods of samples and Section 4.3 will provide details about methods and devices used to characterize the samples throughout the project.

4.1 Wafer Description

All the wafers analyzed during this project came from the same bulk batch. The absorber is an n-type Czochralski grown silicon doped with phosphorus. It has a resistivity of $\rho = 10\,\Omega$cm, corresponding to a base doping concentration of $N_D = 4.5 \times 10^{14}\,\mathrm{cm}^{-3}$, an area of $156.5 \times 156.5\,\mathrm{mm}^2$ and thickness of $180\,\mu$m.

The surface of the substrate presented damage due to sawing the ingot and from laser labeling. These processes make the surface abundant in defects. In order to remove the damage defects, an anisotropic etching step was performed twice using a 80 °C heated KOH solution. The processes had a duration of 8 min, rinsing the samples with deionized water after. This resulted in a removal of around $12\,\mu$m of thickness on each side of the substrate. Next, an ozone cleaning [37] and Piranha cleaning [38] were performed, dipping the wafer in 2.5 % hydrofluoric acid (HF) until a hydrophobic state after each procedure. Figure 4.1 displays a flow diagram that summarizes the processing steps to achieve the desired samples. These three previously mentioned procedures are included in the wet chemical surface preparation step.

Right after the cleaning processes, a thermal oxide (SiO_x) with a thickness of 1.9 nm was grown on both sides of the wafer using a *Centrotherm tube furnace* [39]. The loading temperature was increased to 625 °C in an oxygen and nitrogen atmosphere with a flow rate of 1 slm. Oxidation was carried out for 10 min, followed by an annealing step at 625 °C for 30 min. Then, the wafers were cooled to 575 °C, before being unloaded.

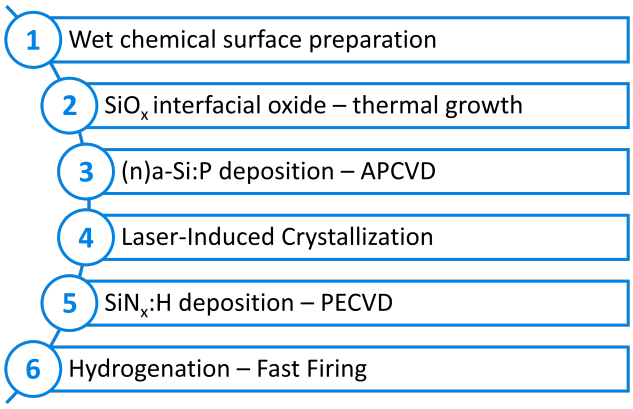

Figure 4.1: Summary flow diagram of the sample fabrication process. Steps 1–3 were conducted externally, while steps 4–6 correspond to the processing methods performed during the project.

To deposit (n) a-Si:P on top of the substrate, atmospheric pressure chemical vapor deposition (APCVD) is utilized. This is a cost-effective form of chemical vapor deposition as it works at atmospheric pressure rather than under vacuum. This process was carried out by an APCVD system from the SCHMID Group with a single deposition on each side of the wafer with a nominal thickness of 100 nm.

Figure 4.2 summarizes the layer structure of the samples used for this thesis and the respective thicknesses, including already the PECV-deposited SiN_x:H coating, described later on in Section 4.2.2.

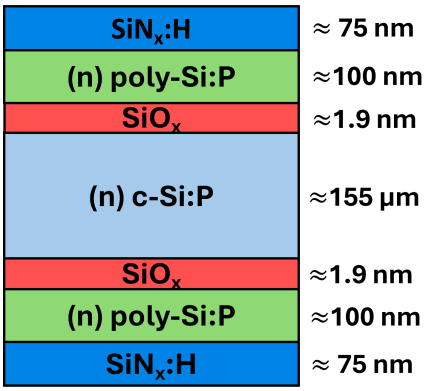

Figure 4.2: Schematic representation of the layer distribution of the analyzed samples with their respective thicknesses. In this project, it is expected to process (n) a-Si:P into (n) poly-Si:P using laser-induced crystallization.

4.2 Sample Processing

Laser-induced crystallization, the main focus of this study, is detailed in Section 4.2.1. Afterward, a plasma-enhanced chemical vapor deposition (PECVD) process for depositing SiN_x:H is outlined in Section 4.2.2. Finally, the hydrogenation process, which completes the sample preparation, is explained in Section 4.2.3.

4.2.1 Laser-Induced Crystallization

Laser-induced crystallization (LIC) of a-Si is the central processing step of this project. It is performed using an industrial device, *microSTRUCT C* from *3D-MICROMAC AG* [40]. This instrument is equipped with two nanosecond-pulsed laser units, operating at wavelengths of 532 nm and 355 nm. For

simplification, the 532 nm source will be referred to as green laser and the 355 nm one as UV laser. Both are diode-pumped solid-state lasers based on a laser medium of Nd:YVO_4. They use frequency coupling, in the case of the 532 nm source is frequency doubling, and in the 355 nm source is frequency tripling. Both lasers work at a repetition frequency of 50 kHz but present different power ranges, pulse duration, etc. With this repetition frequency value, it is possible to understand that a new cycle happens every 20 μs, having 50×10^3 cycles/s. The laser specifications are summarized in Table 4.1.

Table 4.1: Summary of relevant *microSTRUCT C* specifications for the green and UV laser sources used [40].

Laser source	Green	UV
Wavelength λ (nm)	532	355
Power range (W)	[0.0, 6.0]	[0.0, 3.2]
Pulse duration (ns)	30	20
Pulse frequency f (kHz)	50	50
Focal beam radius ω_0 (μm)	16.1	20.0
Rayleigh length z_R (mm)	2.01	1.30

Figure 4.3 presents a view of the laser beam path. It has a mechanical shutter right next to the laser source to control the passage or blocking of the beam, like an ON/OFF switch. Next, an attenuator regulates the beam intensity based on the input of the operator in the software. Following the attenuator, two mirrors redirect the beam toward a beam expander. After passing through the beam expander, the beam is redirected by a third mirror to the galvanometer scanning unit, which controls the rastering on the workpiece, followed by the objective lens that focuses the beam onto the wafer. Additionally, the XY table alignment feature, represented by the XY axis in the schematic, can be used during laser scanning. This system enables wafer positioning by moving the table along the X and Y axes.

Figure 4.4 illustrates how the laser scanning treatment is performed on a wafer. The software follows a predetermined order of columns and rows, with the number of divisions set by the operator and, in the presented case, a 3×3 array is set. The selected number of rows and columns determines the increment values for the chosen laser parameter intervals. Since wafer edges are more prone to a-Si dust accumulation due to wrap-around effects from the deposition technique [41], it was necessary to maintain a minimum distance of around 1 cm from the edge during scanning. This was determined macroscopically by simply identifying the region where no visible dust was present on the wafer. This results in nine lasered fields with an area of $\sim 4 \times 4\,\mathrm{cm}^2$ each.

The laser rastering process always starts from the lower-left corner, marked as "1st" in the illustration of Figure 4.4. Within each field, the laser pulses begin at the bottom left corner and move upward, forming vertical lines of pulses. To maximize coverage, considering that the beam spots are circular shaped, the rastering follows a hexagonal pattern, represented by the dashed blue in the "4th" field of Figure 4.4. The side length of the hexagon corresponds consistently to the set point distance value (L). Following this pattern, the rastering lines start at different programmed initial positions, improving coverage by reducing empty spaces compared to a strictly horizontal alignment of the lines [41].

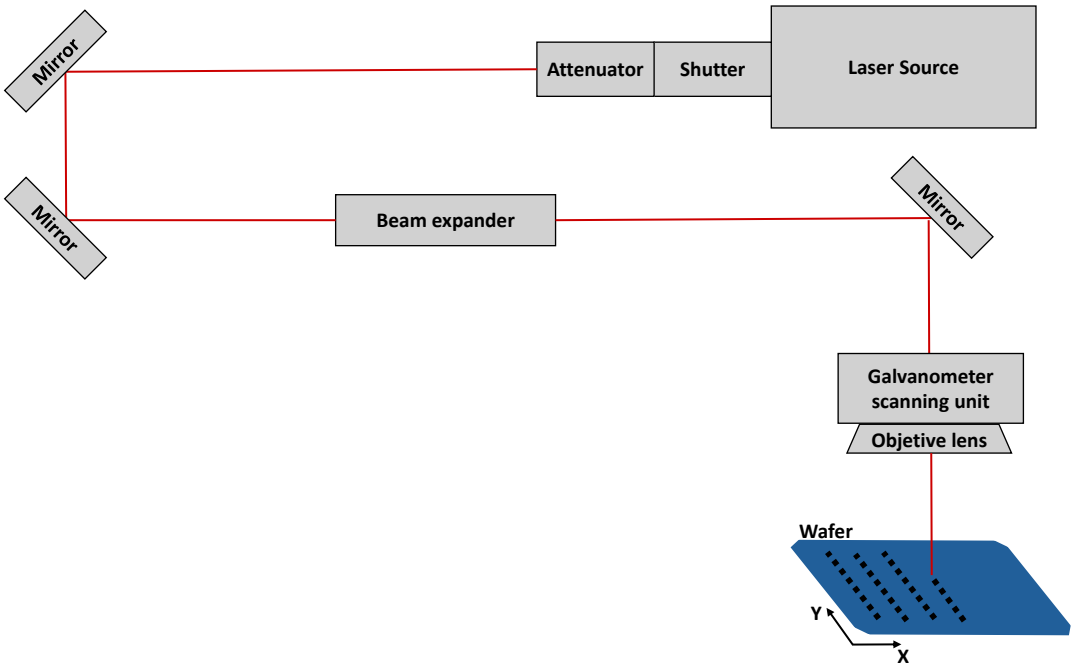

Figure 4.3: Schematic of the laser beam path. The components are following with its respective functions: the laser source generates the beam; the mechanical shutter acts as an ON/OFF switch, blocking or allowing the beam to pass; the attenuator controls the beam intensity; mirrors redirect the beam along the desired optical path; the beam expander adjusts the beam size; the galvanometer scanning unit controls the beam rastering based on a software programming following the pattern further described in Figure 4.4; the objective lens that focuses the beam onto the wafer, the XY table alignment system, represented by the XY axis, adjusts the wafer position.

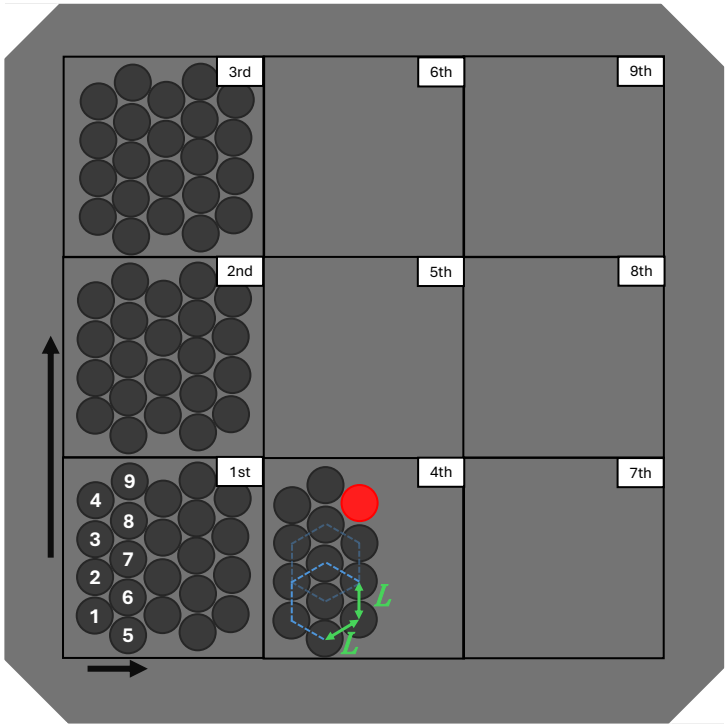

Figure 4.4: Schematic representation of a 3×3 array field for laser rastering on a wafer. The scanning begins in the square marked as "1st". Within each field, laser pulses transition vertically from the lowest to the highest point. Once the top is reached, the laser moves to the next line, scanning from bottom to top again, as indicated by the numbering inside the first field. The scanning lines do not all start at the same position, as the software follows a hexagonal pattern (blue dashed hexagon on the 4th square). Once the first square field is processed, the laser moves upward to the next one, continuing this sequence until reaching the top. It then starts a new column of fields from the bottom (the "4th" field).

Given values for power P, defocus D, and point distance between laser pulses L, it is possible to set the software program and laser-treat wafers with the *microSTRUCT C* device. During this work, scans were primarily performed by varying P horizontally across the wafer and D vertically, while maintaining a constant L for the entire wafer. Additionally, a few samples were processed by varying D and L while keeping the laser power fixed.

The energy distribution of a laser pulse is non-uniform, as the beam distribution is Gaussian, so a reference value is needed to define the beam radius ω. Equation (4.1) describes ω, in mm, as a function of D:

$$\omega(D) = \omega_0 \sqrt{1 + \left(\frac{D}{z_R}\right)^2}, \tag{4.1}$$

where ω_0 is the beam radius at the focal point, defined with the 2σ interval [41], which is about 95 % of the total intensity of the profile. Due to the Gaussian profile, the fluence is also not constant throughout the beam extent, being a function of the radial position relative to the center and the beam radius itself. The center point corresponds to the maximum fluence point $F_{\max}$. The fluence, which is defined as the applied energy per area unit, measured in $\mathrm{J/cm^2}$, at a given radial distance r, can be calculated as

$$F(r, \omega) = F_{\max} \exp\left(-\frac{2r^2}{\omega^2}\right). \tag{4.2}$$

However, in this device setup, the laser parameters that can be varied are the power, defocus and point distance. So, by defining the maximum fluence, one can approximate the fluence as uniform within the 2σ interval:

$$F(D, P) = \frac{2P}{\pi f \omega_0^2} \frac{1}{1 + \left(\frac{D}{z_R}\right)^2}. \tag{4.3}$$

This approach allows a better fit as it simplifies the analysis by treating the fluence as approximately constant in the 2σ interval [41]. Defining fluence for every individual point, while more accurate, would be more time-consuming, computationally intensive and not the focus of this work. It is important to note that the point distance parameter does not influence a single pulse. It only affects the percentage of overlap between consecutive pulses, so it is not a variable for the determination of fluence.

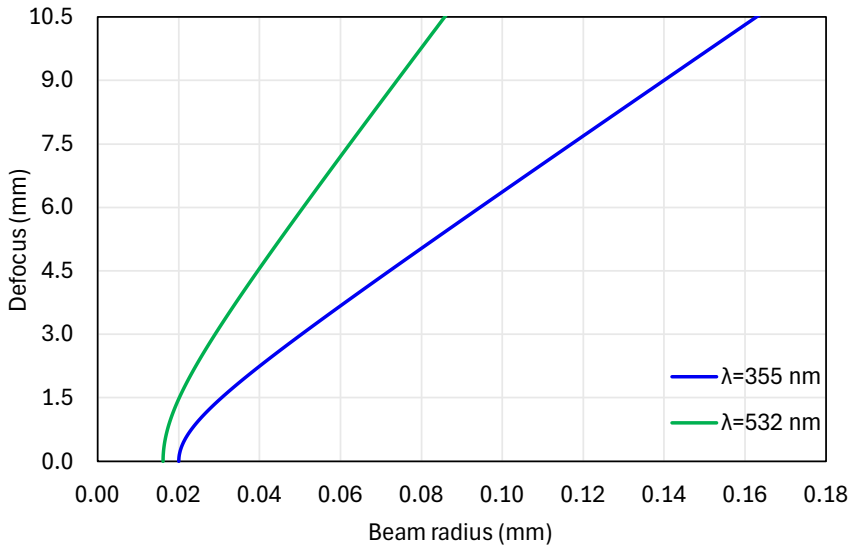

Figure 4.5: Defocus profile as a function of laser beam radius for the two lasers available. The correlation between the two variables is described by Equation (4.1) and the data device specifications of both laser sources are from Table 4.1.

Using the laser device specifications of Table 4.1 and applying Equation (4.1), a plot was generated to illustrate the correlation of the beam radius on the defocus, shown in Figure 4.5. As the table states, the focal beam radius of the green laser is smaller in comparison with the UV laser. Since the only difference between the green and UV source regarding Equation (4.1 is ω_0 and z_R, it is expected to have similar data profiles with a slight offset and inclination, as displayed in the plot.

In addition, by rearranging Equation (4.3) with the data of Table 4.1, plots of defocus as a function of power for key fluence values were generated for both the green and UV laser sources, as shown in Figures 4.6a and 4.6b, respectively. These curvilinear profiles allow a better understanding and visualization of how the correlation of applied laser parameters influences the laser processes. It is clear that, with the same laser parameters, it is easier to achieve higher fluences with the green laser compared with the UV laser.

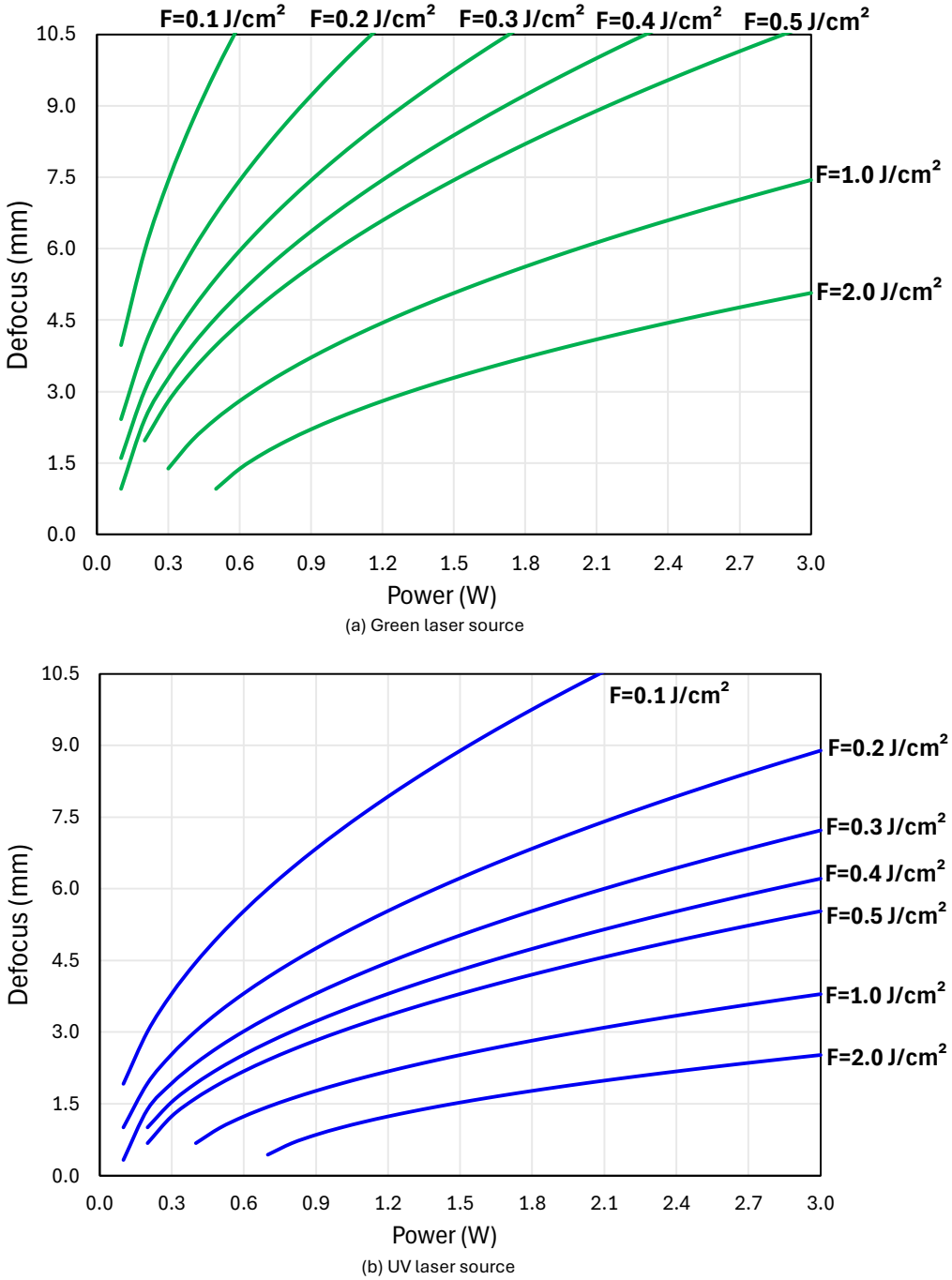

(a) Green laser source

(b) UV laser source

Figure 4.6: Defocus profile as a function of laser power, for several fluence values in the range of $F = [0.1, 2.0]$ J/cm^2, for the two lasers sources available: (a) green laser; (b) UV laser. The correlation between the plot variables Power and Defocus is described by Equation (4.3) and the data device specifications of both laser sources are displayed in Table 4.1.

4.2.2 Plasma-Enhanced Chemical Vapor Deposition

To deposit SiN_x:H using the PECVD method, SiH_4 and NH_3 are required as precursor gases. This gas mixture is exposed to a radio frequency source, creating an electric field between an anode and a cathode. The direct plasma is generated because the electric field accelerates the electrons, causing bonds in the gas molecules to break. This results in ions and free electrons that form a plasma. This plasma is formed by chemical reactive radicals that will react with the surface atoms of the wafer, leading to chemical reactions that result in the deposition of SiN_x. Some incomplete dissociated components are present as a result of the chemical reaction presented in Equation (4.4), like SiH or SiH_2, for example. These are absorbed into the surface, leading to a high hydrogen content.

$$3\,SiH_4 + 4\,NH_3 \longrightarrow SiN_x + 12\,H_2 \tag{4.4}$$

PECVD was used to deposit an estimated thickness of 75 nm SiN_x on both sides of the wafers. The device operated for this purpose was *PECVD Oxford Plasmalab System 100*. The sample is placed in a processing chamber with a load lock, which will help maintain a stable vacuum. Once the evacuation of air is set, the standard SiN_x recipe is run. The sample is transported mechanically, in an automatic way, to the reaction chamber, which is preheated to 400 °C and maintained at an approximate pressure of 100 mTorr to do the deposition. On a side note, the product of the chemical reaction (4.4) is denoted as SiN_x as the deposition process does not produce a strictly stoichiometric compound like Si_3N_4 but rather a mixture of silicon nitrides with different ratios.

4.2.3 Hydrogenation

For passivation analysis, the wafer surface was passivated by incorporating a 75 nm thick SiN_x coating via PECVD, as it contains significant amounts of hydrogen, as described in Section 4.2.2. Hydrogen will help to neutralize defects at the surface and within the bulk as well. By subjecting the sample to a high-temperature step, the passivation quality can be significantly increased [33].

The fast firing process was performed by a firing furnace to diffuse hydrogen from the surface layer (SiN_x:H) into the a-Si layer. This is a high-temperature short duration annealing process that helps dopant activation and recrystallizing silicon, commonly used in PV. The test recipes were set to peak temperatures ranging from 700 °C to 900 °C. The process consists of manually placing the sample on a moving belt after the instrument has been preheated by loading a proper recipe. Samples with sizes of $156.5 \times 156.5\,mm^2$ and $40 \times 40\,mm^2$ were fired. Additionally, the smaller samples were placed on top of a support wafer, to prevent metal contamination from the belt and improve temperature distribution across the smaller sample.

The measured firing temperature profiles illustrated in Figure 4.7 correspond to procedures with set peak temperatures of 800 °C and 875 °C, measured using a temperature tracker. During this project, the set peak temperature (theoretical value) will be referred to as the peak temperature. However, it is important to note that the device never actually reaches this value, as presented in Figure 4.7, with the actual measured peak temperature being lower than the set.

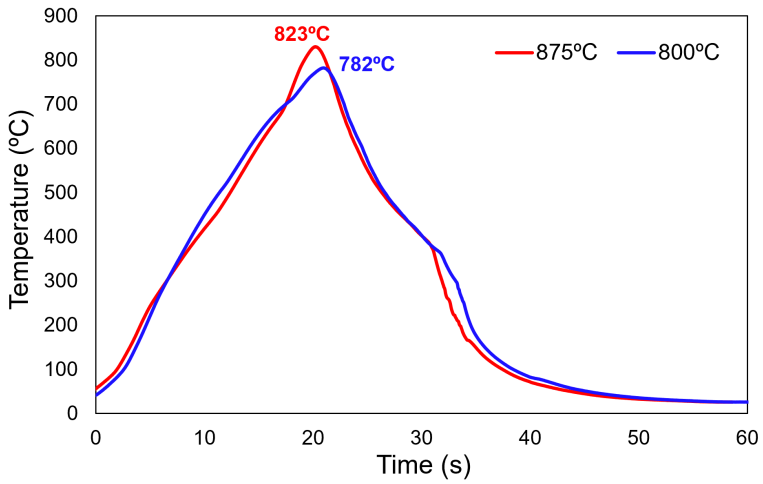

Figure 4.7: Measured temperature profiles during fast firing step, showing peak temperatures: 782 °C for a set temperature of 800 °C; 823 °C for a set temperature of 875 °C.

4.3 Characterization Techniques

The evaluation of passivation quality is detailed in Sections 4.3.1 and 4.3.2, which cover photoluminescence imaging and photoconductance decay measurements. Section 4.3.3 describes a spectroscopic technique used to analyze the elemental composition and layer structure of the samples. Section 4.3.4 discusses the X-ray diffraction method used to assess the crystallinity of the laser-processed a-Si layer. Finally, the four-point probe technique used to measure the sheet resistance of the surface layer is covered in Section 4.3.5.

4.3.1 Photoluminescence Measurement

The short measurement time, high spatial resolution, and contactless, nondestructive nature make photoluminescence (PL) imaging a widely used technique in PV. In this work, a custom-made device was used to assess the passivation quality of the samples through a colormap distributed in units of counts/s [42].

The PL measurement consists of exposing the wafer to a controlled light flux via LED until the rates of charge carrier generation and recombination reach equilibrium. The photons emitted from the sample's surface, generated through radiative recombination of excited charge carriers, are detected and counted by a charge-coupled device (CCD) camera for each pixel. The *LuSCI* software calculates a relative intensity for each pixel, producing a spatially resolved image of the wafer. An illustration of the PL imaging process is displayed in Figure 4.8. Higher intensity values indicate increased radiative recombination. Since radiative recombination is not the dominant process in silicon, the intensity can be directly linked to how effectively other recombination mechanisms, such as surface recombination, are suppressed. In other words, higher intensity will correspond to longer carrier lifetimes [43].

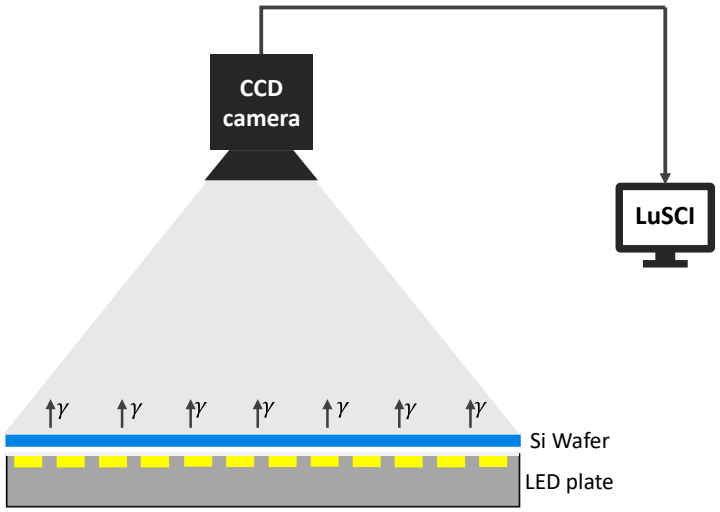

Figure 4.8: Schematic illustration of the PL process.

Since PL intensity strongly depends on surface recombination and charge carrier concentration, following Equation (2.6), the measurements are primarily relative, serving to map differences across regions.

To obtain absolute values such as effective lifetime, PL requires precise calibration. However, in high-lifetime samples, the PL signal becomes insensitive to changes, making absolute measurements unreliable. For low-lifetime samples, calibration can be performed using quasi-steady-state photoconductance measurements and Equation (4.9). While a calibration is theoretically possible for very low-lifetime samples, the count levels in the order of tens introduce significant uncertainty, making the calibration ineffective. Therefore, in this work, PL measurements were used merely as a mapping tool to compare relative differences between points on the samples.

4.3.2 Photoconductance Decays Measurement

Measuring the photoconductance of wafers allows a qualitative analysis of the passivation quality in a non-destructive way. It determines parameters such as implied open-circuit voltage (iV_{oc}). The instrument used for this purpose was the *Sinton Lifetime Tester WCT-120* [44], which uses a filtered xenon flash lamp as a light pulse source and an eddy-current conductance sensor to measure charge carrier lifetime. Measurements can be executed using the Quasi-Steady-State Photoconductance (QSSPC) method or the Transient Photoconductance Decay (Transient PCD) method.

When the flash lamp illuminates the sample, excess charge carriers are generated in the VB and CB of the semiconductor material, leading to a change in the conductivity $\Delta\sigma$. This induces eddy currents in the coil's magnetic field, which alters the inductance of the coil, as the inductive coil is located directly beneath the sample. These variations are then measured, allowing the software to determine the photoconductance, which in the end returns effective lifetimes τ_{eff} and iV_{oc} values, among other parameters. An illustration of the process is displayed in Figure 4.9.

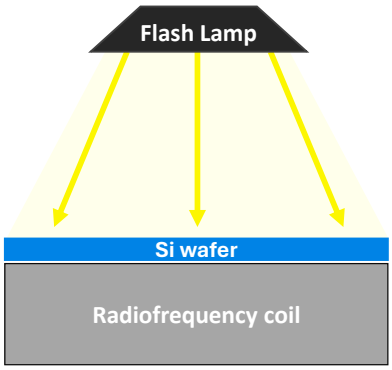

Figure 4.9: Schematic illustration of the PCD measurement process.

The change in conductivity of a sample can be expressed by Equation (4.5) [45]

$$\Delta\sigma = q(\Delta n_{\text{av}}\mu_n + \Delta p_{\text{av}}\mu_p)W, \tag{4.5}$$

with W the sample thickness, q the elementary charge, μ_n and μ_p the electron and hole mobilities, which for Si in particular, are well known [45]. The concentrations of photogenerated electrons and holes are identical, $\Delta n = \Delta p$, so the previous equation can be reformulated to determine the average excess minority carrier density (Δn_{av}), which applies to both types of carriers. It is presented in Equation (4.6)

$$\Delta n_{\text{av}} = \frac{\Delta\sigma}{qW(\mu_n + \mu_p)}. \tag{4.6}$$

Considering spatially uniform photogeneration and zero surface recombination [46]

$$\frac{d\Delta n_{\text{av}}(t)}{dt} = G - R = -\frac{d\Delta n_{\text{av}}(t)}{\tau_{\text{eff}}}, \tag{4.7}$$

where G and R are the generation and recombination rates, respectively. Based on this, the effective lifetime can be calculated via Equation (4.8), with G determined by a calibrated reference cell:

$$\tau_{\text{eff}} = \frac{\Delta n_{\text{av}}(t)}{G - \frac{d\Delta n_{\text{av}}(t)}{dt}} \tag{4.8}$$

Samples with a lifetime lower than 200 μs are measured with QSSPC. With this method, a longer flash with a duration of 2 ms is used and it can be assumed to be constant during the measurement [43]. Therefore, $G = R$ is valid at all times and there is no variation in the concentration of excess charge carriers over time. For this reason, Equation (4.8) can be approximated to Equation (4.9)

$$\tau_{\text{eff,QSS}} = \frac{\Delta n_{\text{av}}}{G}. \tag{4.9}$$

For samples with higher lifetimes ($> 200\,\mu$s), the transient mode is required. This mode uses a short flash, approximately 20 μs [43]. As the duration of excitation is short compared to the effective lifetime, it can be neglected, so the generation rate, $G = 0$. As a consequence, the lifetime of the minority carriers formula is simplified to the Equation (4.10)

$$\tau_{\text{eff,trans}} = -\frac{\Delta n_{\text{av}}(t)}{\frac{d}{dt}\Delta n_{\text{av}}(t)}. \tag{4.10}$$

Implied open-circuit voltage is also an important parameter for the characterization of solar cells. As PCD measurements are taken before the metallization of the wafer, its iV_{oc} represents an upper limit for the V_{oc} of the completed solar cell. It is defined in Equation (4.11)

$$iV_{oc} = \frac{k_B T}{q} \ln\left(\frac{\Delta n_{av}(\Delta n_{av} + N_{base})}{n_i^2}\right), \tag{4.11}$$

with the dopant concentration on the substrate material N_{base}. Equation (4.11) highlights the benefit of this iV_{oc} definition requiring only Δn_{av} at one sun and the wafer's dopant concentration. The measurements were all taken at 30 °C, which was the ambient room temperature.

4.3.3 Glow Discharge Optical Emission Spectrometry

Glow Discharge Optical Emission Spectroscopy (GDOES) is a spectroscopic technique used to study the element composition and layer structure of a sample. In this project, the device used was *GDA 750 HR*, and the complementary analysis software was *WinGDOES* [47]. The measurements have a duration of 60 s, and the key elements to be analyzed were predefined in the standard recipe.

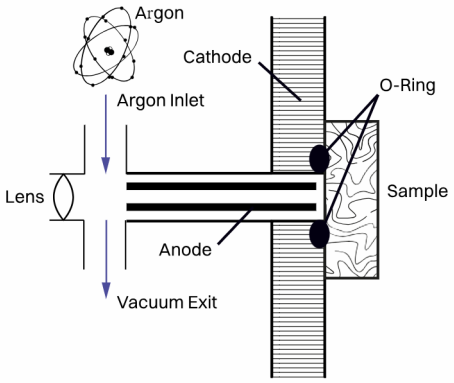

Figure 4.10: Schematic setup of the GDOES. Sourced from Spectruma [48].

The method consists of placing the sample on a glow discharge source filled with low-pressure argon, located in front of a hollow cylindrical copper anode, as presented in Figure 4.10. During the measurement, a high DC voltage is applied between the anode and the sample (which acts as the cathode). Due to the voltage potential, electrons are ejected from the surface of the sample and accelerated towards the anode. Through inelastic collisions with argon atoms, these will get ionized, resulting in argon cations and free electrons, which causes an avalanche effect that increases the density of charge carriers. This process triggers an avalanche effect, increasing the density of charge carriers and forming a glow discharge plasma.

The plasma will sputter surface atoms from the material enter the plasma, collide with the free electrons, get excited to higher energy levels, and emit characteristic light as they return to their ground state. The emitted light is directed to a slit, using a lens, onto a holographic grating. Then, the light intensity is measured by photomultiplier tube detectors, as a dimensionless relative intensity, resulting in a qualitative time-intensity profile for each element. It is possible to get quantitative measurements for this device, but it is necessary to perform a calibration, which is rather complex. For that reason, GDOES is used as a relative measurement during this work.

4.3.4 X-Ray Diffraction

X-ray diffraction (XRD) is a process that allows a better comprehension of the crystal structure of samples. The instrument used for this purpose was *Bruker Advance D8* [49]. The production of X-rays occurs within an X-ray tube, where electrons are emitted and accelerated by a heated cathode, striking a metal anode. During the XRD measurements, a voltage of 40 kV and a current of 20 mA were required, and the scanning mode used was *TwoTheta*.

The principle of this technique relies on the phenomenon known as scattering. The wavelength of X-rays is within the same order of magnitude as the distance between atoms. The incident beam strikes the crystal surface and gets reflected by the atoms, arranged in an ordered structure under specific geometric conditions. The resulting diffraction pattern is characteristic of the material and can be used to identify it, as well as to determine the geometry of its unit cells within the crystal structure. This radiation from the resulting diffraction is usually weak and often gets absorbed by the material. However, in some cases, those secondary X-rays have enough energy to avoid absorption and can be measured by a sensor. These scenarios apply when constructive interference of waves occurs. For that to happen, the incident X-ray has to strike the surface of the crystal at a specific angle, named Bragg angle, which is described by Bragg law, in Equation (4.12)

$$n\lambda = 2d\sin\theta, \tag{4.12}$$

where n is an integer multiple characterizing the order of reflection, λ is the wavelength of the beam, d is the interplanar distance, and θ is the angle of deflection. Poly-Si exhibits three distinct peaks at 2θ values for 28.5°, 47.5° and 56.5° [50].

Crystallite size is a parameter that helps distinguish silicon's different crystallization states. The Scherrer equation can be used to determine this variable [51]. In this work, the analysis software employs an approximate form of Equation 4.13 to calculate the crystallite size along a specific lattice orientation.

$$S_c = \frac{k\lambda}{\beta\cos\theta_B}, \tag{4.13}$$

where S_c is the volume averaged crystallite size, k is the Scherrer constant (dependent on the crystallite shape), β is the peak's full width at half maximum and θ_B is angular peak position (Bragg angle).

The size of the crystallites along an orientation plane can be obtained using methods such as Transmission Electron Microscopy, Raman Spectroscopy, or XRD. However, a comparison between techniques is generally complex because it has to take into account the different physical principles of each technique [52].

4.3.5 Four-Point-Probe

In this work, the focused electrical property was the sheet resistance R_{sh}. Obtaining the resistivity ρ of the top layer of the cell, displayed in Equation (4.14)

$$R_{sh} = \frac{\rho}{W}, \tag{4.14}$$

is more challenging due to the thickness W of the top layer is often unknown or difficult to measure accurately. Besides that, the sheet resistance has the advantage of being independent of the size of the square, which allows an easy comparison between different samples. Therefore, in this project, the sheet resistance was measured using the Four-Point-Probe (FPP) technique, and the instrument for this purpose was *TLM-SCAN*, from *pv-tools GmbH* [53].

The measurement setup is shown schematically in Figure 4.11. The system has a mapping mode in which each measurement position has to be defined in an XY coordinates list [53]. The probe head consists of four equally spaced, co-linear electrical probes. A constant current I is generated through the outer probes and applied on the surface of the wafer, which induces a voltage difference in the inner probes. This voltage is measured and used in Equation (4.15) to determine the sheet resistance [54]:

$$R_{\mathrm{sh}} = \frac{\pi}{\ln 2}\frac{\Delta V}{I}. \tag{4.15}$$

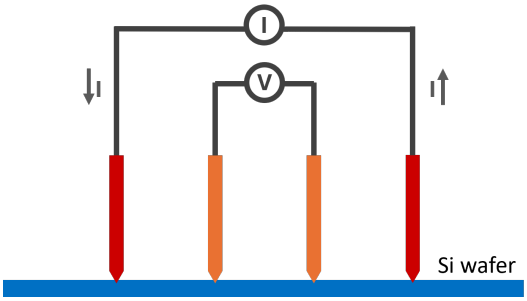

Figure 4.11: Schematic setup of the four-point probe.

Characterization techniques like FPP require direct contact with a conductive layer, so an insulating top layer prevents a proper measurement. Therefore, to analyze layer conductivity, the SiN_x coating must be removed for the hydrogenated samples. These samples were submerged in a solution with 10 % HF and deionized water for 20 min to remove this top layer, then left to air dry. This procedure required authorization to work with 10 % HF solutions, so it was carried out by an authorized staff person.

Chapter 5

Experimental Results and Discussion

This chapter presents and analyses characterization results for LIC samples. First, Section 5.1 compares samples treated with the green and UV laser sources. Subsequently, in Section 5.2, the focus shifts from the laser source used to the scanning techniques utilized by the laser equipment. After choosing the optimal laser source and scanning technique, Section 5.3 focuses on the laser parameters, such as power, defocus and point distance between laser pulses, and how they influence the passivation quality of LIC on the studied wafers. Sections 5.4 and 5.5 study and discuss properties like crystallinity and conductivity, respectively.

5.1 Comparison of Laser Sources

This section will discuss two distinct laser sources: the green laser source with $\lambda = 532\,\text{nm}$, and the UV laser source with $\lambda = 355\,\text{nm}$. Initially, experiments were performed using the green laser. Then, the UV laser was introduced to analyze and compare the influence of the wavelength of different laser sources. The samples of Section 5.1 did not receive any SiN_x deposition neither a fast firing step, thus, no hydrogenation process was applied.

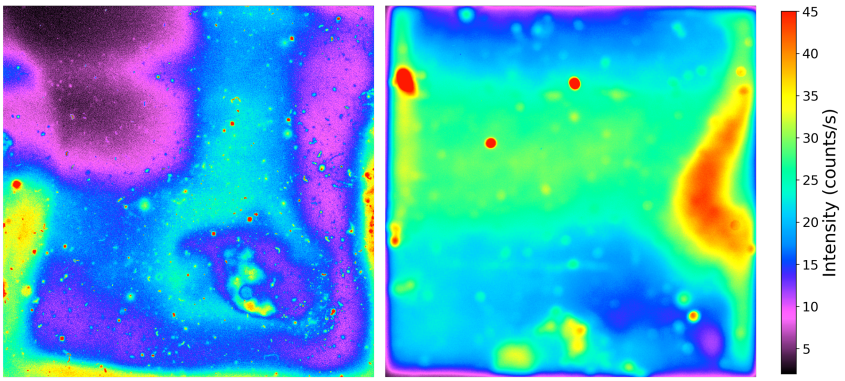

Figure 5.1: Reference PL measurements for two non-lasered wafers (as-deposited wafers). A mask was placed on top of the wafer during the measurements to exclude the edges of the wafer, focusing on the area of interest. The measurement area is approximately $125 \times 125\,\text{mm}^2$ dimensions.

A reference was established using a non-lasered wafer, where the top layer remained (n) a-Si:P, meaning that the samples did not undergo any heat treatment. Figure 5.1 presents two PL measurements of different non-lasered wafers. The data shows a scale in the order of tens, revealing very low passivation quality and, consequently, low carrier lifetimes. The low passivation quality of the wafer makes

it difficult to perform precise measurements due to few intensity counts. The observed inhomogeneous distribution both across the individual wafer and between wafers, even though all wafers are from the same batch, might result from these measurement difficulties. Alternatively, it could be attributed to non-uniform a-Si deposition, which is a possibility that has to be kept in mind.

PCD measurements were also performed across a non-lasered reference wafer, resulting in an average of $\langle iV_{oc} \rangle = (0.497 \pm 0.011)\,\mathrm{V}$. This value is expected for as-deposited wafers that have not undergone any annealing or hydrogenation process, and it is in agreement with the PL measurements in Figure 5.1. Besides that, the APCV-deposited a-Si has no hydrogen content itself incorporated.

GDOES reference measurements were conducted on an as-deposited wafer to analyze the element composition, presenting relevant element data signals in Figure 5.2. This reveals a higher concentration of phosphorus (dopant) and a peak in the near-surface region of the wafer compared with deeper layers, which is consistent with the APCVD (n) a-Si:P layer on top of the wafer. The oxygen peak confirms the presence of an interfacial oxide layer, which separates the a-Si layer from the c-Si substrate layer. In addition, the constant Si profiles are also expected, as all the layers are primarily composed of this material.

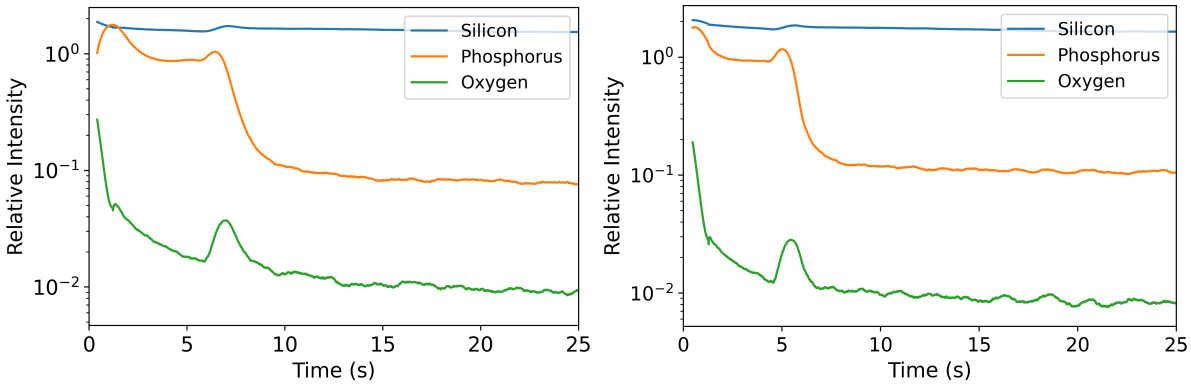

Figure 5.2: Reference profiles of GDOES measurements for a non-lasered wafer. Measurements were performed on the same wafer in distinct locations.

Wafers were laser-treated by applying broad intervals of laser parameters to study potential patterns related to the power or defocus intervals used. Figure 5.3 presents three samples, each one with a shorter interval of scanning laser parameters than the one before. In all samples, no pattern or gradient of intensity is visible, and the passivation quality remains consistently low. Note that in Figure 5.3a, the lower-right region displaying intensities around 25 to 30 counts/s (green-colored area) was not lasered. This is due to an limitation established in the laser software, which enforces an upper fluence threshold of $7.0\,\mathrm{J/cm^2}$. For those specific fields in the laser mapping, the combination of power and defocus exceeded this $7.0\,\mathrm{J/cm^2}$ threshold, preventing the software from lasering them.

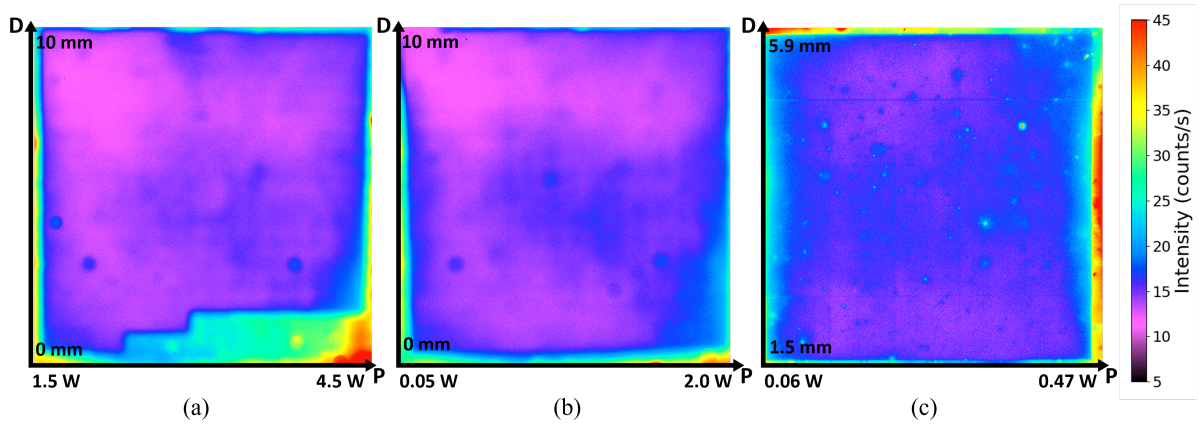

Figure 5.3: PL measurements for lasered wafers with the green laser, with the following parameters fields: (a) $P = [1.5, 4.5]$ W, $D = [0, 10]$ mm; (b) $P = [0.05, 2.0]$ W, $D = [0, 10]$ mm; (c) $P = [0.06, 0.47]$ W, $D = [1.5, 5.9]$ mm. The point distance was fixed at $L = 40\,\mu$m.

Using GDOES, the layer composition of several fields of the samples of Figure 5.3 were analyzed. Figure 5.4 shows measurements for various laser parameter combinations. None of the phosphorus signals of lasered samples from Figure 5.4a present the same shape as the reference signal, suggesting that the phosphorus concentration through the poly-Si layer deviates from the reference non-lasered sample profile. For two profiles, $P = 0.06$ W, $D = 5.9$ mm and $P = 0.47$ W, $D = 1.5$ mm, dopant diffusion is observed. The single peak near the 5-second mark suggests that the laser treatment may induce both indiffusion and outdiffusion of dopants, leading to the observed changes in those two profiles. This effect might be a consequence of rapid solidification during the lasering process, where the material transitions from the liquid to the solid phase, resulting in poly-Si dopant content redistribution.

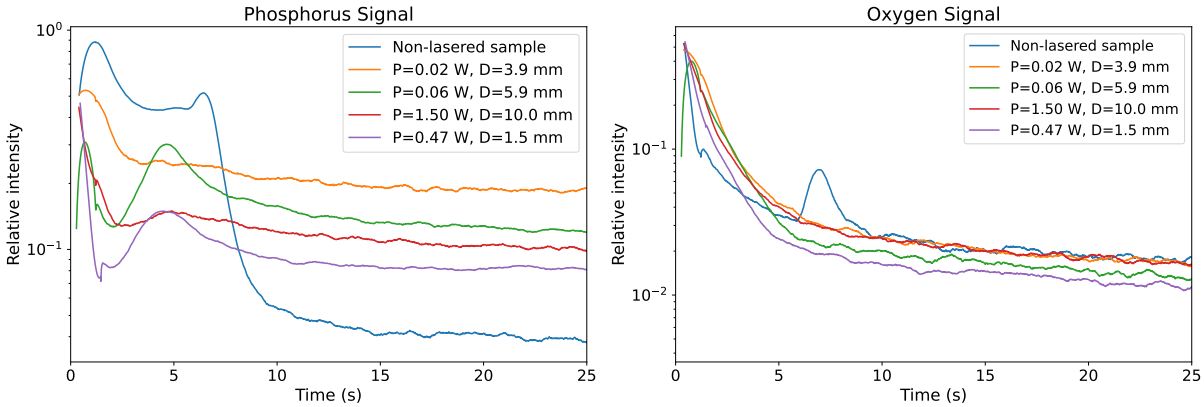

Figure 5.4: GDOES phosphorus and oxygen signal profiles for various applied fluences, using different laser parameters. The wafers were lasered with the green laser source with a fixed point distance of $L = 40\,\mu$m. A reference signal from a non-lasered wafer is also included for comparison. The legend is sorted by increasing fluence: $0.02\,\mathrm{J/cm^2}$ for $P = 0.02$ W, $D = 3.9$ mm; $0.03\,\mathrm{J/cm^2}$ for $P = 0.06$ W, $D = 5.9$ mm; $0.29\,\mathrm{J/cm^2}$ for $P = 1.50$ W, $D = 10.0$ mm; $0.98\,\mathrm{J/cm^2}$ for $P = 0.31$ W, $D = 1.5$ mm; $1.50\,\mathrm{J/cm^2}$ for $P = 0.47$ W, $D = 1.5$ mm.

Additionally, no oxide peak is visible in any lasered samples in the oxygen signal plot of Figure 5.4. On a first interpretation, one can think that the samples from the beginning may not had an oxide layer given that some measurements were taken in regions of low fluence, which shouldn't impact the wafer significantly. However, the reference as-deposited sample, from the same batch as the lasered samples, exhibits a clear oxide peak, confirming that the wafers have an interfacial oxide, eliminating this theory as a potential cause. One possible interpretation is that laser parameters may be too high, leading to

fluences that could melt and ablate the top layers, causing SiO_x to melt and dissolve in the molten Si, effectively removing the oxide layer.

An optical microscope was used to examine wafer surfaces and investigate the absence of interfacial oxide in all samples subjected to laser-induced crystallization. Figure 5.5a displays the surface of a non-lasered wafer, where the top layer remains amorphous silicon. For comparison, Figures 5.5b and 5.5c show regions on the same sample after laser processing, located on the spots with the lowest and highest applied fluence, respectively. In both images, there are signs of laser-induced melting, with clear laser spots. Figure 5.5c also reveals that the area around the laser spots appears more damaged than in Figure 5.5b, which is consistent with the fact that the fluence was higher in this region.

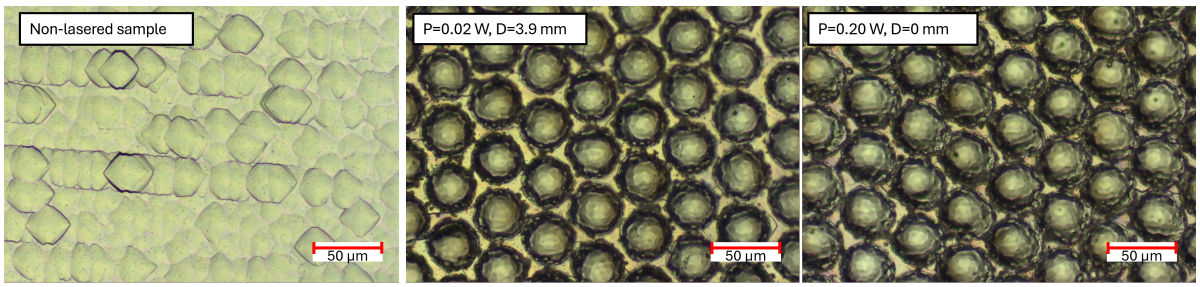

Figure 5.5: Wafer surface analyses by optical microscope images. (a) reference sample; (b) a lasered field with $P = 0.02\,\mathrm{W}$, $D = 3.9\,\mathrm{mm}$; (c) a lasered field with $P = 0.20\,\mathrm{W}$, $D = 0\,\mathrm{mm}$. The green laser source was used with a fixed point distance of $L = 40\,\mu\mathrm{m}$. Correspondent fluence and beam radius for each lasered sample: (b) $F = 0.02\,\mathrm{J/cm^2}$, $\omega = 0.035\,\mathrm{mm}$; (b) $F = 0.98\,\mathrm{J/cm^2}$, $\omega = \omega_0 = 0.016\,\mathrm{mm}$.

A software calibration of the green laser attenuation settings was performed, as there was a possibility of some sort of malfunction of the green source, to try to resolve the problem [41]. However, further processing and sample characterization revealed no noticeable differences with previous samples, ruling out this possibility.

Up until this point, only the green laser source was utilized. To compare the influence of the lasering process from both sources, a set of laser parameters was chosen to apply using both laser sources. In this case, the point distance was varied simultaneously with the defocus, keeping the laser power fixed at $P = 0.31\,\mathrm{W}$. This also aimed to analyze the impact of point distance on passivation. Both wafers were laser-treated with an array of parameters of $L = [20, 54]\ \mu\mathrm{m}$ and $D = [1.5, 3.9]\,\mathrm{mm}$. However, the laser sources have different values of z_R and ω_0 (shown in Table 4.1), so the range of applied fluence and beam radius used differed. Once more, it is seen how the laser properties drastically influence the fluence and beam radius used even though the same P, D and L are set, just like it was shown for the beam radius and fluence plots of Figures 4.5 and 4.6 of Section 4.2.1. The intervals are presented below:

- $\lambda_{\mathrm{green}} = 532\,\mathrm{nm} \rightarrow F = [0.33, 1.00]\ \mathrm{J/cm^2}$, $\omega = [0.020, 0.035]\ \mathrm{mm}$
- $\lambda_{\mathrm{blue}} = 355\,\mathrm{nm} \rightarrow F = [0.05, 0.44]\ \mathrm{J/cm^2}$, $\omega = [0.030, 0.093]\ \mathrm{mm}$

Macroscopically, the wafers present distinct appearances after the laser treatment. The wafer lasered with the green source shows visual marks of melting on the surface (a characteristic in all samples processed with this source). It also has a distinct color contrast compared to the non-lasered edges of the wafer. The wafers lasered with the UV source shows no noticeable difference between lasered and non-lasered areas spots.

The PL imaging of this comparison is present in Figure 5.6a and 5.6b, representing the green and UV laser source, respectively. These images exhibit distinct variations in mapping distribution. As for the

UV laser, the PL intensity around the edges of the lasered areas is lower compared with the central part, where there is a uniform intensity. The mask around the corners of the wafer can be speculated to be caused by the a-Si inhomogeneous deposition, suggesting that the laser came across different thicknesses of a-Si other than it was supposed, resulting in this contrast in intensity.

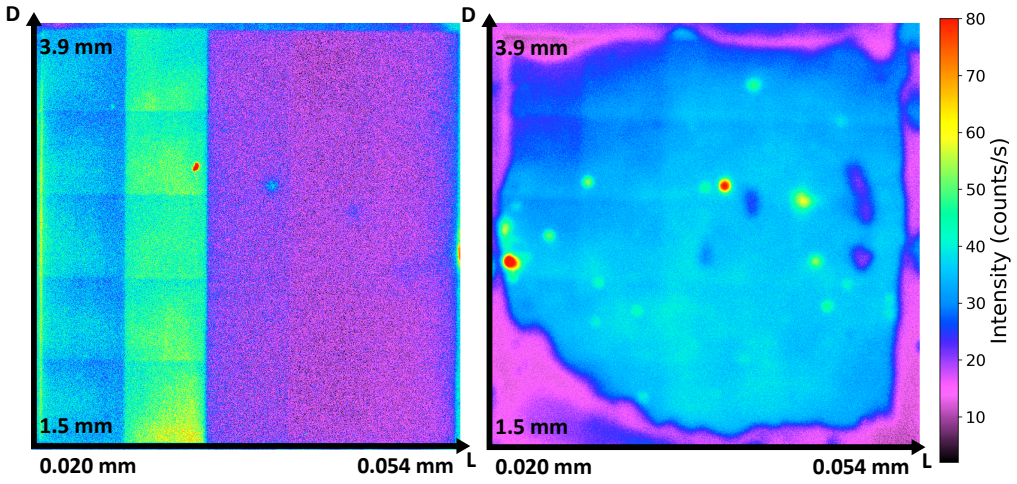

(a) Process using the green laser source (b) Process using the UV laser source

Figure 5.6: PL measurements comparison for following set laser parameters: $L = [20, 54]$ μm and $D = [1.5, 3.9]$ mm, with a laser power of $P = 0.31$ W, on a 5×5 field array. The wafers were lasered with the green laser (a), resulting in $F = [0.32, 0.98]$ J/cm^2 and $\omega = [0.020, 0.035]$ mm; and with the UV laser (b), resulting in $F = [0.10, 0.42]$ J/cm^2 and $\omega = [0.031, 0.063]$ mm.

Additionally, a clear contrast in PL intensity is observed in Figure 5.6a, for the sample treated with the green laser. This contrast appears to be a consequence of the the point distance used, as it is most noticeable in the horizontal direction. Although the scale is in the order of tens of counts, the highest intensity is associated with $L = 29$ μm and does not seem to have a significant improvement with defocus.

To further investigate the influence of the different laser wavelengths, GDOES measurements were performed on the same wafers of Figure 5.6, presenting the data signals on Figure 5.7. For the UV laser, it is evident that the phosphorus profiles are similar to the non-lasered sample, showing a highly concentrated region near the surface, followed by a narrow peak and a rapid but steady slope, indicating that the measurement went through the highly phosphorus-doped layer. In addition, the oxygen curves present a clear peak near the depth where the phosphorus signal abruptly decreases, the end of the a-Si layer and the presence of interfacial oxide. This confirms that the oxide layer is still present after lasering, a phenomenon absent in the green laser samples.

Working with the UV laser unit provides greater control over the laser treatment, allowing wafer processing without apparent damage on the underlying layers or causing unwanted surface ablation. It is important to note that a-Si exhibits distinct absorption coefficients for 532 nm and 355 nm, as displayed in the absorption coefficient spectrum of Figure 2.3. The absorption coefficient for the radiation for the UV laser is nearly 100 times higher than for the green, meaning that 532 nm radiation penetrates much deeper into the wafer with this unit. This suggests that, for the green source, a larger portion of radiation is transmitted through the a-Si layer rather than being absorbed. Since the SiO_x is a thin dielectric layer that presents minimal absorption and high transmission properties, the radiation will be able to reach the c-Si where the absorption coefficient is significantly higher for this wavelength, compared to a-Si. Additionally, it can also be speculated that dopant concentrations influence how energy is absorbed and dissipated, as a-Si is highly doped, meaning that free carriers can absorb some of the incoming radiation. However, the primary factor remains the difference in absorption coefficients at different wavelengths.

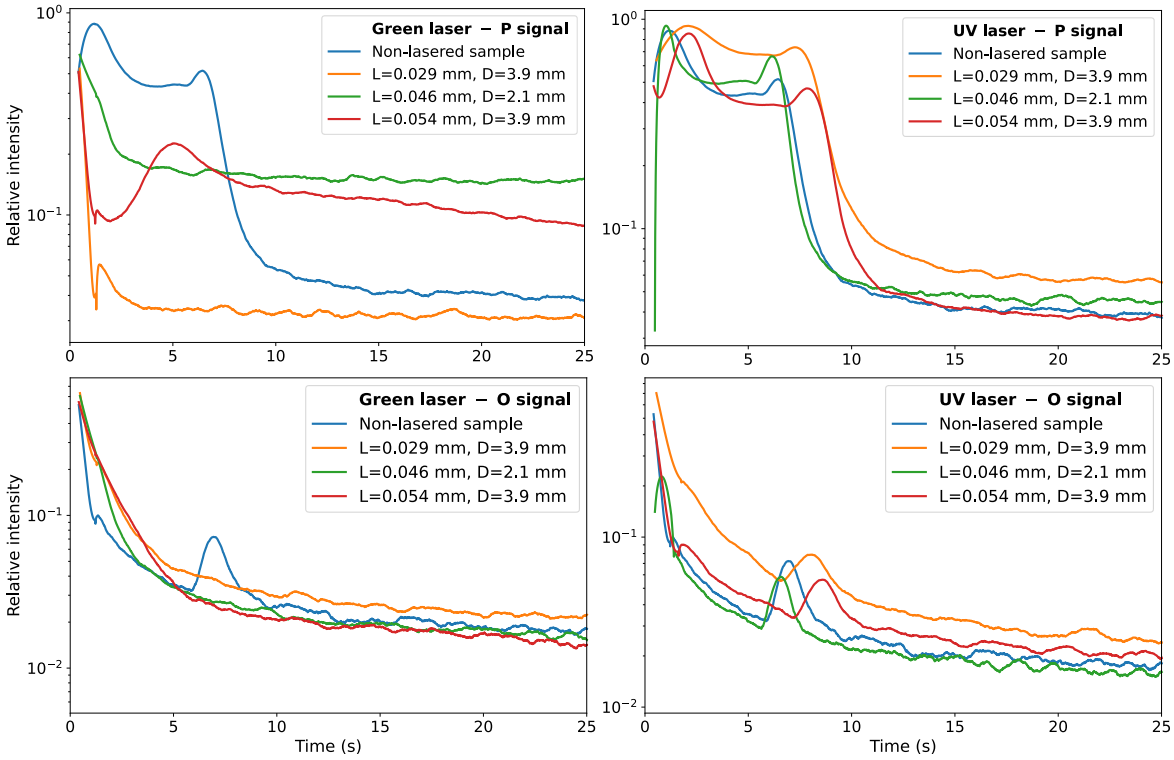

Figure 5.7: Phosphorus and oxygen profiles comparison for samples treated with the green laser (left) and with the UV laser (right). The GDOES measurements were performed wafers treated with a laser power of $P = 0.31\,\mathrm{W}$, while the defocus and point distance parameters were varied, as indicated in the plot legend.

Regardless of the underlying mechanisms, precise control over the laser process is essential, as surface ablation and layer damage are undesirable for this project. Since the UV laser enables laser treatment while preserving the layer structure, it was selected as the optimal laser source for the remainder of this study.

5.2 Comparison of Laser Scanning Approaches

This section compares two laser scanning methods on laser-processed wafers, both using the UV laser source. It mainly focuses on analyzing surface topography and element layer composition on different locations of laser-treated wafers, as well as comparing the influence of each approach on surface ablation and laser rastering uniformity. Two laser scanning approaches were considered: (i) the wafer remains stationary on a fixed table, and a galvanometer scanner performs the entire lasering process, adjusting from field to field and scanning within each field; (ii) an XY table alignment adjusts the wafer between fields, positioning the intended lasered field at the center beneath the galvanometer unit, while the galvanometer handles the laser processing within each individual field, being this second approach a slightly more time-consuming method comparing with approach (i).

Upon analyzing the surface topography and searching for potential laser damage, a wafer was lasered with a 6×6 array of $P = [0.5, 3.5]\,\mathrm{W}$, $D = [1.0, 4.0]\,\mathrm{mm}$ and $L = 40\,\mu\mathrm{m}$, using only the galvanometer (approach (i)). Two microscope images are displayed in Figure 5.8, both captured within the same field lasered with $P = 1.7\,\mathrm{W}$ and $D = 4.0\,\mathrm{mm}$. Optical microscope inspection revealed that within a single lasered field (processed with a single set of parameters), the surface presented noticeable topographical variations. Figure 5.8a was taken in the bottom section of the field, while Figure 5.8b corresponds to the upper (top) section of the same field. Laser ablation is observed in both sections, however, the

top section shows more pronounced damage, with the laser spots appearing clearer and deeper into the surface. Here, the applied fluence was $0.52\,\mathrm{J/cm^2}$, however, this phenomenon was still present even for fields where the applied energy density was lower. It appears that as the laser processes a pulsed line within a field, the laser damage increases. In addition, this issue is macroscopically visible, as a pattern of tonal contrasts can be observed within a lasered field and similarly across multiple fields. A possible approach to mitigate this issue while investigating its origin would be to select higher defocus values, which could improve scanning uniformity as the overlapping between consecutive laser pulses would increase. This would also minimize the impact of individual laser spots, as the energy per unit area would be lower due to the larger beam size.

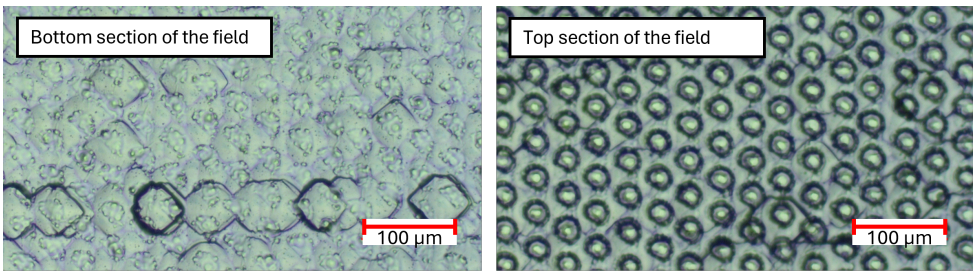

(a) (b)

Figure 5.8: Optical microscope analysis on bottom section (a) and top section (b) of a $2 \times 2\,\mathrm{cm^2}$ lasered field area. The field was processed with the UV laser source using the following parameters: $P = 1.7\,\mathrm{W}$, $D = 4.0\,\mathrm{mm}$, and $L = 40\,\mu\mathrm{m}$. Resulting fluence and beam radius are $0.52\,\mathrm{J/cm^2}$ and 0.065 mm. The laser scanning was performed using solely the galvanometer scanner.

Knowing that laser scanning using the galvanometer for the entire process was resulting in various degrees of surface ablation depending on the location on a field, it was needed to investigate the element composition of the layers across a single lasered field. For that reason, a sample was processed with larger squared areas, $6 \times 6\,\mathrm{cm^2}$, to perform GDOES measurements in different corner sections within a single laser field. The phosphorus and oxygen profiles of the measurement performed in the edges of the lasered field with $P = 1.7\,\mathrm{W}$, $D = 4.0\,\mathrm{mm}$, and $L = 40\,\mu\mathrm{m}$ are presented in Figure 5.9. It is visible that the measurement in the bottom left section of the field (Figure 5.9a) exhibits profiles that align more closely with the reference measurement previously shown in Figure 5.2. The top left measurement (Figure 5.9b) appears to have a more ambiguous oxide peak, likely due to noise interference, possibly indicating already some damage or diffusion of the content of this layer. Its phosphorus profile remains relatively stable. Meanwhile, the top right measurement (Figure 5.9b) shows no oxide peak and the dopant profile is more steady in comparison with the top left. This may indicate that, if the applied fluence is higher in this corner as suggested from Figure 5.8, more energy is applied resulting in enhancing the dopant diffusion of dopant into deeper layers, explaining its profile in the top right corner.

5. EXPERIMENTAL RESULTS AND DISCUSSION

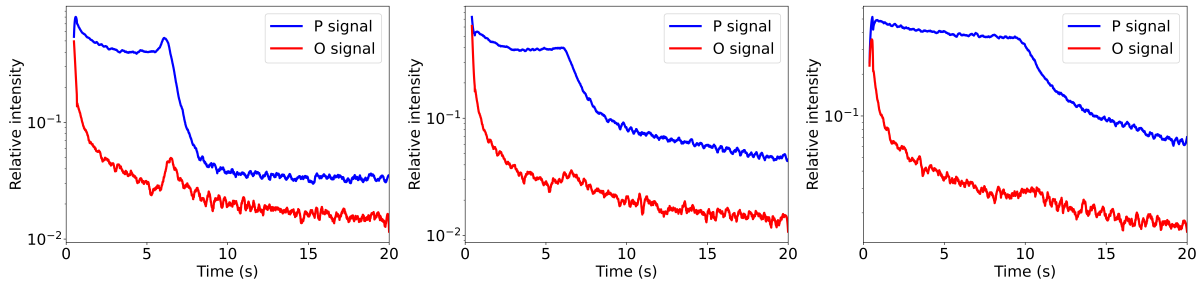

(a) Bottom left corner (b) Top left corner (c) Top right corner

Figure 5.9: Phosphorus and oxygen profiles obtained by GDOES measurements on a $6 \times 6\,\mathrm{cm}^2$ lasered field area, analyzing various locations. The field was processed using the following parameters: $P = 1.7\,\mathrm{W}$, $D = 4.0\,\mathrm{mm}$ and $L = 40\,\mu\mathrm{m}$, which corresponds to $F = 0.52\,\mathrm{J/cm}^2$ and $\omega = 0.065\,\mathrm{mm}$. This laser treatment used only the galvanometer to perform the laser scanning.

To further investigate the effect of position on laser ablation, a sample was lasered using a single set of parameters across the wafer in smaller lasered fields. The goal was to determine whether the same parameters would produce different topographies at different locations, within a field and in comparison between fields, and whether the contrast pattern remained visible. The wafer was processed with an 8×8 field array, using $P = 1.0\,\mathrm{W}$, $D = 4.0\,\mathrm{mm}$ and $L = 40\,\mu\mathrm{m}$, still with the scanning performed solely using a galvanometer (approach (i)). Microscope images were taken at several locations to analyze the wafer's surface. The images are presented in Figure 5.10, along with an 8×8 array field map indicating the measurement locations.

By examining the map displayed in Figure 5.10, one can compare the topography in four different top right field locations (e.g., letters A, B, C, F). It is clear that the surface damage produced by the laser significantly varies depending on its placement as this four sections show distinct topographies. For instance, while image C shows no apparent laser damage, melted spots are visible on F. Additionally, within a single square (e.g., E, F, G, H, I), there are drastically different topographies for this small lasered field (around $1.2 \times 1.2\,\mathrm{cm}^2$ area). Comparing the two top right field corner images (A, F) with two bottom left (D, H) from the correspondent field, the laser damage is noticeably different. This also suggests that the top right section of both individual lasered fields might be subjected to stronger energy densities, highlighting a possible non-uniformity scanning distribution.

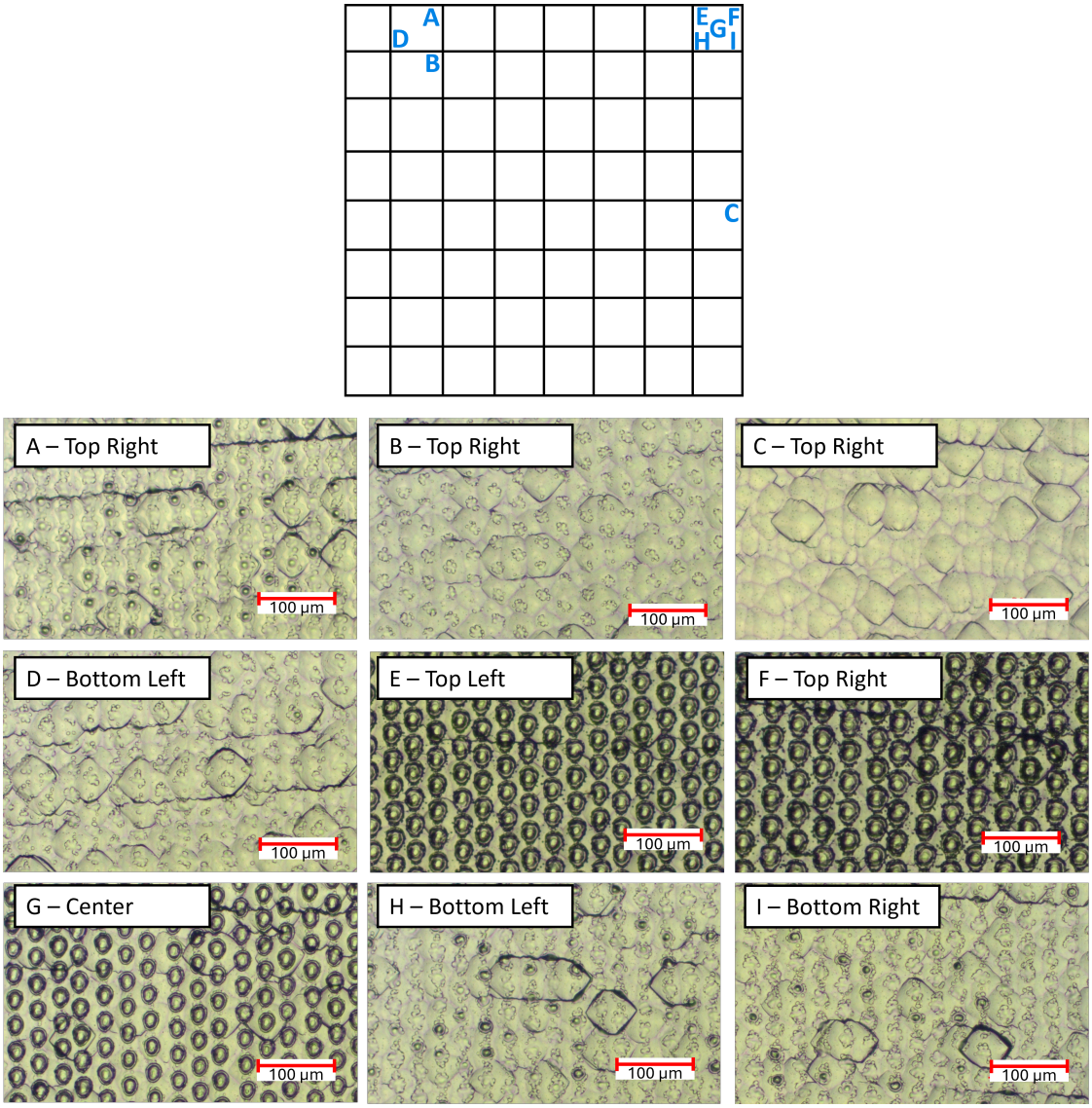

Figure 5.10: Optical microscope images captured on a wafer lasered with an 8×8 field array, using $P = 1.0\,\mathrm{W}$, $D = 4.0\,\mathrm{mm}$, $L = 35\,\mu\mathrm{m}$, corresponding to $F = 0.30\,\mathrm{J/cm^2}$ and $\omega = 0.065\,\mathrm{mm}$. Each field has an area of $1.2 \times 1.2\,\mathrm{cm^2}$. The 8×8 squares map indicates the location of each presented microscope image. This laser process used only the galvanometer to perform the laser scanning.

A factor that could impact this position issue, when processing the wafers using solely the galvanometer scanner, was the inclination of the chuck where the wafer is placed. If inclined to a certain degree, as the table is fixed, it could influence the height level across the wafer and, consequently, influence the defocus and the fluence. However, an internal experiment of the department was found and proved the inclination was of the order of micrometers, which is not significant enough to greatly impact the defocus, therefore excluding this possibility [41]. Another possibility for this behaviour is that, with the approach (i), due to the wafer's size and the fixed table, the galvanometer needs to adjust the beam's angle over a larger area. This can lead to steeper incident angles on some wafer regions, affecting the beam shape and its absorption by the wafer.

By adjusting a feature of the laser software to utilize the XY table alignment, the following wafers were processed using the laser scanning approach (ii). The galvanometer scanner performed the rastering within each field, and then the XY table alignment would move the next field to laser-treat to a central position relative to the galvanometer scanner. The procedures and measurements that were done for

approach (i) were now replicated with approach (ii) for comparison, meaning element composition was analysed again in different positions of a single lasered field. The GDOES measurements were conducted on the corner sections of a field lasered with $P = 1.7\,\text{W}$, $D = 4.0\,\text{mm}$ and $L = 40\,\mu\text{m}$, just like previously done in Figure 5.9. The results, shown in Figure 5.11, demonstrate significantly improved consistency in element profiles across different corners compared to Figure 5.9, which used the static table method. Additionally, no contrast pattern is observed in this sample by naked eye.

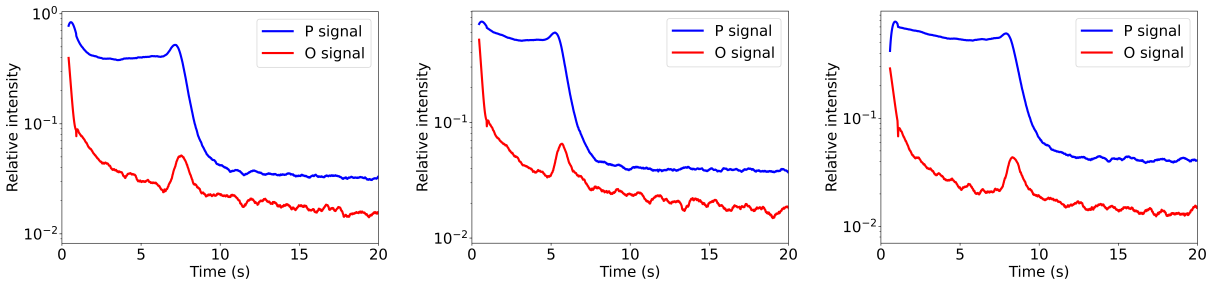

(a) Bottom left corner (b) Top left corner (c) Top right corner

Figure 5.11: Phosphorus and oxygen profiles obtained from GDOES measurements on various locations of a $6 \times 6\,\text{cm}^2$ lasered field. The field was processed using the following parameters: $P = 1.7\,\text{W}$, $D = 4.0\,\text{mm}$ and $L = 40\,\mu\text{m}$, which corresponds to $F = 0.52\,\text{J/cm}^2$ and $\omega = 0.065\,\text{mm}$. This laser treatment incorporated the feature of XY table alignment incorporated with the galvanometer method (approach (ii)).

To observe the presence of potential laser surface ablation now using the scanning approach (ii), another wafer was processed in an 8×8 field array and the same laser parameters ($P = 1.0\,\text{W}$, $D = 4.0\,\text{mm}$ and $L = 40\,\mu\text{m}$) as the wafer shown in Figure 5.10. The microscope images from all the locations tested (A to I) presented in the map of Figure 5.10 were now identical to the reference surface topography of the as-deposited sample (Figure 5.5a). With this scanning method, microscope observations showed uniform topography across all measurements, with no evidence of damage or melting of the surface.

Therefore, since approach (ii), which combines the galvanometer scanner within each field with the XY table alignment to adjust between fields, demonstrated an apparent uniform laser scanning distribution with no visible surface ablation and maintained the presence of the interfacial oxide, it was considered a more reliable approach and it was selected for the remainder of the project.

5.3 Passivation Quality Analysis

This section displays the results after analyzing wafers processed using each one of laser sources and the available laser scanning techniques. The UV laser source and the scanning approach with the XY table alignment feature were used for the remaining studies of the project. Further laser-treated wafers were tested with various laser parameter intervals. Here, a hydrogenation procedure with a SiN_x PECV-deposition and a fast firing step were introduced in several samples.

Section 5.3.1 will focus on analyzing different laser parameter sets and study how the correlation between them influences the passivation quality of the sample, after the incorporation of the hydrogenation process. The attention of Section 5.3.2 shifts into analyzing different fast firing peak temperatures and how that impacts the passivation. Finally, Section 5.3.3 presents and discusses the LIC results for passivation purposes in optimal conditions of the project, i.e., with the UV laser, performing the scanning with the approach combining the galvanometer and the XY table alignment (approach (ii)) and by fast firing at set peak temperature of $750\,^\circ\text{C}$.

5.3.1 Laser Parameters Analysis

To have a reference PL measurement, a 75 nm thick SiN_x layer was deposited, followed by a fast firing step on a non-lasered wafer. The firing process was conducted in a furnace with a peak temperature set to $T_{peak} = 875\,^{\circ}C$. This temperature will serve as the standard for subsequent wafers unless adjustments are required. Throughout this subtopic, the term hydrogenation will be used to refer to the SiN_x deposition and these conditions of fast firing. The PL imaging for the reference sample is shown in Figure 5.12. The scales reveal that the passivation quality improved three orders of magnitude with the SiN_x deposition and the fast firing step.

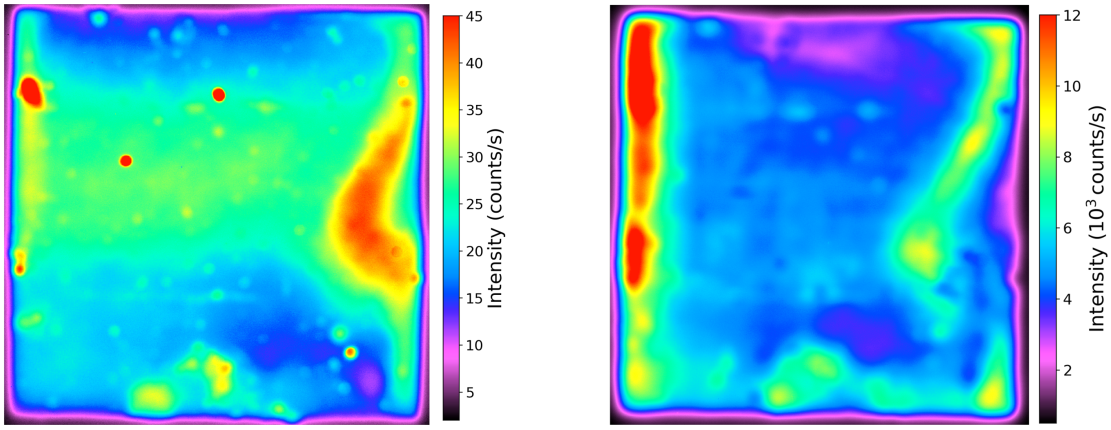

(a) Before hydrogenation

(b) After hydrogenation

Figure 5.12: Reference PL measurements for a non-lasered wafer (distinct intensity scales). The hydrogenation process on (b) included a 75 nm-thick SiN_x deposition and a fast firing step conducted at $T_{peak} = 875\,^{\circ}C$.

As a comparison, two wafers were processed by authorized staff using a tube furnace, a method of solid-phase crystallization process that is already well-established and proven to give high-quality results. The $156.5 \times 156.5\,mm^2$ wafers were loaded into the furnace at $800\,^{\circ}C$. Through a heating rate of $8\,^{\circ}C$/min, the samples were heated to $920\,^{\circ}C$. After waiting 30 min in a N_2 atmosphere, the samples were cooled down to $800\,^{\circ}C$, with a rate of $4\,^{\circ}C$/min [55]. Figure 5.13 presents the PL measurements, in which it is seen the largest scale of intensity during this study, with location measuring at least 100×10^3 counts/s. The samples are from the same batch as those used in the rest of this work, confirming that high-quality results are achievable within this batch with a 100 nm thick (n) a-Si:P layer. However, the data also reveals an inhomogeneous intensity distribution, with a distinct variation between samples. The sample on the left exhibits significantly better performance in the central region of the wafer, while the sample on the right shows high-intensity regions only near the left and bottom edges.

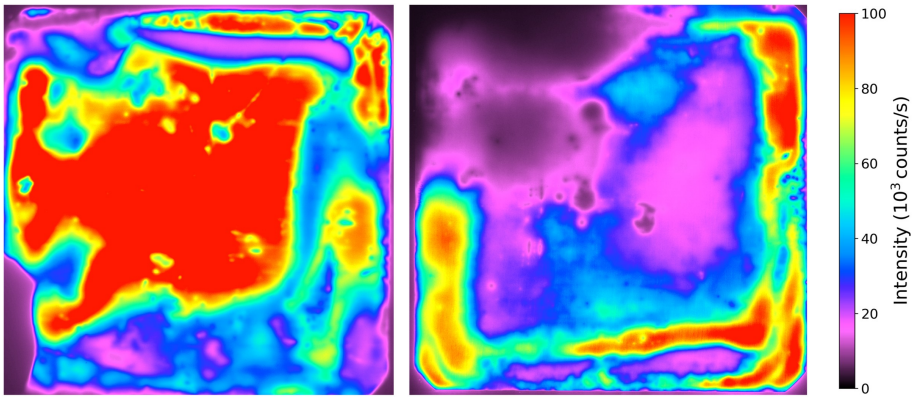

Figure 5.13: PL measurements for two wafers processed with solid-phase crystallization process well established. These samples did not involve any laser treatment, SiN_x coating, or fast firing step.

Fluence is a representative physical variable that combines the influence of power and defocus – Equation (4.3) – which are the laser variables mainly varied in this project. To study the results across several laser-processed wafers, PCD measurements were summarized in Figure 5.14. The fluence varied between $0\,\mathrm{J/cm^2}$, for a reference non-lasered wafer, and $0.55\,\mathrm{J/cm^2}$. Even though fewer measurements were conducted at higher fluences, the data trend seems to indicate that higher fluences are correlated with lower iV_{oc}. However, no clear pattern is visualized in the spectrum of results, as even wafers processed with different laser parameters but similar fluences present distinct results. For this reason, it is not possible to determine whether a parameter set is better than others.

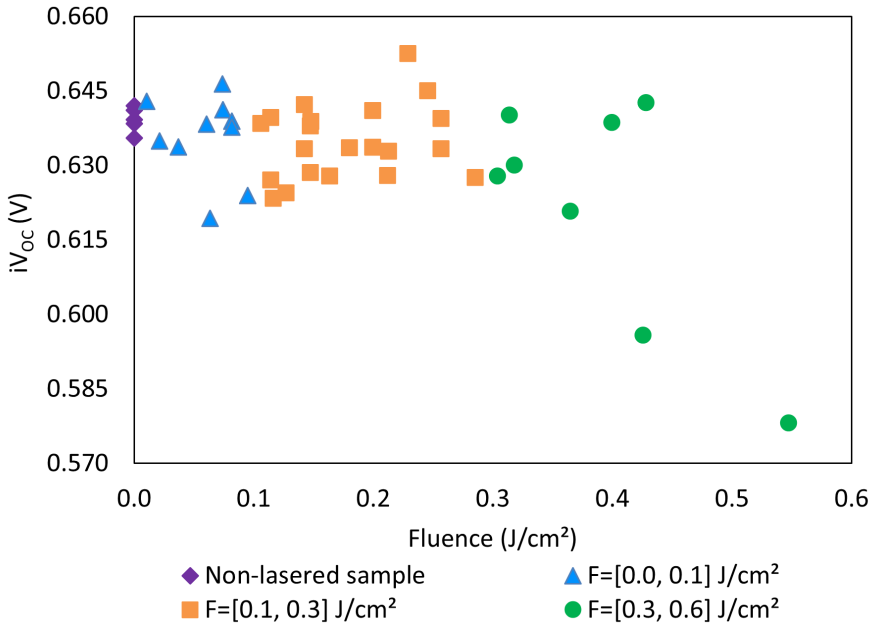

Figure 5.14: PCD measurements, presented as iV_{oc} versus fluence, performed on several laser-treated wafers. The data was divided into fluence intervals, for easier visualization. The laser parameters varied within the ranges $P = [0.2, 3.0]\,\mathrm{W}$ and $D = [4, 10]\,\mathrm{mm}$, with $L = 35\,\mu\mathrm{m}$. The samples were coated with a 75 nm thick SiN_x layer and underwent a fast firing step at a peak temperature of $T_{peak} = 875\,^{\circ}\mathrm{C}$.

While testing different parameter intervals, the PL mapping distribution shown in Figure 5.15a was observed for a wafer laser-treated with $P = [1.0, 1.8]\,\mathrm{W}$ and $D = [4.0, 8.0]\,\mathrm{mm}$, on a 3×3 array. It is visible that for $D = 4.0\,\mathrm{mm}$, the intensity is lower than the rest of the wafer. In order to understand if there is a possibility of an issue related to the galvanometer scanner or the XY table alignment, or if

it is just the defocus used, another wafer was processed with the same set of parameters, but with the defocus distributed in the reverse order, i.e., starting from 8.0 mm on the bottom to 4.0 mm on the top. The PL measurement is presented in Figure 5.15b. Comparing both mapping distributions, a similar pattern is observed, with the lowest intensity region consistently appearing at $P = 1.8\,\mathrm{W}$ and $D = 4.0\,\mathrm{mm}$ in both cases. The consistency of the distribution pattern across both wafers suggests that the laser processing is reproducible and independent of the location of the field in the wafer. Thus, the location issue possibility can be excluded and the XY table alignment feature can be considered to be working properly. Note that the intensity scale is very low, meaning further passivation quality analysis is focused after hydrogenation.

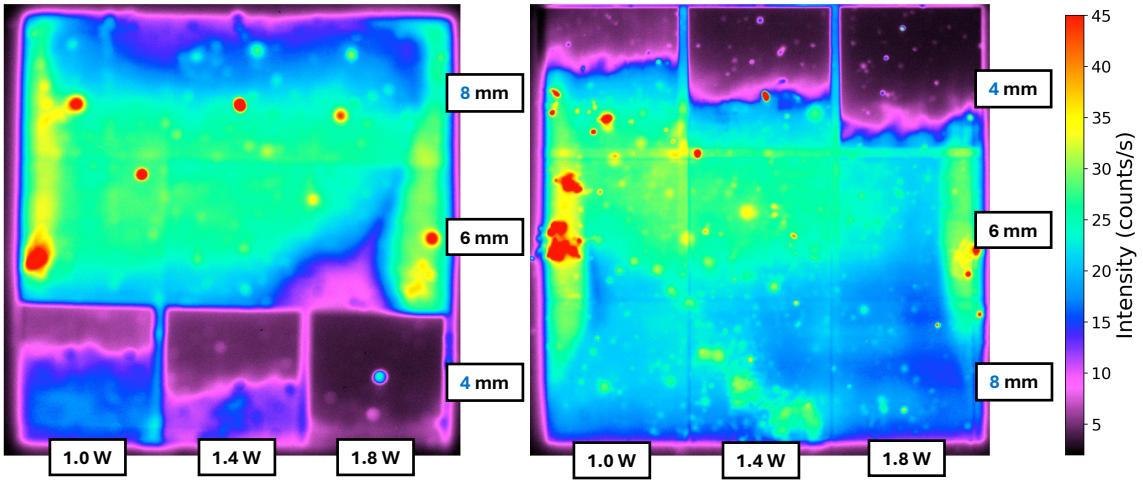

Figure 5.15: PL imaging measurements conducted on a laser-processed 3×3 array sample. The set parameters were the following: $P = [1.0, 1.8]\,\mathrm{W}$ and fixed $L = 35\,\mu\mathrm{m}$ for both samples, $D = [4.0, 8.0]\,\mathrm{mm}$ for the left side, and $D = [8.0, 4.0]\,\mathrm{mm}$ for the right side (same range, reverse scanning direction). Measurements were taken before hydrogenation.

During the lasering process, the wafer is placed on a ceramic plate with securing it in place. Since ceramic is an insulating material, the heat generated in the wafer is not transferred to the plate. In addiction, silicon is highly thermally conductive material, meaning it allows a fast heat dissipation. Despite the high pulse repetition rate of 50 kHz, thermalization occurs quickly, leading to a fast heat dissipation of the energy before the next nanosecond pulse is applied [41], having it already been analysed for other laser set-ups as well [13]. In another words, the substrate returns to the ambient temperature before the next pulse, ruling out thermal accumulation as a possible explanation for the intensity contrast observed for the fields with $D = 4.0\,\mathrm{mm}$ of both PL measurements of Figure 5.15.

Figure 5.16 displays PL images of two processed wafers, where L and D were varied, choosing the parameter intervals to contain similar fluence ranges. This approach aimed to study the effect of laser spot overlap and optimize the L value used for laser-treated samples in P vs. D arrays. After laser treatment, both wafers underwent a SiN_x deposition, followed by a fast firing step at $T_{peak} = 875\,^{\circ}\mathrm{C}$. The PL measurements show that the intensity distribution is within the same values range as the reference as-deposited samples after hydrogenation of Figure 5.12b. In both cases, a significant improvement in passivation quality is visible compared with samples measurements previous to hydrogenation, as expected of this passivation enhancing process. However, a gradient of intensity is visible in several lasered fields. The left and right edges present higher intensity counts; since this gradient intensity pattern was only present in nearly half of the lasered fields and has been observed in other wafers, it is not clear yet whether these results are influenced by the chosen laser parameters or are a consequence of inhomogeneity in the deposited a-Si layer.

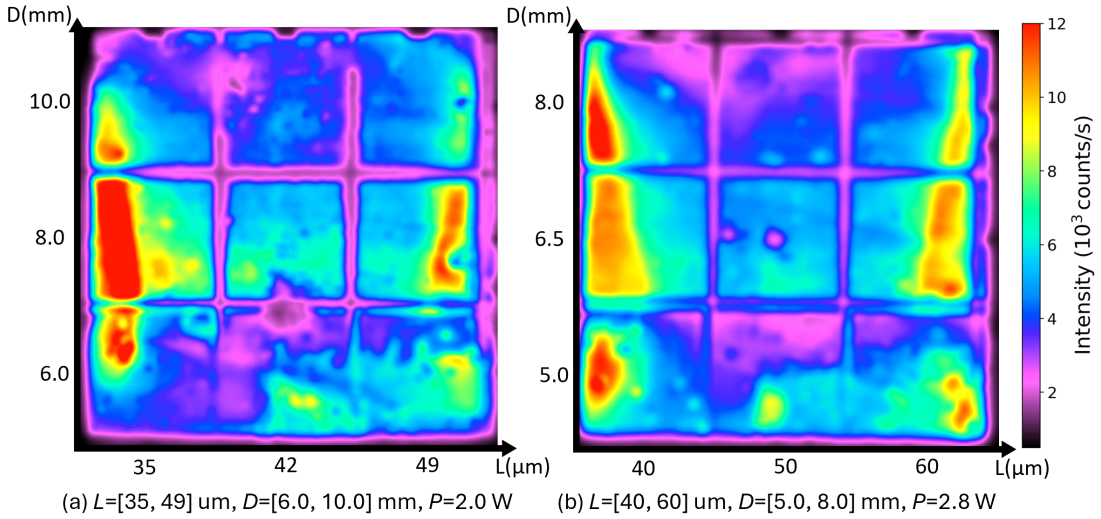

(a) L=[35, 49] um, D=[6.0, 10.0] mm, P=2.0 W (b) L=[40, 60] um, D=[5.0, 8.0] mm, P=2.8 W

Figure 5.16: PL imaging measurements of two laser-processed 3×3 array wafers. The resulting fluence and beam radius ranges intervals are: (a) $F = [0.15, 0.40]$ J/cm^2. and $\omega = [0.094, 0.155]$ mm; (b) $F = [0.16, 0.40]$ J/cm^2 and $\omega = [0.080, 0.125]$ mm. The measurements were conducted after hydrogenation with firing at $T_{\text{peak}} = 875\,^{\circ}$C.

To further analyze the influence of the point distance, PCD measurements for several L were conducted and they are summarized in in Figure 5.17, as iV_{oc} values as a function of applied fluence. While the number of measurements was limited to avoid processing too many wafers, the data obtained does not reveal any clear trends for different point distance values. As a result, the investigation shifted to focus only on power and defocus analyzes. Unless stated otherwise, $L = 35\,\mu$m was used as the standard value for subsequent LIC processes, as it is the value that presents a narrower spread out of iV_{oc} results and a higher average value.

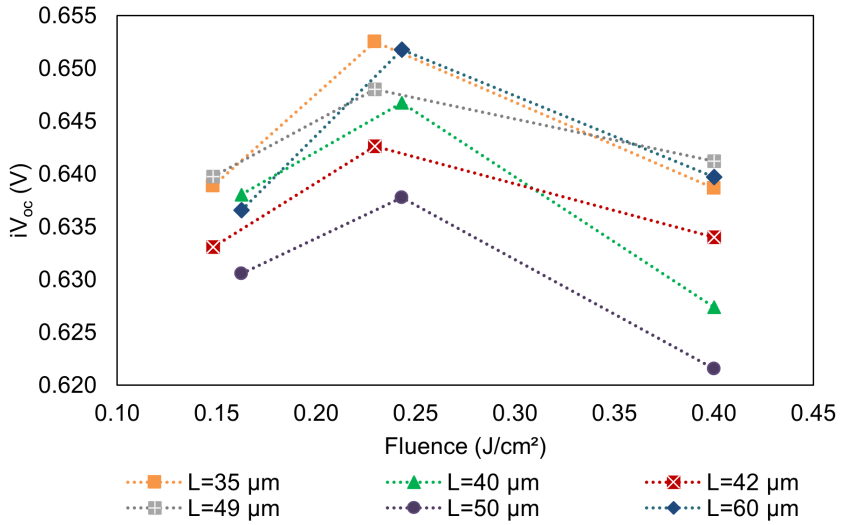

Figure 5.17: PCD measurements, presented as iV_{oc} versus fluence, performed on laser-treated wafers after a hydrogenation process, for several point distances from 35 to 60 μm. Defocus and power values varied between $D = [5.0, 10.0]$ mm and $P = [2.0, 2.8]$ W. These PCD measurements correspond to the same processed wafers showed in the PL measurements of Figure 5.16.

5.3.2 Fast Firing Temperatures Analysis

Up to this point, the peak temperature of the furnace used for the fast firing step was maintain fixed at $T_{\text{peak}} = 875\,^{\circ}\text{C}$. This section will focus on analyzing how the firing temperature affects laser-treated wafers and which temperature should be the optimal.

The same laser scanning array was processed in four wafers, all of them underwent a SiN_x deposition, and then they were fired at different temperatures. The PL measurements, presented in Figure 5.18, correspond to the following set peak firing temperatures: (a) 900 °C, (b) 875 °C, (c) 800 °C and (d) 750 °C. Knowing that the PL measurements are displayed in the same intensity scale, it is visible that lower firing temperatures produce better passivation. With the exception of the 750 °C sample, all measurements present improved passivation on the left and right corners, a phenomenon already detected before, speculated that is not a result of the lasering process. In addition, while some variations within the same lasered fields are noticeable, it seems that the lower-left section of the wafer for 800 °C and 750 °C, associated with a power of 1.0 W, exhibits better results than the rest of the wafer.

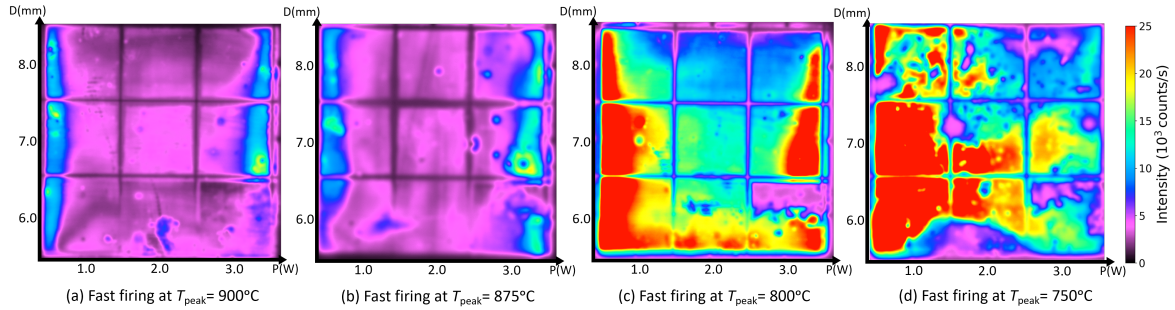

Figure 5.18: PL measurements for SiN_x coated laser-treated samples, with a followed fast firing step with different peak temperatures. The 3×3 laser parameter set remains consistent for all samples: $P = [1.0, 3.0]$ W, $D = [6.0, 8.0]$ mm, with $L = 35\,\mu$m.

As for the next step, PCD measurements were conducted to obtain more quantitative data from samples of Figure 5.18. Figure 5.19 present the iV_{oc} data as a function of laser fluence. Among the data, the wafer fired at 750 °C presents the highest iV_{oc} values, followed by 800 °C. Both present similar results distributions. From the other two curves, it can be suggested that the higher the temperature the worse the passivation quality of these wafers. Except two individual PCD measurements, 900 °C is the temperature with the lowest iV_{oc} results.

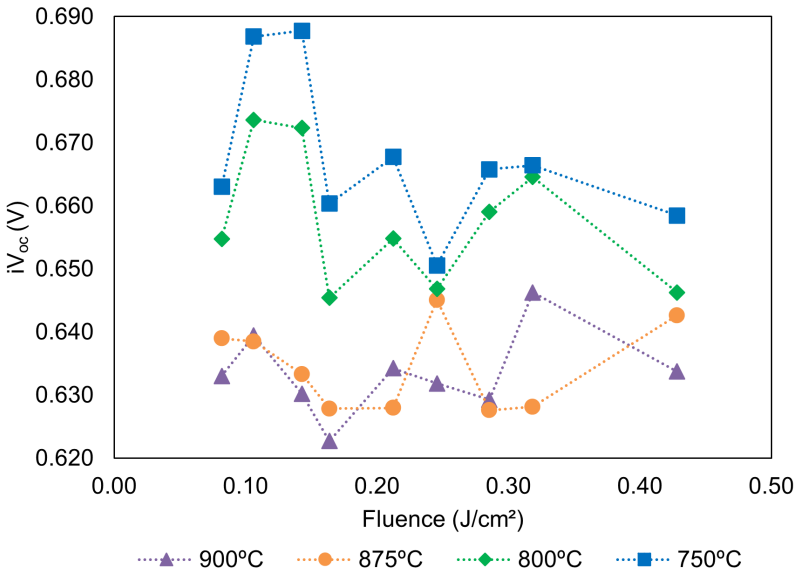

Figure 5.19: PCD measurements for SiN_x coated laser-treated samples, with a followed fast firing step with different peak temperatures. The 3×3 laser parameter set remains consistent for all samples: $P = [1.0, 3.0]$ W, $D = [6.0, 8.0]$ mm, with $L = 35\,\mu$m. Nine measurements were conducted for each wafer, corresponding to the fluence of each power and defocus combination.

Although the PL imaging results from Figure 5.18 suggest 750 °C was the optimal firing temperature, further tests were conducted, to gather more data. To prevent the usage of too many wafers, the analysis was carried out on smaller samples. The wafers were lasered with one set of parameters, on a 3×3 field array, coated with a 75 nm thick SiN_x, laser cut into $4 \times 4\,cm^2$ samples providing nine samples per wafer. Groups of three samples with specific locations were arranged to be fired at the same temperature. Note that the same combination of three locations was kept, for reproducibility purposes. However, between wafers, the temperature assigned to each group was rotated, to mitigate the influence of the inhomogeneity in the experiment. For firing peak temperatures of 700 °C, 750 °C and 800 °C, three sets were tested: a non-lasered wafer; two wafers treated with $P = 1.0$ W, $D = 6.0$ mm; $L = 35\,\mu$m; and a wafer processed with $P = 2.0$ W, $D = 6.0$ mm, $L = 35\,\mu$m. Figure 5.20 displays the iV_{oc} results of this experiment. An obvious variability of results is observed, despite the only variable within each dataset being the $4 \times 4\,cm^2$ sample's location on the wafer.

While the 800 °C dataset of Figure 5.20 presents less discrepancy of iV_{oc} values, it is also the one with the lowest iV_{oc} results. Between 700 °C and 750 °C, from the available data, both produce comparable outcomes and are valid options. The highest registered iV_{oc} belongs to 700 °C. Although a metallization step was not a part of this project, for the fabrication of a complete solar cell it is an essential step. Temperatures above 700 °C are more commonly used for peak firing temperatures, according to literature [30]. As a result, from this point on, 750 °C was defined as the default peak temperature for the fast firing procedure.

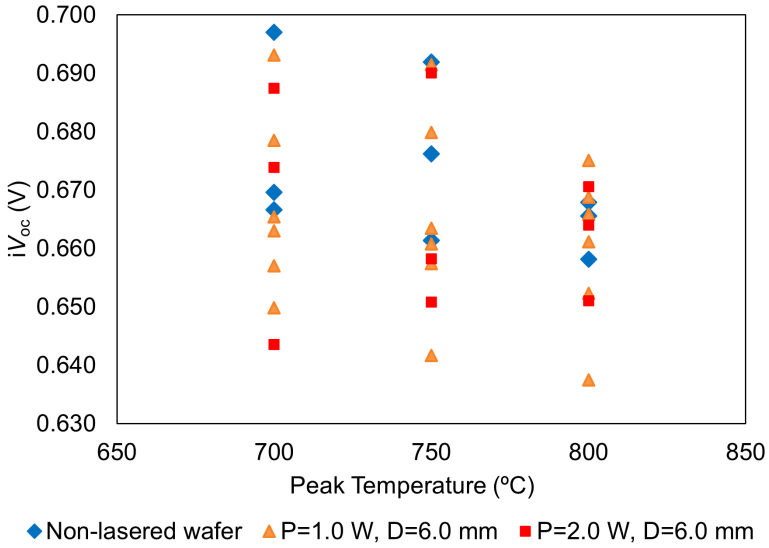

Figure 5.20: PCD measurements on samples hydrogenated with different peak firing temperatures, expressed iV_{oc} plotted as a function of peak temperature. The entire wafer was processed using a single parameter set, with lasering performed in 3×3 square arrays. Afterward, the wafer was coated with 75 nm thick SiN_x, laser-cut into $4 \times 4\,cm^2$ samples, and fired in different temperatures. The data of non-lasered wafer that went through the same laser-cutting and hydrogenation is also included.

5.3.3 Laser-Induced Crystallization Under Optimal Conditions

The left side of the wafer consistently shown better passivation results after hydrogenation. To understand if this originates from the wafer itself or if it is due to the parameters used during lasering, a laser array was applied to two samples with the same parameter intervals but reversed orders. A wafer was treated with a combination of $P = (1.0, 2.0, 3.0)\,W$ and $D = (6.0, 7.0, 8.0)\,mm$, while the other was the reversed combination to change the location, so $P = (3.0, 2.0, 1.0)\,W$ and $D = (6.0, 7.0, 8.0)\,mm$. PL and PCD measurements are shown in Figure 5.21 and 5.22, respectively.

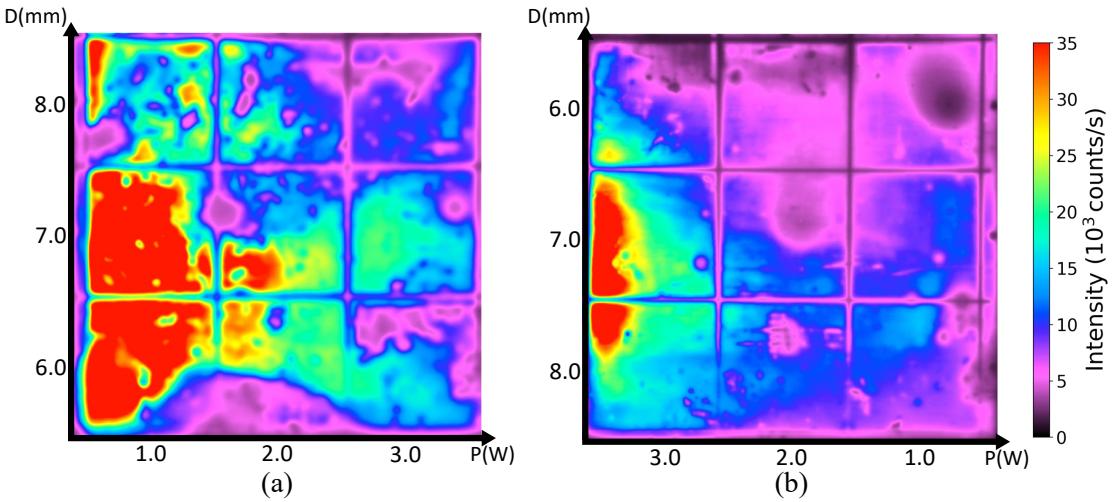

Figure 5.21: PL measurements conducted on laser-processed 3×3 array wafers. The wafers were processed using the following set of parameters: (a) $P = [1.0, 3.0]\,W$, $D = [6.0, 8.0]\,mm$; (b) $P = [3.0, 1.0]\,W$, $D = [8.0, 6.0]\,mm$ (reversed direction parameter array). The point distance was kept constant at $L = 35\,\mu m$. Measurements were taken after hydrogenation at $T_{peak} = 875\,°C$.

Despite equal parameters, the PL images of Figure 5.21 demonstrate that the left side of both wafers exhibited superior passivation, independently from the parameters used, confirming the assumption that

this region provides better results than the rest. However, within these same field locations, $P = 1.0\,\mathrm{W}$ results higher intensity compared to $P = 3.0\,\mathrm{W}$, suggesting that $P = 1.0\,\mathrm{W}$ may be more suitable for achieving improved passivation.

Analyzing in a more quantitative matter, PCD measurements (Figure 5.22) show the discrepancy of $\mathrm{i}V_{\mathrm{oc}}$ values for the same parameters lasered on different locations. To be able to discuss and compare parameter combinations fairly, future experiments should involve lasering the entire wafer with a singe set of parameters to mitigate the positioning issue. This will redirect the focus of the study more to the left region of the wafers allowing us to possibly compare fairly laser parameters even with inhomogeneous layers existing in the wafers, minimizing the influence of position as a variable.

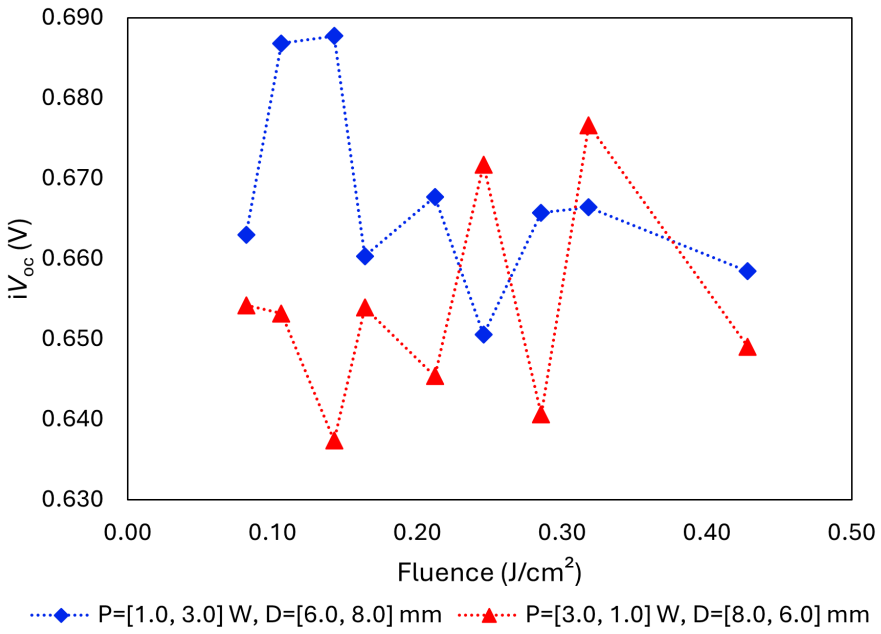

Figure 5.22: PCD measurements of two wafers lasered with the same interval of parameters but displayed in reversed order on the wafer. The applied set was $P = [1.0, 3.0]\,\mathrm{W}$ $D = [6.0, 8.0]\,\mathrm{mm}$ with $L = 35\,\mu\mathrm{m}$. Measurements were taken after hydrogenation.

From Figure 5.21, it can be observed that, when comparing both laser arrays, the passivation quality provided by the parameters $P = 1.0\,\mathrm{W} \wedge D = 6.0\,\mathrm{mm}$ is superior to $P = 3.0\,\mathrm{W} \wedge D = 8.0\,\mathrm{mm}$ at the same wafer location (bottom left section). Therefore, this parameter combination was the starting point for experimenting lasering an entire wafer with a single set of parameters. In addition, knowing that the fluence applied to the wafer by 1.0 W of power and 6.0 mm of defocus is $0.14\,\mathrm{J/cm^2}$, another set of parameters was tested that would result in the same fluence, which is 1.7 W and 8.0 mm. The only difference between these samples is the beam spot radius, which varies between 0.094 mm for D =6.0 mm and 0.125 mm for D =8.0 mm. As a consequence, the overlapping factor is higher for the second one. PL and PCD measurements are displayed in Figure 5.23.

The PL image of Figure 5.23 presents a more uniform distribution of intensity for the wafer prepared with $P = 1.0\,\mathrm{W} \wedge D = 6.0\,\mathrm{mm}$, even though it has some areas in between where the intensity drops drastically. The $P = 1.7\,\mathrm{W} \wedge D = 8.0\,\mathrm{mm}$ laser-treated wafer has a few high intensities regions on the left side of the wafer but it presents a more emphasized gradient from the top right of the wafer to the bottom left. Analysing the PCD measurements, the $\langle \mathrm{i}V_{\mathrm{oc}} \rangle$ of each dataset is: $(0.670 \pm 0.015)\,\mathrm{V}$ in red; $(0.660 \pm 0.014)\,\mathrm{V}$ in blue. These $\langle \mathrm{i}V_{\mathrm{oc}} \rangle$ values are the average of the nine measurements performed each wafer lasered in a 3×3 array, with the associated standard deviation of those measurements. A

variation of 10 mV is significant, so, from this experiment, the optimal set of parameters is $P = 1.0\,\mathrm{W} \wedge D = 6.0\,\mathrm{mm}$.

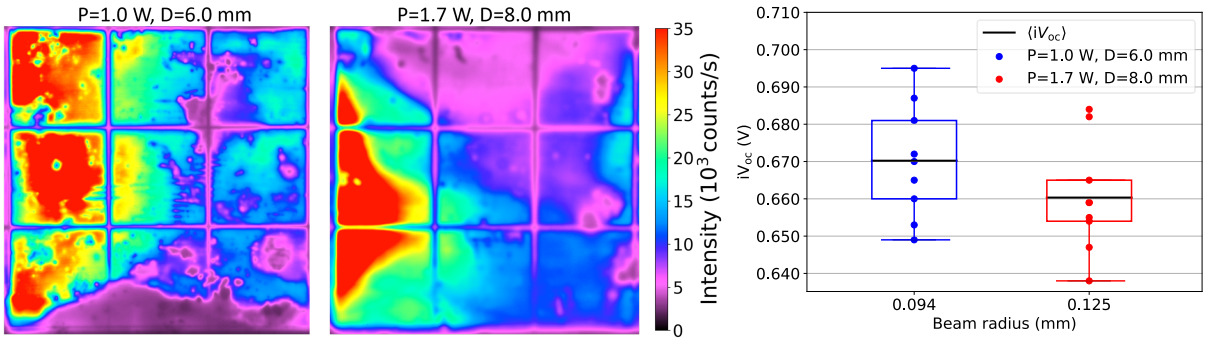

Figure 5.23: PL imaging and PCD measurements for two wafers processed with the same applied fluence ($F = 0.14\,\mathrm{J/cm^2}$) different laser parameter sets. The wafers were lasered using a 3×3 array with $P = 1.0\,\mathrm{W}$, $D = 6.0\,\mathrm{mm}$ for one wafer, and $P = 1.7\,\mathrm{W}$, $D = 8.0\,\mathrm{mm}$ for the other. The boxplot on the right displays a dataset for each parameter set, with nine PCD measurements performed across each wafer. All measurements were taken after hydrogenation.

To summarize the PCD data related to full wafers processed with a single set of laser parameters each, a boxplot was created for the iV_{oc} data as a function of fluence – Figure 5.24. Note that two sets contain only three measurements each: the non-lasered set (purple) and the $P = 2.0\,\mathrm{W} \wedge D = 6.0\,\mathrm{mm}$ set (grey). It is visible that the applied fluence range only goes up to $0.40\,\mathrm{J/cm^2}$. This limited interval arises mainly because higher values of defocus were tested to try to mitigate potential non-uniformities due to laser processing. Each dataset highlights two specific two data points (or one in the case of sets with only three measurements), represented by an unfilled circle with a border color corresponding to the respective set. This distinction indicates that the measurements correspond to positions P21 and P31 when visualizing the wafer as a 3×3 matrix array. These positions consistently give higher results. A closer examination of the plot reveals that the highest iV_{oc} in each dataset is found in one of these two places.

The three highest achieved iV_{oc} individual values were 0.695 V, 0.692 V and 0.688 V, belonging respectively to the parameter sets $P = 1.0\,\mathrm{W} \wedge D = 6.0\,\mathrm{mm}$, the non-lasered sample and $P = 2.0\,\mathrm{W} \wedge D = 6.0\,\mathrm{mm}$ of Figure 5.24. Notably, all these measurements were taken on the bottom left section of the wafers (P21 or P31). Additionally, the highest $\langle iV_{oc} \rangle$ value belongs to the set of the non-lasered sample. This, combined with the interquartile ranges of each set, seems to indicate that the non-lasered sample is the most favorable option based on the available data. However, it is important to remember that this dataset includes fewer measurements than most sets.

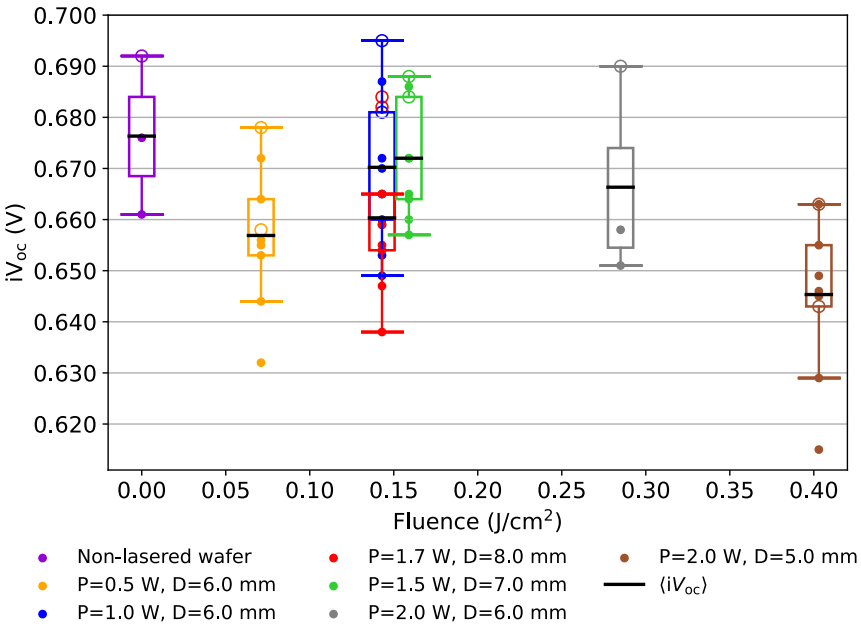

Figure 5.24: PCD measurements of wafers lasered in 3×3 arrays with several single sets of parameters (enumerated on the legend of the plot). The data is presented as a box plot, where all sets contain nine measurements except for the purple and grey datasets, which each have three measurements. Point distance was kept constant at $L = 35\,\mu$m. Measurements were taken after hydrogenation with firing at $T_{\text{peak}} = 750\,^{\circ}$C.

It was already understood that the lasering alone does not necessarily enhance the passivation quality or the performance of the future solar cell in the absence of any hydrogenation process, which is expected as there are several recombination mechanisms present in the absence of this procedure. Now, provided the hydrogenation process, overall, there appear to be no significant improvements from laser-processing the wafers comparing non-lasered. However, similar passivation results can be obtained with the laser treatments.

5.4 Crystallinity Study

This section focuses on analyzing the crystallinity of the a-Si layer after laser-induced crystallization. Studying crystallinity provides insights into the microstructure of the sample, which will be assessed through XRD measurements.

Using XRD, diffraction patterns were obtained for three samples: a non-lasered wafer, a wafer lasered with $P = 0.5\,\text{W} \wedge D = 2.8\,\text{mm}$ ($F = 0.28\,\text{J/cm}^2$) and wafer lasered with $P = 2.3\,\text{W} \wedge D = 4.0\,\text{mm}$ ($F = 0.70\,\text{J/cm}^2$), both with a fixed $L = 40\,\mu$m, presented in Figure 5.25. These XRD measurements were conducted without the wafers passing through any hydrogenation process, meaning that the only annealing process involved capable of melting and recrystallizing the layer is the LIC process.

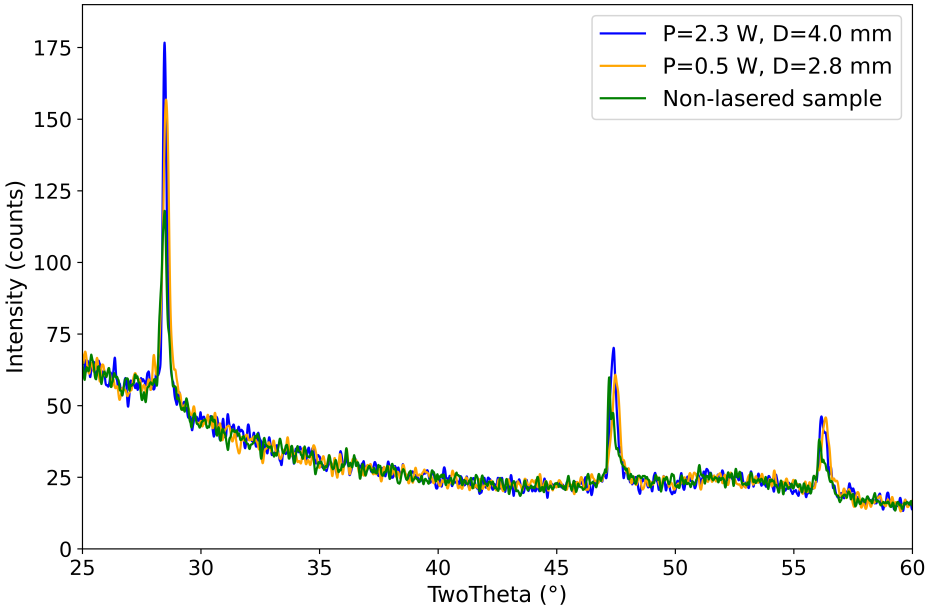

Figure 5.25: XRD patterns of a non-lasered wafer and laser-treated samples with $P = 0.5\,\mathrm{W}$, $D = 2.8\,\mathrm{mm}$ $\left(F = 0.28\,\mathrm{J/cm^2}\right)$ and $P = 2.3\,\mathrm{W}$, $D = 4.0\,\mathrm{mm}$ $\left(F = 0.70\,\mathrm{J/cm^2}\right)$. Point distance was kept constant at $L = 40\,\mu\mathrm{m}$. Measurements performed prior to hydrogenation.

The main characteristic diffraction Si peaks are visible in all profiles of Figure 5.25, for the angles approximated to 28.5°, 47.5°, and 56.5°, corresponding respectively to the lattice orientations (111), (220) and (311) [50]. For the first peak, which usually exhibits the highest intensity, the non-lasered sample shows a lower peak intensity compared to the $P = 0.5\,\mathrm{W} \wedge D = 2.8\,\mathrm{mm}$ peak, which, in turn, is lower than the $P = 2.3\,\mathrm{W} \wedge D = 4.0\,\mathrm{mm}$ peak. For the second peak, the $P = 2.3\,\mathrm{W} \wedge D = 4.0\,\mathrm{mm}$ sample again exhibits the highest intensity, while distinguishing between the other two profiles is more difficult. Every sample seems to have approximately the same intensity for the last identified peak. Higher intensity indicates an increased number of counts registered, which implies more diffraction events, suggesting larger crystal sizes or a greater quantity of crystals. From the data available, it can be considered that, compared to the non-lasered sample, the crystallinity increased with the laser treatment. More specifically, the crystallinity improved with the increasing of the applied fluence, even though the precise degree of amorphousness in the a-Si (non-lasered) sample is unknown.

The crystallite size was determined by the software through Scherrer evaluation, as described by Equation (4.13). Table 5.1 presents the crystallite sizes for the first peak, corresponding to the lattice orientation (111) of the profiles displayed in Figure 5.25. These results provide evidence that the lasering process enhances the crystallinity of a-Si. Specific reference values for the crystallite sizes of a-Si or poly-Si measured via XRD were not found in the literature. Besides that, comparing the results with another technique, such as Raman spectroscopy or transmission electron microscopy, which rely on a different physical principle, is rather complex [52]. This observed increase in crystallite size indicates that the crystallinity is improved by increasing the applied fluence on the wafers, even though the degree of crystallinity is difficult to quantify with the available data.

Table 5.1: Crystallite size calculated by the XRD instrument software based on the first diffraction peak for each analyzed sample. Lasered samples had the point distance constant at $L = 40\,\mu$m. Measurements were performed prior to hydrogenation.

Sample	Fluence $\left(\mathrm{J/cm^2}\right)$	Peak angle (°)	Crystallite size (nm)
Non-lasered	0	28.50	22.2
$P = 0.5\,\mathrm{W}$, $D = 2.8\,\mathrm{mm}$	0.28	28.51	25.3
$P = 2.3\,\mathrm{W}$, $D = 4.0\,\mathrm{mm}$	0.70	28.48	38.2

5.5 Conductivity Study

In this section, the conductivity of the layer after laser-induced crystallization of a-Si is analyzed. This is assessed by the Four-Point-Probe, which indirectly measures sheet resistance, by applying a constant current and measuring the voltage difference through the probes. Since sheet resistance is related to resistivity by Equation (4.14), it serves as an indicator of the layer's conductivity, reflecting how charge carriers move through the crystal structure.

As a reference, a measurement was conducted on a non-lasered wafer, presented as an R_{sh} colormap distribution, in Figure 5.26. The left image presents the wafer in its as-deposited state, while the one on the right is the wafer after a series of processes: a $\mathrm{SiN_x}$ deposition followed by a fast firing step $T_{\mathrm{peak}} = 875\,^{\circ}\mathrm{C}$ and a $\mathrm{SiN_x}$ removal step. This last step is essential as $\mathrm{SiN_x}$ is an insulating material, which prevents the current injected by the FPP device from flowing between the probes, making the measurement impossible.

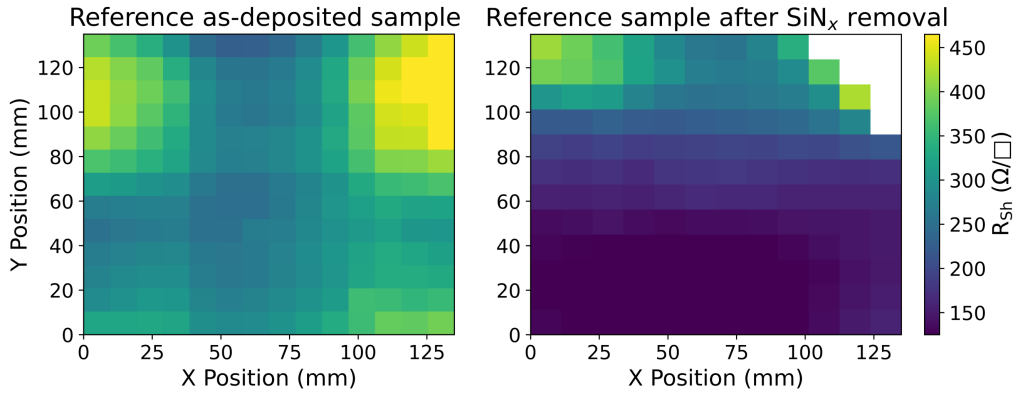

Figure 5.26: FPP measurements conducted on non-lasered wafers presented as R_{sh} colormap distribution. On the left side, the measurement was taken in the wafer as-deposited. On the right side, a different wafer went through a hydrogenation process with $T_{\mathrm{peak}} = 875\,^{\circ}\mathrm{C}$, followed by a $\mathrm{SiN_x}$ layer removal step. Average R_{sh} values are: $\langle R_{\mathrm{sh}} \rangle = (323 \pm 63)\ \Omega/\square$, for the wafer on the left; $\langle R_{\mathrm{sh}} \rangle = (189 \pm 78)\ \Omega/\square$, for the wafer on the right.

Comparing the colormaps, the sample that had the fast firing step exhibits a more uniform distribution of values, still presenting a region with higher R_{sh} near the top corners, as in the as-deposited wafer. The $\langle R_{\mathrm{sh}} \rangle$ value decreased from $(323 \pm 63)\ \Omega/\square$ to $(189 \pm 78)\ \Omega/\square$. This decrease is due to the fast firing step, as it is the only annealing process performed. Unfortunately, a reference measurement for a wafer fired at $T_{\mathrm{peak}} = 750\,^{\circ}\mathrm{C}$, the firing temperature selected as optimal in Section 5.3.2, is unavailable. So, quantitative conclusions are limited as there is a significant temperature gap of $125\,^{\circ}\mathrm{C}$ between the peak firing temperatures. Even so, it can be affirmed that conductivity improved, as the R_{sh} decreased, and that the uniformity across the wafer got better.

From the same samples analyzed for PL in Figure 5.21, FPP measurements were conducted and presented in Figure 5.27. The 3×3 array used the following interval of laser parameters: $P = [1.0, 3.0]\,\mathrm{W}$,

$D = [6.0, 8.0]$ mm, with a fixed $L = 35\,\mu$m, inverting the interval for the other wafer. When comparing both orientations, no major or immediate pattern is observed. However, by closely examining and comparing the regions of highest and lowest applied fluence on the map – $F_{\max} = 0.43\,\mathrm{J/cm^2}$ for $P = 3.0$ W and $D = 6.0$ mm; $F_{\min} = 0.08\,\mathrm{J/cm^2}$ for $P = 1.0$ W and $D = 8.0$ mm – a difference in color shade is visible. The regions with higher fluence exhibit a relatively darker tone on both samples. Looking at the scale, the darker shade corresponds to lower R_{sh} values, which indicates an improvement relative to the reference as-deposited sample. Additionally, comparing the colormap values of Figure 5.27 with the as-deposited sample of Figure 5.26, a slight decrease in R_{sh} values is observed in the laser-treated wafers.

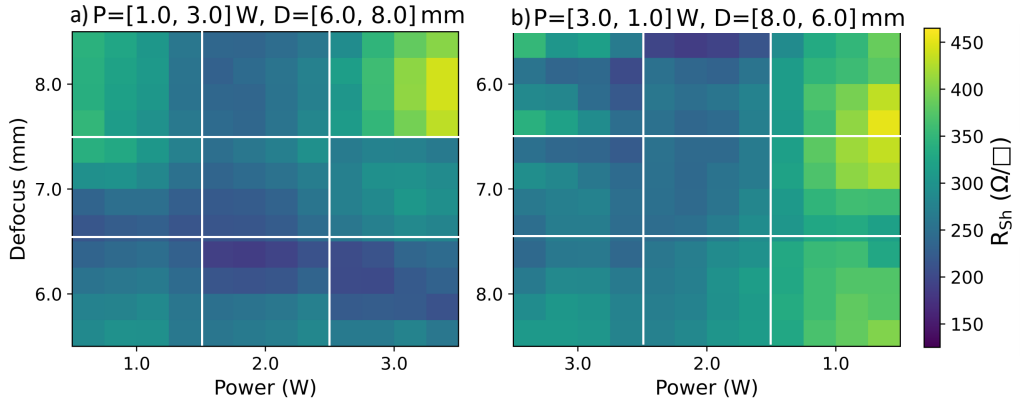

Figure 5.27: FPP measurements of laser-processed 3×3 array samples. The set parameters were the following: $P = [1.0, 3.0]$ W and fixed $L = 35\,\mu$m for both samples, $D = [6.0, 8.0]$ mm for a), and $D = [8.0, 6.0]$ mm for b) (same range, reverse direction). For this treatment, fluence ranged between $F = [0.08, 0.43]\,\mathrm{J/cm^2}$ and the beam radius between $\omega = [0.094, 0.125]$ mm. Measurements were performed before the hydrogenation process.

APCV-deposited a-Si, with its disordered structure, may contain amorphous agglomerates. It can be speculated that, even if the energy of the laser pulse is insufficient to fully melt and recrystallize these agglomerates, the thermal budget from lasering could facilitate nucleation. This process may increase the grain size, which is in accordance with XRD measurements, and lead to fewer grain boundaries. Consequently, this would lead to fewer disruptions of the layer structure, improving carrier transport, which could be the possible explanation of the decrease in the measured R_{sh} after lasering. Alternatively, dopant activation of substitutional impurities of a-Si, induced by the laser step, may also contribute to improved conductivity, without necessarily meaning grain size increase of the crystallites.

Each FPP measurement provides a value of R_{sh} that constitutes the colormap, and it also provides a value of the associated uncertainty. The uncertainties of FPP measurements of the two previous wafers presented in Figure 5.27 are displayed in Figure 5.28. While the uncertainty colormaps appear significantly inhomogeneous, the scale reveals that the range is relatively small. The uncertainties vary between $0\,\Omega/\square$ and $5\,\Omega/\square$, with a good majority of measurements falling below $3\,\Omega/\square$. This demonstrates the reliable performance of the equipment, as it measures R_{sh} values that are up to 100 times greater than the corresponding uncertainties. Furthermore, considering the standard deviation of the $\langle R_{\mathrm{sh}} \rangle$ value resulted from the FPP map of the reference as-deposited sample – $\langle R_{\mathrm{sh}} \rangle = (323 \pm 63)\,\Omega/\square$ – the uncertainty of the FPP measurement is relatively low in comparison to this value. This suggests that the variations observed in the colormap are more likely to be attributed to the inhomogeneous distribution of the a-Si layer.

5. EXPERIMENTAL RESULTS AND DISCUSSION

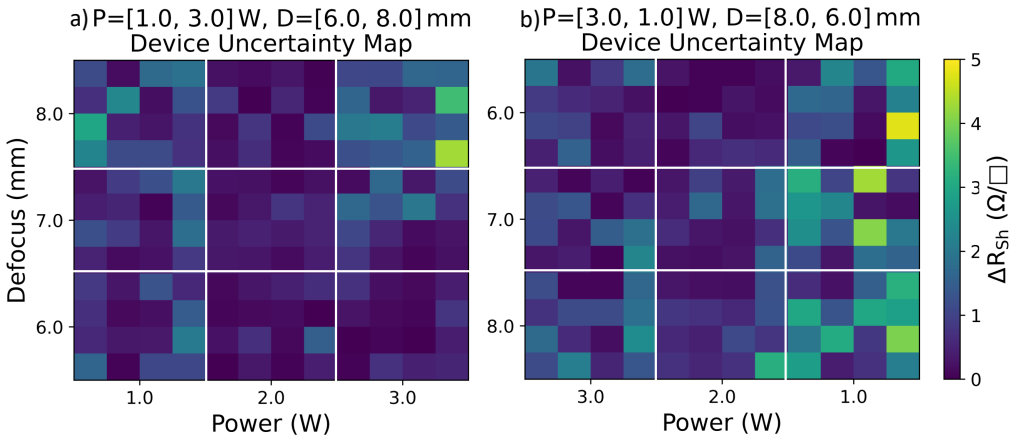

Figure 5.28: FPP device uncertainty colormap distribution of the samples presented in Figure 5.27, where ΔR_{sh} represents the individual measurement uncertainty provided by the instrument. The set parameters used were the following: $P = [1.0, 3.0]$ W for both samples, $D = [6.0, 8.0]$ mm for the left side, and $D = [8.0, 6.0]$ mm for the right side (same range, reverse direction). For this treatment, the fluence ranged between $F = [0.08, 0.43]$ J/cm^2 and the beam radius between $\omega = [0.094, 0.125]$ mm. Measurements were performed before the hydrogenation process.

The FPP measurements for wafers lasered with a single set of parameters are displayed in Figure 5.29 by the colormap distributions of the wafers, with all being referenced to the same color scale. It is visible that each colormap has a large range of R_{sh} values even though each wafer was treated with a single parameter set. They all present a similar section on the top right corner exhibiting higher R_{sh} than the rest of the wafer. This behavior is suggested to be characteristic of the a-Si layer itself, as it is present in several samples, including the reference as-deposited sample in Figure 5.26. Notably, sample (e), corresponding to parameters $P = 2.0$ W and $D = 5.0$ mm, presents the colormap with the lowest R_{sh} achieved within these five samples.

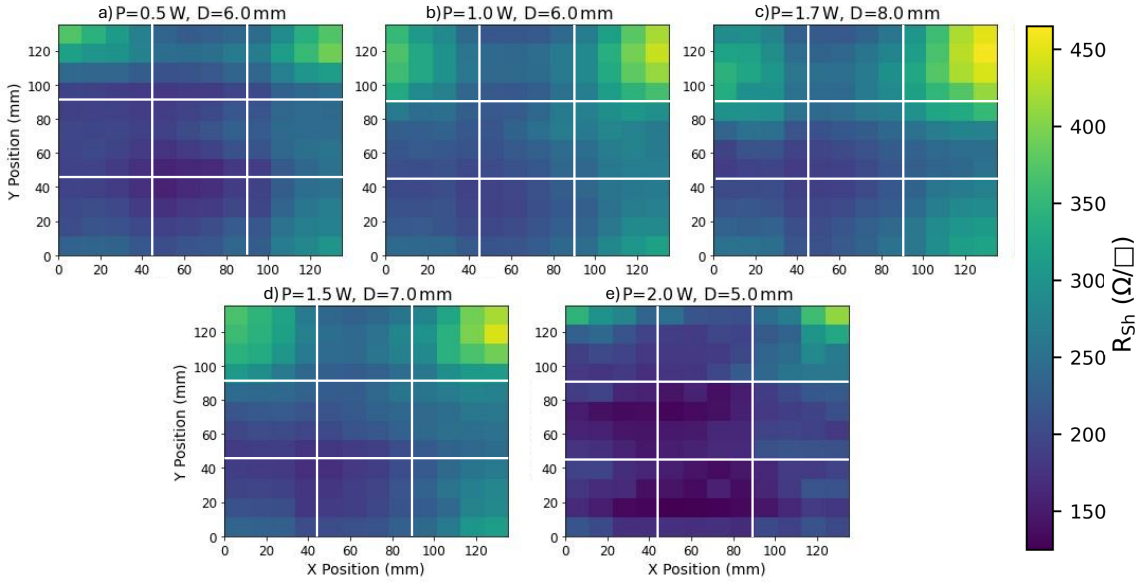

Figure 5.29: Colormap distributions of FPP measurements for wafers lasered in 3×3 arrays, each with a single set of parameters. Point distance was kept constant at $L = 35\,\mu$m. Measurements were performed after hydrogenation ($T_{peak} = 750\,^{\circ}$C) and SiN_x removal. Fluence and beam radius for each sample: a) $F = 0.07$ J/cm^2, $\omega = 0.094$ mm; b) $F = 0.14$ J/cm^2, $\omega = 0.094$ mm; c) $F = 0.14$ J/cm^2, $\omega = 0.125$ mm; d) $F = 0.16$ J/cm^2, $\omega = 0.110$ mm; e) $F = 0.40$ J/cm^2, $\omega = 0.080$ mm. All colormaps share the same R_{sh} scale.

To further analyze the last FPP measurements, Figure 5.30 summarizes the results by plotting the

$\langle R_{sh} \rangle$ values as a function of the applied laser fluence. The highest $\langle R_{sh} \rangle$ corresponds to the non-lasered sample, while the lowest $\langle R_{sh} \rangle$ is observed in the sample with the highest applied fluence ($P = 2.0\,\mathrm{W}$, $D = 5.0\,\mathrm{mm}$). In these samples, two annealing processes are at play: LIC and the fast firing step for hydrogenation, the latter being identical across all samples. The plot does not show a clear trend that would enable conclusive statements. Theoretically, higher fluences should enhance conductivity, as they provide more energy to the layer, increasing crystallization and improving carrier transport. This interpretation aligns with the fact that the lowest R_{sh} is achieved with the parameter set of highest fluence. However, a small discrepancy is observed with the set $P = 0.5\,\mathrm{W}$ and $D = 6.0\,\mathrm{mm}$, that has a lower R_{sh} than some sets with higher fluences. It can be argued that this phenomenon could be attributed to inhomogeneous layer distribution across the wafers, a factor that has already been noted to affect passivation quality.

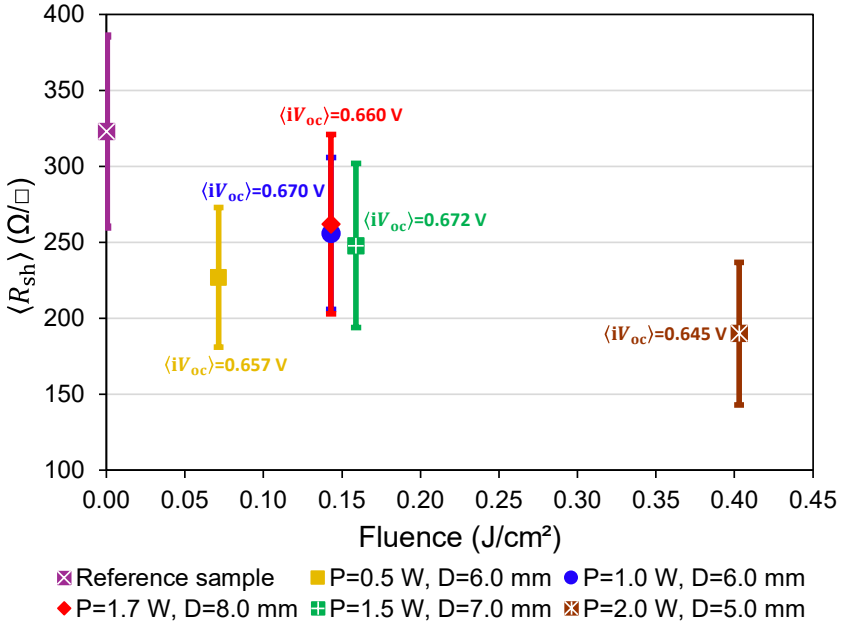

Figure 5.30: $\langle R_{sh} \rangle$ plot as a function of applied fluence for wafers lasered in 3×3 arrays, using a single set of parameters per wafer. Point distance was kept constant at $L = 35\,\mu\mathrm{m}$. Fluence ranged from $F = [0, 0.40]\,\mathrm{J/cm^2}$, while the beam radius varied between $\omega = [0.079, 0.125]$ mm. Measurements were performed after hydrogenation ($T_{peak} = 750\,^{\circ}\mathrm{C}$) and SiN_x removal, except for the as-deposited sample, which did not undergo hydrogenation. The $\langle iV_{oc} \rangle$ values from PCD measurements performed on the same wafers are presented with the corresponding color of each data set (Figure 5.24), except for the as-deposited wafer, as no hydrogenated non-lasered wafer fired at $750\,^{\circ}\mathrm{C}$ was processed.

Due to the absence of a reference sample that underwent the fast firing step at $T_{peak} = 750\,^{\circ}\mathrm{C}$, it is difficult to quantify the improvement in sheet resistance specifically attributed to LIC, as all the single set lasered wafers had a SiN_x coating and did the fast firing step. Nevertheless, the available data suggests that LIC enhances the conductivity of the a-Si layer. This implies that the values of fluences applied seem to be sufficient to induce the transformation of Si in the amorphous phase to the polycrystalline phase, achieving a certain degree of crystallinity that cannot be quantified with only the available data.

Chapter 6

Conclusions

The goal of this work was the development of a suitable laser-induced crystallization process of (n) a-Si:P in silicon solar cells, specifically for application on poly-Si/SiO_x passivating contacts. Measurements focused on passivation quality, element composition, surface topography, crystallinity, and conductivity of the resulting (n) poly-Si(P) layer.

The study evaluated and compared the performance of two nanosecond pulsed laser sources with distinct wavelengths of $\lambda = 532\,\text{nm}$ (green laser) and $\lambda = 355\,\text{nm}$ (UV laser). PL images presented a uniform intensity distribution across several samples, indicating no significant gradient in passivation quality, despite the wide range of laser parameters tested. Surface ablation was confirmed under optical microscope, revealing laser pulses that had melted the surface. GDOES measurement profiles showed the absence of a peak on the oxygen signal, indicating no interface oxide between the a-Si and absorber layer, resulting in a lack of interface passivation. In comparison, samples processed with the UV laser using the same laser parameters presented no macroscopic contrast between lasered and non-lasered areas. Microscopically, no ablation is observed, and the samples appeared to have a topography similar to that of an as-deposited a-Si wafer. GDOES profiles matched the pattern of as-deposited a-Si wafers, confirming that there was no unwanted ablation.

The absorption coefficient of a-Si differs significantly between 532 nm and 355 nm, with the latter being approximately 100 times higher. As a result, the green laser penetrates deeper into the wafer, as the radiation is less absorbed in the a-Si layer compared with the UV laser. Therefore, the UV laser provides better control over the laser processing of a-Si and it was selected as the laser source for the remainder of the project.

With further laser treatments, a macroscopic surface color contrast appeared in several samples for the fields where the set laser parameters would correspond to higher fluences. However, within a lasered field defined by P, D and L values, only part of the cell presented this contrast. Microscope analysis revealed a gradient of increasingly melted laser spots from the bottom to the top, and especially from the left to the right. GDOES measurements confirmed that different fluences were applied at various positions within a lasered field, as the oxygen and phosphorus profiles would vary within the lasered field position. This would occur regardless of the field size, even though the set parameters remained unchanged throughout the field. These experiments suggested a potential issue regarding the galvanometer scanner. Up to this point, the galvanometer alone managed the scanning of the fields, with the table beneath the wafer fixed. It can be speculated that the sharp redirection angles of the beam inside the scanning unit machinery could influence beam intensity, resulting in an uncontrolled increase in the applied fluence. To address this problem, a change was made in the software configuration: the XY table alignment scanner was activated to reposition in a more central position, avoiding sharp incident angles

from the galvanometer with the wafer. In this configuration, the galvanometer was used exclusively for scanning the beam within a lasered field. Microscope images and GDOES measurements became more consistent across the lasered fields, suggesting that this adjustment could mitigate the problem and represent the optimal available choice to achieve more uniform laser treatments.

Using the laser source unit and scanning technique arrangement in optimal conditions mentioned before, diverse arrays of laser parameters were processed on wafers, comparing them regarding the resulting applied fluence or laser beam radius. After laser treatments, these wafers underwent a hydrogenation process, which included the deposition of a 75 nm thick SiN_x, followed by a fast firing step at a standard peak temperature of 875 °C. A wide diversity of results was observed in the iV_{oc} values from the PCD measurements, for a fluence ranging between $F = [0, 0.6]\,\mathrm{J/cm^2}$. These results showed measurements with similar fluences producing distinct iV_{oc} values, which may have been influenced by differences in laser parameter settings or possibly by inhomogeneities in the a-Si deposition, as variations in layer thickness across the wafer would affect a-Si crystallization during laser processing. Additionally, the results also suggested that higher fluences were ineffective for passivation purposes.

To optimize the firing temperature to hydrogenate laser-processed wafers, multiple wafers were treated using the same laser parameter arrays and then fired at temperatures ranging from 700 °C and 900 °C. PL and PCD measurements indicated that the optimal temperature for achieving better passivation quality was 750 °C, which was subsequently used for the remainder of the project.

Experiments investigating different orientations and positioning of the laser parameters in the wafer indicated that distinct wafer regions lasered with equal laser parameters resulted in variations in passivation performance. This highlighted the need to account for layer inhomogeneity to improve the reliability of the wafer characterization. To address this, wafers were processed using a single parameter set, with comparisons made from wafer to wafer rather than across different regions of the same wafer. Among the tested laser parameter sets, the optimal set was $P = 1.5\,\mathrm{W}$, $D = 7.0\,\mathrm{mm}$ and $L = 35\,\mu\mathrm{m}$, resulting in a fluence of $F = 0.16\,\mathrm{J/cm^2}$. After hydrogenation at $T_{peak} = 750\,^{\circ}\mathrm{C}$, for the non-lasered wafer, the $\langle \mathrm{i}V_{oc} \rangle$ was $(0.677 \pm 0.015)\,\mathrm{V}$, while for the optimal laser set, it was $(0.672 \pm 0.012)\,\mathrm{V}$, with no severe laser damage introduced. The next best parameter set, $P = 1.0\,\mathrm{W}$, $D = 6.0\,\mathrm{mm}$, and $L = 35\,\mu\mathrm{m}$, with a fluence of $F = 0.14\,\mathrm{J/cm^2}$, resulted in $\langle \mathrm{i}V_{oc} \rangle = (0.670 \pm 0.015)\,\mathrm{V}$. However, individual PCD measurements in this wafer registered the highest iV_{oc} achieved for LIC in this project, reaching 0.695 V, showing the potential of this method.

XRD measurements indicated that LIC improved the crystallinity of a-Si with increasing applied fluence, with no hydrogenation process involved, meaning that the only annealing process involved is LIC. The melting of the amorphous Si phase leads to the formation of polycrystalline Si, although the degree of crystallinity remains difficult to quantify with the available data. These XRD results suggest that LIC enhances crystallinity.

Through FPP measurements, it was observed that increasing the fluence leads to lower sheet resistance, indicating improved layer conductivity and, consequently, better carrier transport. Similarly, regarding the previously discussed iV_{oc} values, sheet resistance significantly decreased in wafers processed with laser treatments followed by the firing step (for hydrogenation), compared to a reference as-deposited wafer. However, a balance is necessary between achieving high conductivity and optimizing passivation quality. While higher fluences improve conductivity, they do not necessarily lead to the best iV_{oc} results previously presented, making it essential to find a trade-off between these two factors.

This investigation further corroborates that LIC enhances the crystallinity and conductivity of (n) poly-Si compared to the non-lasered wafers with an as-deposited (n) a-Si layer. Incorporating a hydrogenation process – depositing a hydrogen-rich layer and performing a fast firing step, a common

practice in PV – can further improve conductivity and crystallinity. Additionally, it achieves iV_{oc} values comparable to those of a non-lasered sample from the same batch, both after undergoing hydrogenation. This was accomplished without significant surface ablation, as observed under the optical microscope, and without compromising the (n) poly-Si layer structure or the SiO_x interface, confirmed by GDOES measurements.

Future work should focus on further increasing the iV_{oc} for laser-treated areas by conducting a more detailed investigation of laser parameters, in relation to applied fluence and laser beam size. Additional wafers should be processed with constant power and defocus, varying only the pulse point distance to further analyze how the pulse overlap impacts LIC, without altering the applied fluence or beam size. Investigating the control of the laser radiation depth absorbance would be important to determine the maximum penetration depth of the radiation and what ranges of temperatures would it result in. This analysis would be supported by incorporating simulations. By building a finite element model, thermal simulations could be conducted to replicate LIC on a-Si with the sample structures utilized in this project, as has been done in other studies [56]. To have an accurate modeling, several physical properties would need to be precisely known, like the thickness, applied fluence and beam radius, for instance.

With such a simulation, it would be possible to test several laser parameter sets and estimate the resulting temperature profiles during laser scanning. This approach would allow to determine what temperature a lasered field would reach under specific power and defocus settings, enabling a better understanding of whether the melting temperature of silicon would be achieved. This would give greater control over the parameters without the need to use physical samples during the initial experimental phase, leading to reduced material waste and possible budget savings.

Bibliography

[1] Our World in Data. *Solar panel prices have fallen by around 20% every time global capacity doubled*. H. Ritchie. Accessed: 18-02-2025. 2024. URL: https://ourworldindata.org/data-insights/solar-panel-prices-have-fallen-by-around-20-every-time-global-capacity-doubled.

[2] Reuters. *EU solar growth slows, raising fears for energy transition*. K. Abnett. Acessed: 10-01-2025. 2024. URL: https://www.reuters.com/business/energy/eu-solar-growth-slows-raising-fears-energy-transition-2024-12-17/.

[3] JinkoSolar. *JinkoSolar's High-efficiency N-Type Monocrystalline Silicon Solar Cell Sets Our New Record with Maximum Conversion Efficiency of 26.1%*. Accessed: 20-02-2025. 2022. URL: https://ir.jinkosolar.com/news-releases/news-release-details/jinkosolars-high-efficiency-n-type-monocrystalline-silicon-1.

[4] Solar Magazine. *TOPCon Solar Cells: The New PV Module Technology in the Solar Industry*. Accessed: 18-02-2025. 2023. URL: https://solarmagazine.com/solar-panels/topcon-solar-cells/?.

[5] S. Mitra et al. "Understanding Hydrogen Passivation Mechanism in poly-Si Passivating Contacts: Insights from Effusion Studies". In: *30th Annual NREL Silicon Workshop* (). URL: https://www.nrel.gov/docs/fy23osti/87261.pdf.

[6] P. Würfel and U. Würfel. *Physics of Solar Cells: From Basic Principles to Advanced Concepts*. 3rd. Wiley, 2016. ISBN: 978-3-527-41309-6.

[7] R. Peibst et al. "Working principle of carrier selective poly-Si/c-Si junctions: Is tunnelling the whole story?" In: *Solar Energy Materials and Solar Cells* 158 (2016), pp. 60–67. DOI: https://doi.org/10.1016/j.solmat.2016.05.045.

[8] A. Luque and S. Hegedus. *Handbook of Photovoltaic Science and Engineering*. 2nd. Wiley, 2011. ISBN: 978-0-470-72169-8.

[9] A. B. Sproul, M. A. Green, and J. Zhao. "Improved value for the silicon intrinsic carrier concentration at 300 K". In: *Journal of Applied Physics* 57 (1990), pp. 255–257. DOI: https://doi.org/10.1063/1.103707.

[10] National Renewable Energy Laboratory (NREL). *Reference Solar Spectral Irradiance: Air Mass 1.5*. Accessed: 2024-12-04. URL: https://www.nrel.gov/grid/solar-resource/spectra-am1.5.html.

[11] W. Fuhs, K. Niemann, and J. Stuke. "Heterojunctions of Amorphous Silicon and Silicon Single Crystals". In: *AIP Conference Proceedings* 20 (1 1974), pp. 345–350. DOI: https://doi.org/10.1063/1.2945985.

[12] J. Robertson. “Deposition mechanism of hydrogenated amorphous silicon”. In: *Journal of Applied Physics* 87.5 (2000), pp. 2608–2617. DOI: 10.1063/1.372226.

[13] G. Wilkes et al. “Laser Crystallization and Dopant Activation of a-Si:H Carrier-Selective Layer in TOPCon Si Solar Cells”. In: *IEEE Journal of Photovoltaics* 10.5 (2020), pp. 1283–1289. DOI: 10.1109/JPHOTOV.2020.3006273.

[14] N. Hernandez-Como and A. Morales-Acevedo. “Hetero-junction (HIT) silicon solar cell model for AMPS-1D simulation”. In: (2008), pp. 449–454. DOI: 10.1109/ICEEE.2008.4723401.

[15] M. Rüdiger et al. “Parameterization of Free Carrier Absorption in Highly Doped Silicon for Solar Cells”. In: *IEEE Transactions on Electron Devices* 60.7 (2013), pp. 2156–2163. DOI: 10.1109/TED.2013.2262526.

[16] W. Shockley and W. T. Read. “Statistics of the Recombinations of Holes and Electrons”. In: *Physical Review Journals* 87 (5 1952), pp. 835–842. DOI: 10.1103/PhysRev.87.835.

[17] R. N. Hall. “Electron-Hole Recombination in Germanium”. In: *Physical Review Journals* 87 (2 1952), pp. 387–387. DOI: 10.1103/PhysRev.87.387.

[18] A. G. Aberle. “Surface passivation of crystalline silicon solar cells: a review”. In: *Progress in Photovoltaics: Research and Applications* 8.5 (2000), pp. 473–487. DOI: https://doi.org/10.1002/1099-159X(200009/10)8:5<473::AID-PIP337>3.0.CO;2-D.

[19] J. F. Lelièvre et al. “Study of the composition of hydrogenated silicon nitride SiN_x:H for efficient surface and bulk passivation of silicon”. In: *Solar Energy Materials and Solar Cells* 93.8 (2009), pp. 1281–1289. DOI: https://doi.org/10.1016/j.solmat.2009.01.023.

[20] J. Melskens et al. “Passivating Contacts for Crystalline Silicon Solar Cells: From Concepts and Materials to Prospects”. In: *IEEE Journal of Photovoltaics* 8.2 (2018), pp. 373–388. DOI: 10.1109/JPHOTOV.2018.2797106.

[21] National Renewable Energy Laboratory (NREL). *Best Research-Cell Efficiency Chart*. Accessed: 04-01-2025. URL: https://www.nrel.gov/pv/cell-efficiency.html.

[22] W. Shockley and H. J. Queisser. “Detailed Balance Limit of Efficiency of p-n Junction Solar Cells”. In: *Journal of Applied Physics* (1961), pp. 510–519. DOI: https://doi.org/10.1063/1.1736034.

[23] S. Rühle. “Tabulated values of the Shockley–Queisser limit for single junction solar cells”. In: *Solar Energy* 130 (2016), pp. 139–147. DOI: https://doi.org/10.1016/j.solener.2016.02.015.

[24] T. G. Allen et al. “Passivating contacts for crystalline silicon solar cells”. In: *Nature Energy* 4 (2019), pp. 914–928. DOI: https://doi.org/10.1038/s41560-019-0463-6.

[25] M. Hermle et al. “Passivating contacts and tandem concepts: Approaches for the highest silicon-based solar cell efficiencies”. In: *Applied Physics Reviews* 7.2 (2020), p. 021305. DOI: 10.1063/1.5139202.

[26] J. Benick et al. “High efficiency n-type Si solar cells on Al_2O_3-passivated boron emitters.” In: *Applied Physics Letters* 92.25 (2008), p. 253504. DOI: 10.1063/1.2945287.

[27] E. Yablonovitch et al. “A 720 mV open circuit voltage SiO_x:c-Si:SiO_x double heterostructure solar cell”. In: *Applied Physics Letters* 47.11 (1985), pp. 1211–1213. DOI: 10.1063/1.96331.

[28] F. Feldmann et al. “Studying dopant diffusion from Poly-Si passivating contacts”. In: *Solar Energy Materials and Solar Cells* 200 (2019), p. 109978. DOI: https://doi.org/10.1016/j.solmat.2019.109978.

[29] U. Römer et al. “Recombination behavior and contact resistance of n^+ and p^+ poly-crystalline Si/mono-crystalline Si junctions”. In: *Solar Energy Materials and Solar Cells* 131 (2014), pp. 85–91. DOI: https://doi.org/10.1016/j.solmat.2014.06.003.

[30] B. Terheiden et al. “Manufacturing 100-µm-thick silicon solar cells with efficiencies greater than 20% in a pilot production line”. In: *Physica Status Solidi A* 212.1 (2015), pp. 13–24. DOI: https://doi.org/10.1002/pssa.201431241.

[31] A Gawlik et al. “Diode Laser-Crystallization for the Formation of Passivating Contacts for Solar Cells”. In: *physica status solidi (RRL) – Rapid Research Letters* 16.5 (2022), p. 2100537. DOI: https://doi.org/10.1002/pssr.202100537.

[32] R. Peibst et al. “Atmospheric Pressure Chemical Vapor Deposition of In-Situ Doped Amorphous Silicon Layers for Passivating Contacts”. In: (2018). DOI: 10.4229/35thEUPVSEC20182018-2DV.3.49.

[33] M. Lehmann et al. “Analysis of hydrogen distribution and migration in fired passivating contacts (FPC)”. In: *Solar Energy Materials and Solar Cells* 200 (2019), p. 110018. DOI: https://doi.org/10.1016/j.solmat.2019.110018.

[34] T. H. DiStefano and D. E. Eastman. “The band edge of amorphous SiO_2 by photoinjection and photoconductivity measurements”. In: *Solid State Communications* 9.24 (1971), pp. 2259–2261. DOI: https://doi.org/10.1016/0038-1098(71)90643-0.

[35] I.W. Boyd and J.I.B. Wilson. “Laser annealing for semiconductor devices”. In: *AIP Conference Proceedings* 287 (1980), p. 278. DOI: https://doi.org/10.1038/287278a0.

[36] S. Chowdhury et al. “Crystallization of Amorphous Silicon via Excimer Laser Annealing and Evaluation of Its Passivation Properties”. In: *Energies* 13.13 (2020). DOI: 10.3390/en13133335.

[37] M. M. Heyns et al. “Cost-effective cleaning for advanced Si-processing”. In: *IEEE Xplore* (1999), pp. 325–328. DOI: 10.1109/IEDM.1998.746365.

[38] X.M. Yang et al. “Silicon wafer wettability and aging behaviors: Impact on gold thin-film morphology”. In: *Materials Science in Semiconductor Processing* 26 (2014), pp. 25–32. DOI: https://doi.org/10.1016/j.mssp.2014.03.044.

[39] T. Okker et al. “Charge carrier transport mechanism through different oxides for (n) poly-Si/SiO_x fired passivating contacts”. In: *Physica Status Solidi (RRL) - Rapid Research Letters* 18.9 (2024). ISSN: 1862-6254. DOI: 10.1002/pssr.202400099.

[40] *microSTRUCT C*. 3D-Micromac AG, 2016.

[41] University of Konstanz. Internal Communication.

[42] D. Kiliani. “Aufbau eines lumineszenz-messplatzes zur charakterisierung von solarzellen”. MA thesis. 2009.

[43] B. Gapp. “Characterization of APCVD Based Processes for Deposition of Al_2O_3 Layers for PERC Solar Cells”. MA thesis. University of Konstanz, 2018.

[44] *WCT-120 Photoconductance Lifetime Tester User Manual*. Sinton Instruments.

[45] R. A. Sinton and A. Cuevas. "Contactless determination of current–voltage characteristics and minority carrier lifetimes in semiconductors from quasi-steady-state photoconductance data". In: *Applied Physics Letters* 69.17 (1996), pp. 2510–2512. DOI: 10.1063/1.117723.

[46] H. Nagel, C. Berge, and A.G. Aberle. "Generalized analysis of quasi-steady-state and quasi-transient measurements of carrier lifetimes in semiconductors". In: *Journal of Applied Physics* 86.11 (1999), pp. 6218–6221. DOI: 10.1063/1.371633.

[47] *Betriebsanleitung - GDA 750 HR*. SPECTRUMA Analytik GmbH, 2016.

[48] SPECTRUMA Analytik GmbH. *GD-OES Theory*. Accessed: 25-10-2024. URL: https://www.spectruma.de/en/resources/gdoes-theory.

[49] *D8 Advance / D8 Discover User Manual Vol. 1.* Bruker AXS GmbH, 2010.

[50] K. Chen et al. "Measurement of poly-Si film thickness on textured surfaces by X-ray diffraction in poly- Si/SiO_x passivating contacts for monocrystalline Si solar cells". In: *Solar Energy Materials and Solar Cells* 236 (2022). DOI: https://doi.org/10.1016/j.solmat.2021.111510.

[51] C. Weidenthaler. "Pitfalls in the characterization of nanoporous and nanosized materials". In: *Nanoscale* 3 (2011), pp. 792–810. DOI: 10.1039/c0nr00561d.

[52] M. B. Vázquez-Santos et al. "Comparative XRD, Raman, and TEM Study on Graphitization of PBO-Derived Carbon Fibers". In: *The Journal of Physical Chemistry C* 116.1 (2012), pp. 257–268. DOI: 10.1021/jp2084499.

[53] *TLM-SCAN User Manual*. pv-tools GmbH.

[54] F.M. Smits. "Measurement of Sheet Resistivities with the Four-Point Probe". In: *Bell System Technical Journal* 34 (1958), pp. 711–718. DOI: 10.1002/j.1538-7305.1958.tb03883.x.

[55] T. Okker. "Processing and Characterization of Passivating Contacts with Low Thermal Budget for Silicon Solar Cells". MA thesis. University of Konstanz, 2021.

[56] L. Huang et al. "Characterization and simulation analysis of laser-induced crystallization of amorphous silicon thin films". In: *Materials Science in Semiconductor Processing* 16.6 (2013), pp. 1982–1987. DOI: https://doi.org/10.1016/j.mssp.2013.07.005.

Appendix A

Laser Machinery Setup

Figure A.1 shows the design of the laser equipment setup. Components (1) and (10) represent the green and UV laser scanner units, respectively, and contain the laser source and the beam path machinery. The Z-axis (3) moves the entire laser source compound as a unit, including both the zoom camera (2) and wide camera (9), to adjust the defocus parameter. Defocus D refers to the displacement of the beam focal plane relative to the target surface, meaning the beam is either above or below the focal position. These cameras are used to position and align the sample to reference points that must be registered every time before measurement. With those reference points, the software automatically aligns the wafer. The sample is manually positioned on a plate (5) and, with the help of a vacuum system, will be fixed to it. The sample will be placed in the desired position using a table-moving system composed of the X-axis (7) and the Y-axis (8) – XY table alignment. During lasering, material particles formed are extracted with the aid of an extractor tube (4).

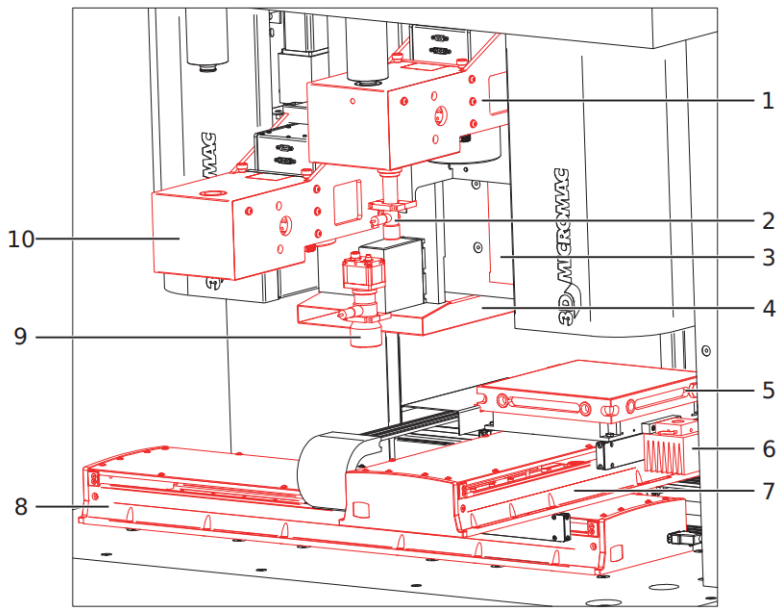

Figure A.1: Mechanical components setup design of *microSTRUCT C* laser system. Sourced from the microSTRUCT C manual [40]. 1 - 532 nm laser scanner unit (green laser); 2 - zoom camera; 3 - Z-axis; 4 - extraction tube; 5 - holder chuck; 6 - Power sensor; 7 - Y-axis; 8 - X-axis; 9 - wide camera; 10 - 355 nm laser scanner unit (UV laser).